Fall 2021

Impaired Metabolic Flexibility in a Mouse Model Of Leigh Syndrome

Richard Sterling McCain Jr

IMPAIRED METABOLIC FLEXIBILITY IN A MOUSE MODEL OF LEIGH SYNDROME

By
Richard Sterling McCain Jr

Bachelor of Science
University of South Carolina, 2016

Submitted in Partial Fulfillment of the Requirements

For the Degree of Doctor of Philosophy in

Biomedical Science

School of Medicine

University of South Carolina

2021

Accepted by:

Norma Frizzell, Major Professor

Susan Wood, Committee Member

Gerardo Piroli, Committee Member

Daping Fan, Committee Member

Deanna Smith, Committee Member

Tracey L. Weldon, Interim Vice Provost and Dean of the Graduate School

DEDICATION

I dedicate this dissertation to my wife; without whose support I would never have achieved so much.

ACKNOWLEDGEMENTS

I would like to thank my wife and family for their love and support over these years. I thank Dr. Norma Frizzell for training me to become a better scientist and for all that we have been able to accomplish. On that note, thank you to the members of the Frizzell laboratory for our work together over the years, including Dr. Gerardo Piroli, Holland Smith, Dr. Allison Manuel, Stephanie Martin, Jingtian (Josh) Wang, Bryan Fitzgerald, Macey Johnson, Tulsi Patel, Emery Tran, Cameron Kiger, Melat Tarekegne, and Shoba Swaminathan. I am thankful for the guidance of my committee who have improved the quality of this work, including Dr. Susan Wood, Dr. Norma Frizzell, Dr. Gerardo Piroli, Dr. Daping Fan, and Dr. Deanna Smith. Finally, I thank the faculty and staff of the department of Pharmacology, Physiology, and Neuroscience; the Viral Vector Core; the Mass Spectrometry facilities; the Presidential Fellowship program; and the School of Medicine for their efforts in training and supporting me.

ABSTRACT

Metabolic dysfunction burdens tissues with high energy demands, particularly the brain. Leigh syndrome is a mitochondrial encephalopathy stemming from genetic defects in the electron transport chain. Leigh syndrome patients develop lactic acidosis, ataxia, bilateral necrotizing lesions in the brainstem and basal ganglia, lesion microgliosis, and eventually death due to respiratory failure. The NADH dehydrogenase [ubiquinone] iron-sulfur protein 4 (NDUFS4) knockout mouse is an established model of Leigh syndrome due to impaired assembly of mitochondrial Complex I that develops motoric deficits and necrotizing lesions in the brainstem vestibular nuclei and olfactory bulb. In addition to the Complex I-derived bioenergetics defect, altered production of other metabolites, including fumarate, modulate protein function due to irreversible protein modification. Fumarate-induced protein succination (2SC) is increased in the NDUFS4 knockout (KO) brainstem and olfactory bulb. In this dissertation, we investigated altered metabolite production with an emphasis on itaconate-derived regulation of microglial and macrophage function in the NDUFS4 KO mouse.

We detected limited inflammatory markers in the NDUFS4 KO olfactory bulb, despite abundant microglia. We quantified impaired metabolism, reduced phagocytic capacity, and limited inflammatory activity in macrophages as a model of the microglial response during pro-inflammatory lipopolysaccharide stimulation.

Knockout of NDUFS4 promoted a metabolic shift from mitochondrial to glycolytic metabolism, decreased the metabolic reserve, and impaired the accumulation of the immunometabolites itaconate and succinate during pro-inflammatory conditions. Itaconate-derived protein dicarboxypropylation provides a robust measure of the cellular capacity to increase immunometabolism, and we observe that this is recognized by an in-house antibody detecting succinate moieties. Using this antibody as a tool, we determined that isolated NDUFS4 KO microglia do not accumulate fumarate or itaconate-induced protein modifications in contrast to neurons, where fumarate-derived succination is significantly increased.

Given that the production of the anti-inflammatory metabolite itaconate was reduced, we hypothesized that exogenous itaconate, as the ester 4-octyl itaconate (4OI), might limit microglial accumulation and improve motor behavior in NDUFS4 KO mice. 4OI administration slowed the NDUFS4 knockout-induced decline in motor endurance in male mice with beneficial trends to improve other clinical symptoms, independent of microglial content in the olfactory bulb. The data suggest that itaconate supplementation may have therapeutic potential in the NDUFS4 KO, but the mechanisms underlying this benefit remain to be determined.

Finally, we improved methods to simultaneously detect enantiomers of lactate and 2-hydroxyglutarate. We hypothesized that fumarate-derived succination of a component of the α-ketoglutarate dehydrogenase complex would favor generation of L-2-hydroxyglutarate. Total levels of L and D enantiomers of 2-hydroxyglutarate were measured in parallel with lactate in tissues of the NDUFS4

knockout. The findings suggest additional metabolic flexibility in the NDUFS4 knockout, which may be harnessed for therapeutic benefits.

In summary, we find that the loss of NDUFS4 contributes to impaired metabolic flexibility and altered metabolic responses when challenged, elucidating novel alternative targets with therapeutic potential to treat this devastating disease.

TABLE OF CONTENTS

LIST OF FIGURES

LIST OF ABBREVIATIONS

2-HG 2-Hydroxyglutarate

2SC ..... S-(2-succino)cysteine

4OI ..... 4-octyl itaconate

ABP ..... Albumin-binding peptide

ANOVA ..... Analysis of variance

ASL ..... Argininosuccinate lyase

Acetyl-CoA ..... Acetyl-coenzyme A

ASS ..... Argininosuccinate synthetase

AST ..... Aspartate aminotransferase

ATP ..... Adenosine triphosphate

BMDM ..... Bone marrow-derived macrophages

BS ..... Brainstem

CAT ..... Catalase

cGAS ..... Cyclic GMP-AMP synthase

CNS ..... Central nervous system

CPEO ..... Chronic progressive external ophthalmoplegia

Crus 1 ..... Crus 1 ansiform lobule

DATAN ..... Diacetyl-l-tartaricanhydride

DLST ..... Dihydrolipoyllysine-residue succinyltransferase

DMF ..... Dimethyl fumarate

DMKG ..... Dimethyl-ketoglutarate

ETC..... Electron transport chain

FAD.....Flavin adenine dinucleotide

Fh1..... Fumarase/fumarate hydratase

FN ..... Fastigial nucleus

GAPDH .....Glyceraldehyde 3-phosphate dehydrogenase

GTP ..... Guanosine triphosphate

H_2O_2.....Hydrogen peroxide

HIF-1α.....Hypoxia inducible factor-1α

HO-1 ..... Heme oxygenase-1

Iba-1..... Ionized calcium binding adaptor molecule 1

IFN-γ .....Interferon gamma

IL-1β..... Interleukin 1β

IMS ..... Intermembrane space

iNOS ..... Inducible nitric oxide synthase

IO/Gi ..... Inferior olive/gigantocellular reticular nucleus

IsoTOP-ABPP .....Isotopic tandem orthogonal proteolysis activity-based protein profiling

JmjC.....Jumonji-C

KATP channels ..... ATP sensitive potassium channels

KEAP1 .....Kelch-like ECH-associated protein 1

KO.....Knock-out

L2HGDH .....L-2-HG dehydrogenase

LC-MS..... Liquid chromatography-mass spectrometry

LOX.....Lactate oxidase

LS ..... Leigh syndrome

MDH2 ..... Malate dehydrogenase

MELAS ..... Mitochondrial encephalomyopathy, lactic acidosis, and stroke-like episodes

MT-ATP6 ..... Mitochondrially encoded ATP synthase membrane subunit 6

MTND ..... Mitochondrially encoded NADH:ubiquinone oxidoreductase core subunit

mTOR ..... Mechanistic target of rapamycin

MT-TL1 ..... Mitochondrially-encoded tRNA leucine 1

NAD^+ ..... Nicotinamide adenine dinucleotide

$NADP^+$ ..... Nicotinamide adenine dinucleotide phosphate

ND75 ..... NADH dehydrogenase (ubiquinone) 75 kDa subunit

NDE1 ..... NADH-ubiquinone oxidoreductase chain 1

NDI1 ..... NADH-ubiquinone reductase

NDUFA12 ..... NADH dehydrogenase [ubiquinone] 1 alpha subcomplex subunit 12

NDUFAF2 ..... NADH:ubiquinone oxidoreductase complex assembly factor 2

NDUFS4 ..... NADH dehydrogenase [ubiquinone] iron-sulfur protein 4

NMN ..... Nicotinamide mononucleotide

NO ..... Nitric oxide

NQO1 ..... NAD(P)H:quinone oxidoreductase-1

NRF2 ..... Nuclear factor erythroid 2-related factor 2

OB ..... Olfactory bulb

OCR ..... Oxygen consumption rate

OXPHOS ..... Oxidative phosphorylation

P(#) ..... Postnatal day (#)

PHGDH ..... D-3-phosphoglycerate dehydrogenase

PO_2 ..... Partial pressure of oxygen

Polg..... Mitochondrial polymerase gamma

qRT-PCR ..... Quantitative real-time polymerase chain reaction

Reductive stress ..... NADH/NAD^+ ratio

ROS ..... Reactive oxygen species

RS-..... Cysteine thiolate group

RSH ..... Cysteine thiol group

SDH ..... Succinate dehydrogenase

STING ..... stimulator of interferon genes

SURF1 ..... Surfeit locus protein 1

TCA ..... Tricarboxylic acid cycle/Krebs cycle

TET2 ..... Ten-eleven translocation 2

V-ATPase ..... Vacuolar H^+ ATPase

VDAC ..... Voltage-dependent anion channel

Vmax ..... Maximum reaction rate

VN ..... Vestibular nucleus

WT ..... Wild-type

αKGDH ..... α-ketoglutarate dehydrogenase

CHAPTER 1

INTRODUCTION

1.1 Mitochondrial Respiration

While the role of mitochondria in energy production is well-known, recent studies have elucidated the specific role of mitochondrial metabolites in regulating the immune response, a field known as immunometabolism (Tannahill et al., 2013; Mills et al., 2018; Ryan and O'Neill, 2020). An overview of mitochondrial metabolism is provided below, with an emphasis on metabolites known to have immunomodulatory and signaling roles.

1.1.1 The Krebs Cycle. Mitochondria produce the majority of cellular adenosine triphosphate (ATP) through the Krebs cycle (tricarboxylic acid cycle, TCA) and oxidative phosphorylation. As a central hub for metabolism, the Krebs cycle oxidizes the acetyl-coenzyme A (acetyl-CoA) produced from glycolysis, lipolysis, or proteolysis to generate several high-energy intermediates, including NADH (**Figure 1.1**). Citrate synthase condenses acetyl-CoA and oxaloacetate to generate citrate. Aconitase isomerizes citrate to form *cis*-aconitate and then isocitrate. Isocitrate dehydrogenase oxidizes isocitrate to produce α-ketoglutarate, which is then oxidized by α-ketoglutarate dehydrogenase to yield succinyl-CoA. Electron transfer to reducing equivalents occurs in parallel with these reactions, namely the reduction of two nicotinamide adenine dinucleotide (NAD^+) to NADH.

Succinyl-CoA synthase generates succinate from succinyl-CoA while also facilitating substrate-level phosphorylation to produce guanosine triphosphate (GTP). Succinate dehydrogenase (SDH), which also acts as Complex II of the electron transport chain, oxidizes succinate to fumarate while reducing flavin adenine dinucleotide (FAD) to $FADH_2$. Fumarase hydrates fumarate to form malate, which is then oxidized to oxaloacetate by malate dehydrogenase while also reducing one NAD^+ to NADH (Ryan et al., 2019). The overall energy yield from a single turn of the Krebs cycle is 3 NADH, 1 $FADH_2$, and 1 GTP (**Figure 1.1**).

1.1.2 Oxidative Phosphorylation. The electron transport chain is a series of 5 protein complexes that utilize oxidative phosphorylation to convert high-energy intermediates, such as those produced by the Krebs cycle, to ATP (**Figure 1.2**). Complex I, or NADH ubiquinone oxidoreductase, is a 45-subunit protein complex that transfers electrons from NADH through iron-sulfur clusters to ubiquinone while simultaneously pumping protons into the mitochondrial intermembrane space to form a proton gradient (Mimaki et al., 2012). Complex II transfers the electrons donated by $FADH_2$ through iron-sulfur clusters to ubiquinone. Ubiquinone shuttles the electrons from Complex I and II to Complex III, also known as cytochrome c reductase. Complex III oxidizes ubiquinone, transfers the electrons through iron-sulfur clusters and heme to reduce cytochrome c, and pumps two additional protons into the intermembrane space. The reduced cytochrome c shuttles the electrons to Complex IV (cytochrome c oxidase), which oxidizes the cytochrome c while reducing molecular oxygen to water and contributing further to the proton gradient. Complex V, ATP synthase, uses the proton motive force generated by

Complexes I-IV to synthesize ATP in response to cellular energy demands (Raimondi et al., 2020).

1.1.3 Rewiring the Krebs Cycle during Macrophage Activation. The expanding field of immunometabolism has demonstrated that the Krebs cycle can undergo remodeling to support alternative metabolic functions that are not immediately associated with the production of reducing equivalents for oxidative phosphorylation. Macrophages are well-known to have a plastic phenotype, switching between quiescent and activated states in response to their extracellular environment (**Figure 1.3**). The rewiring of Krebs cycle metabolism is now appreciated as a central regulator of the dynamic states of macrophage activation (Seim et al., 2019). This regulation is achieved through modulating the activity and expression of select Krebs cycle enzymes, resulting in pronounced metabolite changes that can either promote or inhibit cytokine production, as discussed below.

Metabolism plays a central role in orchestrating macrophage and microglial inflammatory activation (El Kasmi and Stenmark, 2015; Davies et al., 2017). The pro-inflammatory activation of these cells by lipopolysaccharide (LPS, part of the outer membrane of Gram-negative bacteria) and interferon-γ (IFN-γ) dramatically increases the utilization of glycolysis for fuel. In parallel, there is a decrease in oxidative phosphorylation and a truncated Krebs cycle that favors succinate accumulation and concomitant interleukin-1β (IL-1β) production (**Figure 1.4**) (Van den Bossche et al., 2017; Seim et al., 2019; Lauro and Limatola, 2020; Lynch et al., 2020). Pro-inflammatory macrophages need to generate nitric oxide (NO) to

kill intracellular mycobacteria, and NO inhibits succinate dehydrogenase, promoting the truncated Krebs cycle. To sustain NO production, macrophages employ the argininosuccinate pathway whereby argininosuccinate synthetase (ASS) catalyzes the synthesis of argininosuccinate from aspartate and citrulline. Argininosuccinate lyase (ASL) metabolizes the argininosuccinate to produce arginine and fumarate. Arginine is consumed by inducible nitric oxide synthase (iNOS) in the presence of NADPH to generate NO (Qualls et al., 2012; Jha et al., 2015; Fall et al., 2020; Bizzoco et al., 2007). The fumarate generated anaplerotically replenishes the Krebs cycle after the SDH breakpoint, and the malate-aspartate shuttle ensures the cycle of metabolites continues using mitochondrial aspartate aminotransferase (AST) (**Figure 1.4**) (El Kasmi and Stenmark, 2015).

Itaconate is the most abundant metabolite produced in macrophages exposed to LPS (Jha et al., 2015; Mills et al., 2018). Itaconate is a dicarboxylic acid derived from *cis*-aconitate of the Krebs cycle by the immune-responsive gene 1 (IRG1) protein (**Figure 1.4**). *Irg1*-deficient animals succumb early to *M. tuberculosis infection* (Nair et al., 2018). Itaconate production is induced in macrophages activated by pro-inflammatory stimuli and acts as a concentration-dependent immunomodulator in activated immune cells (Bambouskova et al., 2018; Mills et al., 2018; Ryan and O'Neill, 2020; Jha et al., 2015). As itaconate levels rise, it acts as a competitive inhibitor of succinate dehydrogenase, which leads to a rise in succinate levels (Lampropoulou et al., 2016). Reduced succinate oxidation is associated with reverse electron transfer and reactive oxygen species

(ROS) generation (Mills et al., 2016; Scialò et al., 2017) and increases protein lysine succinylation by succinyl-CoA (Tannahill et al., 2013). Elevations in succinate regulate the levels of prolyl hydroxylases to stabilize hypoxia-inducible factor-1α (HIF-1α) (Tannahill et al., 2013; Mills et al., 2014; Seim et al., 2019). Nuclear translocation of HIF-1α is associated with the transcription of IL-1β (Tannahill et al., 2013), TNF-α, and IL-6 (Guo et al., 2017), as well as genes encoding the glycolytic enzymes phosphofructokinase and GAPDH (McGettrick and O'Neill 2020). Overall, both itaconate and succinate accumulate rapidly in LPS-stimulated macrophages and are robust indicators of M1 activation (**Figure 1.4**; Seim et al., 2019).

1.1.4 Protein Dicarboxypropylation by Itaconate. The identification of dynamic metabolite flux in macrophages has prompted mechanistic investigations delineating how metabolites regulate the immune cell landscape. Several metabolites are capable of post-translational protein modification, providing an alternative mechanism whereby they may alter the function of select proteins. As a dicarboxylic acid containing a double bond, itaconate is capable of Michael addition chemistry to irreversibly alkylate cysteine thiols to generate 2,3-dicarboxypropylcysteine, referred to as protein dicarboxypropylation (**Figure 1.5**). While early increases in itaconate modulate succinate dehydrogenase by allosteric mechanisms and lead to succinate accumulation, the dicarboxypropylation of protein thiols by sustained itaconate also contributes to potent anti-inflammatory effects of itaconate (Cordes et al., 2016; Mills et al., 2018). Mills *et al.* discovered that dicarboxypropylation of the Kelch-like ECH-associated protein 1 (KEAP1) by

itaconate impaired its ability to associate with and trigger degradation of nuclear factor erythroid 2-related factor 2 (NRF2) protein (Mills et al., 2018). NRF2 is a transcription factor that promotes increased expression of several anti-inflammatory proteins, including heme oxygenase-1 (HO-1) and enzymes involved in glutathione synthesis. Increased HO-1 transcription attenuates the production of pro-inflammatory IL-1β and IL-6 (Bambouskova et al., 2018; Mills et al., 2018; Ryan and O'Neill, 2020). NRF2 also reduces the expression of Type I interferons by inhibiting the production of the stimulator of interferon genes (STING), demonstrating a link between metabolic reprogramming and antiviral sensing (Olagneir et al., 2018). More recently, itaconate-induced dicarboxypropylation of NLRP3 has been shown to directly inhibit pro-inflammatory inflammasome activation and IL-1β production. The NLRP3 inflammasome is composed of NLRP3, ASC, NEK7, and caspase 1. Activation of the NLRP3 inflammasome results in caspase 1-mediated cleavage of pro-IL-1β, pro-IL-18, and gasdermin D into their active form, stimulating a pro-inflammatory phenotype (Hooftman et al., 2020). Cell permeable esters of itaconate have been used in both wild-type and *Irg1* deficient cells to confirm the role of these itaconate targets in modulating the immune cell phenotype (Lampropoulou., et al., 2016; Mills et al., 2018).

1.1.5 Protein Succination by Fumarate. Like itaconate, fumarate is also a dicarboxylic acid that can act as a Michael acceptor to react irreversibly with nucleophilic cysteine residues (Manuel et al., 2017). Under favorable conditions, the accumulation of fumarate results in the non-enzymatic modification of cysteine residues, generating the covalent chemical adduct S-2-succinocysteine (2SC)

(**Figure 1.6**) (Alderson et al., 2006; Nagai et al., 2007; Frizzell et al., 2009). During this reaction, the double bond of fumarate is lost, and a succinate moiety is attached to the thiol group of the cysteine residue, resulting in the cysteine succination nomenclature. Protein succination by fumarate is distinct from reversible metabolite-driven acylation reactions, e.g., lysine succinylation (Tannahill et al., 2013), as S-2-succinocysteine (2SC) is a chemically irreversible thioether adduct. The term 'succination' distinguishes protein succination from protein succinylation, in which an ester, thioester, or amide bond is formed on lysine residues (Frizzell et al., 2012; Yang et al., 2019; Hirschey and Zhao, 2015). The non-enzymatic and irreversible nature of cysteine succination in eukaryotic cells was confirmed when the rate of succination of glutathione (GSH) by exogenous $^{13}C_2$-fumarate was not enhanced or degraded in the presence of cellular extracts (Zheng et al., 2015; Wagner et al., 2017).

As fumarate is a mild electrophile, it was originally proposed to be most reactive with the more nucleophilic cysteine thiolate group (RS-). While the free thiol group of cysteine (RSH) has a pKa ~8.5, thiolates have a lower pKa determined by the local protein microenvironment (Poole, 2015; Bak et al., 2019). Fumarate succinates several proteins with nucleophilic cysteines, including glyceraldehyde-3-phosphate dehydrogenase (GAPDH, Cys 149 and 244) (Blatnik et al., 2008a; Blatnik et al., 2008b), Kelch-like ECH-associated protein 1 (KEAP1, Cys 288), DJ-1 (Cys 106) (Adam et al., 2014), and α-tubulin (Cys 347 and Cys 316) (Piroli et al., 2014). However, thiol nucleophilicity does not appear to be the foremost determinant for reactivity. For example, non-nucleophilic cysteines in

exposed protein regions are also fumarate-reactive, e.g., succination of an N-terminal cysteine in adiponectin disrupts disulfide bond mediated oligomerization (Frizzell 2009).

Kulkarni *et al.* identified a total of 684 fumarate-reactive cysteines in a fumarate hydratase deficient tumor cell line (UOK262) and documented a striking anti-correlation with established datasets of reactive nucleophilic cysteines (Weerapana et al., 2010; Kulkarni et al., 2019). Further analysis of the structural determinants of fumarate-reactive cysteines demonstrated enrichment of acidic residues, such as glutamate and aspartate, in regions flanking the succinated cysteine (Kulkarni et al., 2019). This enrichment of acidic residues contrasts with the basic residues common in motifs with nucleophilic hyperreactive cysteines and suggests that an acidic microenvironment promotes cysteine succination due to the accumulation of protonated fumarate. The endogenous production of elevated fumarate has been documented in (patho)physiological conditions that facilitate the accumulation of lactic acid, promoting the protonation of fumarate and cysteine succination. The impact of endogenous fumarate accumulation in models of diabetes and mitochondrial encephalopathy is discussed further.

3T3-L1 adipocytes matured in high glucose, high insulin conditions (25-30 mM glucose, 3 nM insulin) increase fumarate levels by ~4-fold after 6 days of maturation, and protein succination increases more than 10-fold after 8 days of maturation (Nagai et al., 2007). Metabolic labeling has also demonstrated that lactate generation is prioritized in adipocytes, particularly in response to insulin, but is maintained even in insulin-resistant states, enhancing protein succination in

adipocytes and adipose tissue during diabetes (Krycer et al., 2020; Lai and Goldman, et al., 1992; Tanis et al., 2015; Manuel et al., 2017; Manuel et al., 2020). Flux analysis with isotopically labeled glucose revealed that the accumulation of fumarate is sustained in the presence of insulin due to bifurcated glucose metabolism (Krycer et al., 2017; Krycer et al., 2020). Oxidative Krebs cycle metabolism occurs in parallel with enhanced pyruvate anaplerosis via pyruvate carboxylase (Sugden and Holness, 2011). The ATP-dependent carboxylation of pyruvate ultimately supports nicotinamide adenine dinucleotide phosphate (NADPH) production and fatty acid synthesis via malic enzyme activity (Liu et al., 2016). Fumarate accumulation due to enhanced oxaloacetate and malate production is a consequence of this pyruvate cycling in the nutrient-rich state (Krycer et al., 2020).

A total of ~40 succinated proteins have been identified in primary adipocytes isolated from the epididymal fat pads of db/db mice or 3T3-L1 adipocyte matured in high glucose (Nagai et al., 2007; Merkley et al., 2014). These include cytosolic enzymes (GAPDH, triose phosphate isomerase, lactate dehydrogenase A, and tryptophanyl-tRNA synthetase), cytoskeletal proteins (α and β tubulin, vimentin, annexins, and 14-3-3 family proteins), proteins located in or trafficked through organelles (protein disulfide isomerase, glucose-regulated protein 78, the secreted hormone adiponectin, and lysosomal cathepsin B), and nuclear proteins (transcriptional activator protein Pur-beta, elongation factor 2, and nuclear factor 1 X-type) (Merkley et al., 2014; Piroli et al., 2014; Frizzell et al., 2009). The heterogeneous locations of succinated proteins suggest that abundant fumarate

will modify available thiols based on factors determined by the local microenvironment.

Broader consideration of conditions in which lactic acidosis is present and where the NADH:NAD^+ ratio might promote fumarate accumulation prompted us to examine the role of protein succination in mitochondrial diseases. These conditions especially plague areas with high ATP needs, such as the brain and muscles (Delonlay et al., 2013). As discussed further below, we were the first to describe increased fumarate levels and protein succination in a mouse model of the mitochondrial disease Leigh Syndrome (Piroli et al., 2016). Since the lesioned brain regions in Leigh Syndrome contain significant gliosis, we decided to investigate how fumarate and itaconate are regulated during inflammatory activation in this model of mitochondrial disease.

1.2 Mitochondrial Disease

Mitochondrial diseases are genetic disorders that can be caused by mutations in either mitochondrial or nuclear DNA that impair mitochondrial function. Over 350 mutations have been documented in factors that facilitate the assembly or function of the electron transport chain to impact the production of mitochondrial energy (Ng et al., 2021). Mitochondrial DNA mutations are transmitted by maternal inheritance, while mitochondrial disease caused by mutations in nuclear DNA may follow autosomal dominant, autosomal recessive, or X-linked inheritance patterns. Given the importance of mitochondrial function, mitochondrial diseases commonly feature a failure to thrive from impaired energy

production. Tissues with high energy demands, including the brain and muscles, are most vulnerable to impaired energy production. Mitochondrial diseases have wide-ranging ramifications, including neurological dysfunction, respiratory abnormalities, muscle weakness, and death (Ng et al., 2021; Parikh et al., 2015; Taylor et al., 2005). These diseases may, therefore, manifest as mitochondrial encephalopathies, myopathies, or encephalomyopathies with multi-system involvement. Several of the more common manifestations of mitochondrial disease are discussed below.

1.2.1 MELAS. Mitochondrial encephalomyopathy, lactic acidosis, and stroke-like episodes (MELAS, 1:20,000 prevalence) most commonly stem from a maternally inherited mutation of arginine to guanine (A3243G) in the mitochondrially-encoded tRNA leucine 1 (*TL1*). This gene encodes the mitochondrial tRNA that is responsible for leucine incorporation into newly synthesized components of the electron transport chain (Chinnery et al., 2000; Majamaa et al., 1998; Uusimaa et al., 2007; Manwaring et al., 2007; Goto et al., 1990). Mutations in tRNA impair mitochondrial protein synthesis leading to lactic acidosis, NO deficiencies, myopathy, fatigue, difficulty breathing, recurring headaches, dementia, epilepsy, and stroke-like episodes. The stroke-like episodes cause lesions to develop in areas of high energy demand, especially the neuron-dense cortex. Therefore, acute lesions commonly occur in the primary visual, somatosensory, and auditory cortices (Iizuka and Sakai, 2005; Bhatia et al., 2019; El-Hattab et al., 2015). Diabetes, hearing loss, and heart and kidney problems may also develop in these patients, confirming multi-system involvement. The

symptoms of MELAS can begin in early childhood, and most individuals experience stroke-like episodes before age 40. There is no cure, but L-arginine, a precursor of NO, supplementation has been shown to reduce the incidence and severity of stroke-like episodes (Koga et al., 2018; El-Hattab et al., 2015).

1.2.2 Leber's hereditary optic neuropathy. Leber's hereditary optic neuropathy (1:65,000 incidence) stems from genetic defects in the mitochondrial DNA for Complex I, including NADH-ubiquinone oxidoreductase chain 1 (*NDE1*, G3460A), NADH-ubiquinone oxidoreductase chain 4 (*NDE4*, G11778A), and NADH-ubiquinone oxidoreductase chain 6 (*NDE6*, T14484C) (Mascialino et al., 2012; Taylor et al., 2003). These mutations selectively cause progressive degeneration of retinal ganglion cells and bilateral loss of vision. This disease is maternally inherited and typically presents in males around 15 to 35 years, leading to total visual loss after one year of disease onset. While there is no proven treatment, administration of quinone analogs or vitamin B12 supplementation promotes vision recovery in some cases (Mohana Devi et al., 2021; Mascialino et al., 2012; Man et al., 2002; Peragallo and Newman, 2015).

1.2.3 Leigh Syndrome. Leigh syndrome (1:40,000 prevalence) is caused by a variety of nuclear or mitochondrial genetic defects in the electron transport chain or pyruvate dehydrogenase complex, including Complex I. Mutation in the mitochondrially encoded ATP synthase membrane subunit 6 (*ATP6)* gene disrupts Complex V and is the most common cause of Leigh syndrome (Lake et al., 2016; Sofou et al., 2014). The pathogenesis of Leigh syndrome varies with different mutations. Mutations in the Complex IV assembly factor surfeit locus protein 1

(SURF1) can also cause hypertrichosis and leukodystrophy (Rahman et al., 2001; Wedatilake et al., 2013). While not a component of the electron transport chain, mutations in subunits associated with the pyruvate dehydrogenase complex also manifest as Leigh syndrome (Lake et al., 2016). While *ATP6* is the most common gene mutated in Leigh syndrome patients, Complex I is the most common target for the wide range of gene mutations associated with Leigh syndrome, including the mitochondrially encoded NADH:ubiquinone oxidoreductase core subunit 3 (*MTND3), MTND5,* and the NADH dehydrogenase [ubiquinone] iron-sulfur protein 4 (*NDUFS4*). Complex I has three functional subunits: the NADH binding and oxidation N-module, the electron transfer to ubiquinone Q-module, and the proton pumping P-module (Scacco et al., 2003; Martín et al., 2005; Petruzzella et al., 2002). The NADH dehydrogenase [ubiquinone] iron-sulfur protein 4 is an 18 kDa assembly protein in the electron input module (N module) of Complex I. Mutation of NDUFS4 in Leigh syndrome patients impairs the maximum reaction rate (Vmax) and disrupts Complex I phosphorylation patterns. NDUFS4 mutation-associated misassembly of Complex I triggers loss of the NADH dehydrogenase [ubiquinone] 1 alpha subcomplex subunit 12 (NDUFA12) accessory subunit and increases NADH:ubiquinone oxidoreductase complex assembly factor 2 (NDUFAF2) levels, further altering the assembly of Complex I (Scacco et al., 2003; Adjobo-Hermans et al., 2020).

These defects lead to muscle hypotonia and bilateral basal ganglia and brainstem lesions that cause death due to respiratory failure after a few years of life (Finsterer, 2008; Bakare et al., 2021). There is no cure for Leigh syndrome, but

some interventions such as a ketogenic diet, vitamin therapy, and improving electron flow using coenzyme Q_{10} supplementation slow the progression of symptoms by a few years (Chen et al., 2017; Ernster and Forsmark-Andree, 1993; Laugel et al., 2007). The clinical aspects of Leigh syndrome are discussed further below.

1.3 Leigh Syndrome Pathology

1.3.1 Clinical Aspects of Leigh Syndrome. Leigh syndrome is a subacute necrotizing encephalopathy characterized by bilateral lesions in the brainstem and basal ganglia. Clinically, Leigh syndrome infant patients demonstrate a failure to thrive and develop muscle hypotonia, ataxia, seizures, and death due to respiratory failure after a few years of life (Finsterer, 2008; Lake et al., 2016; Sofou et al., 2014). Illness or injury can accelerate the progression of Leigh syndrome (Cavanagh and Harding, 1994; Van Coster et al., 1991). Mitochondrial dysfunction in Leigh syndrome patients reduces mitochondrial ATP production and promotes the conversion of pyruvate to lactate. Clinical biochemical findings include lactic acidosis in biofluids or altered pyruvate:lactate ratios by magnetic resonance imaging in affected brain regions (Jurkiewicz et al., 2011; Patel et al., 2012). Periods of illness due to infection correlate with increased metabolic acidosis in these patients. The limited electron flux contributes to the accumulation of reduced electron carriers (e.g., NADH) (Finsterer 2008; Leigh et al., 1951; Piroli et al., 2016; Quintana et al., 2010). As a result, other metabolic pathways may be impacted, including α-hydroxybutyrate, myristoylcarnitine, and succinate metabolism. Increased α-hydroxybutyrate and myristoylcarnitine and decreased succinate

have been detected in the plasma of Leigh syndrome patients (Thompson Legault et al., 2015; Ferrari et al., 2017).

1.3.2 NDUFS4 Knockout Model of Leigh Syndrome. One of the most frequently studied models of Leigh Syndrome is the *Ndufs4* knockout (NDUFS4 KO) mouse. Correctly assembled, the multi-subunit Complex I of the electron transport chain forms a 1 MDa complex. NDUFS4 is an assembly protein for Complex I, and the loss of the *Ndufs4* gene impairs the assembly and stability of Complex I. This misassembly results in a smaller 830 kDa complex being formed (Calvaruso et al., 2012) with significantly less electron shuttling capacity than properly formed Complex I. The activity of Complex I in NDUFS4 KO brain is reduced to 26% of normal controls, and ATP production is significantly reduced. These defective bioenergetics severely impact the energy-demanding neurons, driving the mitochondrial encephalopathy phenotype. NDUFS4 KO mice present with motoric deficits, bilateral necrotizing vestibular nuclei and olfactory bulb lesions, and lactic acidosis leading to respiratory failure and death at approximately 8 weeks, recapitulating the symptoms of severe human Leigh syndrome (Leong et al., 2012; Quintana et al., 2010). Selective knockout of *Ndufs4* in the central nervous system under the *Nestin* promoter shows the same symptoms as systemic knockout under the *Mox2* promoter. Therefore, central nervous system mitochondrial dysfunction is sufficient to mimic the disease (Kruse et al., 2008; Quintana et al., 2010; Piroli et al., 2016). Strikingly, despite the ubiquitous loss of the *Ndufs4* gene, the muscles of the affected mice presented with no evidence of myopathy. NDUFS4 KO mice develop neuropathy that leads to motoric deficits,

respiratory failure, and death without myopathy. Therefore, NDUFS4 KO mice are an excellent model for the study of Leigh-like encephalopathy.

To further delineate the roles that specific neuronal subtypes play in the pathogenesis of NDUFS4 KO mice, Bolea *et al.* examined the effects of knockout of NDUFS4 in cholinergic, glutamatergic, and GABAergic neurons (Bolea et al., 2019). Knockout of NDUFS4 in cholinergic neurons, which carry information from the central nervous system to the periphery, did not result in any clinical phenotype in the mice. *Ndufs4* deficiency, specifically in glutamatergic neurons, caused the mice to develop brainstem neuroinflammation, resulting in reduced lifespan and body weight and motor and respiratory deficits. GABA-specific knockout of *Ndufs4* led to neuroinflammation in the basal ganglia, reduced lifespan and body weight, and death due to epileptic seizures (Bolea et al., 2019). Therefore, specific neuronal subsets drive the clinically diverse phenotype of Leigh syndrome, justifying the importance of examining mitochondrial disease pathology at a cellular level.

1.4 Mechanisms Contributing to the Pathology of Leigh Syndrome

Despite well-described single gene defects predominantly affecting the electron transport process, the precise mechanisms driving region-specific pathogenesis of Leigh syndrome are not fully established. Reduced ATP production, increased reductive stress, and unresolved microgliosis are salient factors for Leigh syndrome pathogenesis. However, it remains unclear why specific cell types appear to be more affected than others. A mechanistic understanding of

the factors that accelerate biochemical decline is needed to design targeted therapies for the treatment of Leigh syndrome.

1.4.1 Oxidative Phosphorylation Derived ATP Deficit. Leigh Syndrome resulting from Complex I deficits has a significant reduction in cellular ATP production due to reduced proton pumping at Complex I. The loss of NDUFS4 results in the assembly of a smaller complex with significantly reduced electron shuttling ability. Despite this significant ATP reduction, Complex I in the NDUFS4 KO model has been shown to directly associate with Complex III as part of a supercomplex, potentially facilitating improved electron transfer to cytochrome c (Calvaruso et al., 2012). This compensation may also explain why individuals with significant oxidative phosphorylation deficits may survive and deteriorate more slowly. Rapamycin treatment of NDUFS4 KO mice increases the median lifespan to over 100 d versus 52 d in untreated KOs (Johnson et al., 2013; Johnson et al., 2015). Rapamycin is an inhibitor of the mammalian target of rapamycin (mTOR), a regulator of protein synthesis. Zheng *et al.* demonstrated ATP conservation through decreased protein synthesis, likely sparing energy for the demands of neurons (Zheng et al., 2016).

Reduced electron transport chain flux is frequently believed to be accompanied by oxidative stress. Augmented protein carbonylation, derived from oxidative protein modification, was described in the olfactory bulbs (Quintana et al., 2010) but not in the motor cortex of the NDUFS4 KO mice (Felici et al., 2014). However, we and others did not find increased HNE-protein conjugation in the lesioned brainstem (Kayser et al., 2016; Piroli et al., 2016). The absence of overt

oxidative stress in primary NDUFS4 KO fibroblasts and bone marrow-derived macrophages has recently been confirmed by another laboratory (Miller et al., 2021). Indeed, specific measurement of the rate of hydrogen peroxide (H_2O_2) production by isolated mitochondria demonstrated no difference in H_2O_2 production by the NDUFS4 KO versus wild-type (WT) mice (Jain et al., 2019). Therefore, the evidence confirming that oxidative stress is a driver of pathological decline is limited.

1.4.2 Reductive Stress. Another consequence of electron transport chain inhibition is an increase in the accumulation of NADH relative to NAD^+ (NADH/NAD, reductive stress) (Frizzell et al., 2012; Sharma et al., 2021). Increased reductive stress favors the production of lactate to regenerate NAD^+. Therefore, lactic acidosis and the pyruvate: lactate ratio often reflect reductive stress present in electron transport chain defects. As dysfunctional oxidative phosphorylation does not regenerate NAD^+, NADH accumulates and inhibits Krebs cycle dehydrogenases, amongst other pathways. Therefore, reductive stress aggravates pathways that require regeneration of reducing equivalents and contributes to increases in the levels of metabolites, including fumarate and pyruvate (Piroli et al., 2016; Finsterer et al., 2008). McElroy *et al.* demonstrated that knock-in of yeast NADH-ubiquinone reductase (NDI1) in NDUFS4 KO mice to regenerate NAD^+ without restoring energy production improved the lifespan of NDUFS4 KO mice but did not improve motor endurance on the rotarod task or distance traveled in the novel open field environment, indicating the importance of NAD^+ regeneration for survival (McElroy et al., 2020). However, this strategy also

demonstrated that additional factors are driving the pathology in the most affected brain regions. Therefore, other factors derived from the increased reductive stress contribute to the accelerated motor decline observed in the NDUFS4 KO model of Leigh syndrome (Iannetti et al., 2018).

1.4.3 Altered Metabolism. Our laboratory provided the first evidence that reductive stress-derived increases in fumarate could drive increased succination in the brain of the NDUFS4 KO mouse (Piroli et al., 2016). Importantly, these increases in succination (2SC) were documented only in the brain regions affected by pathology but not in other tissues, e.g., skeletal muscle. The vestibular nucleus and inferior olivary/gigantocellular reticular nucleus of the brainstem, the deep cerebellar fastigial nucleus, and the olfactory bulb all demonstrated increased succination as detected by an anti-2SC antibody (**Figure 1.7**) (Nagai et al., 2007; Piroli et al., 2016). Protein succination in these regions is relevant given their involvement in behaviors altered by loss of *Ndufs4*. The cerebellar fastigial nucleus regulates posture; the inferior olivary nucleus regulates motor coordination; and the vestibular nucleus regulates posture, respiration, and cardiovascular responses (Angelaki and Cullen, 2008; Quintana et al., 2010; Yates et al., 2002).

Our laboratory identified a large increase in the succination of voltage-dependent anion channel isoforms 1 (VDAC1) and 2 (VDAC2) at Cys77 and Cys48, which may further compromise the metabolic flux of the limited ATP generated through the outer mitochondrial membrane. Remarkably, while tubulin is abundantly succinated in the NDUSF4 KO brain, the levels of succination do not increase, illustrating disease-specific differences in the proteins targeted. We

further demonstrated the selectivity of protein succination with no increased modification observed in skeletal muscle tissue, a site that has no major pathology in the NDUFS4 KO mouse or humans with *NDUFS4* mutations (Kruse et al., 2008; Piroli et al., 2016; Leshinsky-Silver et al., 2009). Given the increased gliosis present in the necrotizing lesion environment of the NDUFS4 KO brain, itaconate is another potential metabolite that has not yet been explored (Fan et al., 2020; Bajwa et al., 2019; Yun et al., 2021; Quintana et al., 2010). Itaconate production by microglia has been described to be protective in the context of stroke-derived ischemia, generating protective *Hmox1* to attenuate infarct volumes (Kuo et al., 2021). Therefore, further investigation of itaconate production in the context of NDUFS4 KO gliosis will be of interest.

1.4.4 Gliosis. NDUFS4 KO olfactory bulb and vestibular nuclei brain lesions accumulate astrocytes around the lesions and microglia within the lesions (Quintana et al., 2010). This accumulation of astrocytes and microglia in NDUFS4 KO mouse brain lesions is correlated with increased disease severity and protein succination, suggesting potential immunometabolic interactions (Quintana et al., 2010; Piroli et al., 2016). The infiltration of other inflammatory cell types, including follicular cells, Th1 cells, Th17 cells, Tregs, dendritic cells, mast cells, and macrophages, was demonstrated in the brainstem of the vGlut2-specific knockout of *Ndufs4* (Bolea et al., 2019), although the extent to which these contribute to the neuroinflammatory status remains to be determined. While astrogliosis is beneficial to brain function in the short-term, long-term accumulation of astrocytes and microglia often prevents tissue regeneration and accelerates the damage to

surrounding neuronal tissues through chronic inflammatory signaling (Cavanagh et al., 1994; Guadagno et al., 2013; Yun et al., 2021; Takeda et al., 2021). Damaged neurons release damage-associated molecular patterns (DAMPs) that stimulate a pro-inflammatory phenotype in resident microglia and a positive feedback loop of neuroinflammatory damage (Fan et al., 2020; Bajwa et al., 2019; Yun et al., 2021). A glia-specific knockdown of NADH dehydrogenase (ubiquinone) 75 kDa subunit (*ND75)*, the homolog to human Complex I, in *Drosophilia* is sufficient to induce neuronal toxicity and mitochondrial dysfunction, indicating that microglia play an autonomous role in disease pathogenesis (Hegde et al., 2014). Therefore, sustained microgliosis within the necrotizing brain lesions may accelerate tissue damage through chronic neuroinflammation. Further exploration is required to determine the inflammatory state of NDUFS4 KO microglia in mice and to delineate the impact of knockout of NDUFS4 on microglial function.

In summary, several compounding factors may contribute to the pathogenesis of Leigh syndrome. The loss of *Ndufs4* at Complex I directly leads to an oxidative phosphorylation-derived ATP deficit, occurring in parallel with increased reductive stress, protein succination, and reactive gliosis. However, there remains much to explore on the mechanisms by which these factors and the interplay between them lead to Leigh syndrome pathology.

1.5 Treatment of Leigh Syndrome

1.5.1 Current Treatments for Leigh Syndrome. Current treatments for Leigh Syndrome patients employ a wide range of vitamins and antioxidants to

extend patient lifespan and quality of life, including coenzyme Q_{10}, riboflavin (B_2), folinic acid (B_9), thiamine, and lipoic acid. Coenzyme Q_{10} or ubiquinone is a component of the electron transport chain that transfers electrons from Complex I and II to Complex III. Supplementation with coenzyme Q_{10} or quinone analogs helps restore electron flow to the electron transport chain directly and increases mitochondrial antioxidant capacity through regenerating vitamin C and E (Hargreaves, 2014; Turunen et al., 2004). Riboflavin is part of flavin mononucleotide, a prosthetic group of Complex I. Treatment with riboflavin is especially important and effective in patients with a Complex I deficiency (Scholte et al., 1995; Gerards et al., 2011). Folinic acid is a supplement used to correct deficiencies in folate, a cofactor used in one-carbon metabolism for the biosynthesis and methylation of DNA and RNA (Garcia-Cazorla et al., 2008; Parikh et al., 2015). At best, these treatments only prolong a patient's lifespan by a few years.

1.5.2 Novel Therapeutic Approaches. Several pre-clinical studies have identified other promising treatments and targets in NDUFS4 KO mice. Ferrari *et al.* found that hypoxic conditions (specifically 11% O_2) from 30 d of age extended the lifespan of NDUFS4 KO mice (median survival at 270 d), reduced lactic acidosis, and prevented the development of necrotizing brain lesions (Ferrari et al., 2017). Genetic hypoxia-inducible factor activation is insufficient for these beneficial effects in the NDUFS4 KO mouse, which has a 2-fold increase in brain partial pressure of oxygen (PO_2) levels at P50 and 21% O_2 compared to age-matched WTs. However, chronic hypoxic and CO-rich (600 ppm) conditions

stabilized the brain PO_2 levels to WT levels, improved lifespan, and prevented the development of brain lesions in NDUFS4 KO mice. In addition, anemia induced by phlebotomy and an iron-deficient diet also stabilized NDUFS4 KO brain PO2 levels, improved lifespan, and prevented brain lesion development. As knockout of NDUFS4 leads to increased brain PO_2 and stimulating HIF in normoxic conditions can promote further increases in brain PO_2, the benefit of these treatments may be from reducing brain oxygen tensions (Ferrari et al., 2017; Jain et al., 2019). In addition, hyperoxia (55% O_2) is fatal for NDUFS4 KO mice within 10 d from pulmonary edema. Unfortunately, the beneficial effects of hypoxic conditions were not recapitulated in an intermittent (10 h each day) paradigm, perhaps limiting the clinical utility for Leigh Syndrome patients (Ferrari et al., 2017).

Recently, a novel approach was used to engineer an enzyme to alleviate intracellular redox imbalances by directly targeting metabolite imbalances (Patgiri et al., 2020). The enzyme, LOXCAT, was a fusion of lactate oxidase (LOX) and catalase (CAT) that irreversibly converts lactate and oxygen to pyruvate and water to reduce the lactate: pyruvate ratio and facilitate NADH oxidation to relieve reductive stress. Addition of LOXCAT lowered medium lactate: pyruvate ratios and improved cell growth in Complex I (*NDUFA9*), III (*UQCRB*), and V (*ATP5A1*) mutant K562 cells and Complex I (*NUBPL*) mutant patient fibroblasts. Finally, LOXCAT was fused with albumin-binding peptide (ABP) to prolong the half-life of LOXCAT *in vivo*. ABP-LOXCAT normalized blood lactate: pyruvate and brain and heart NADH: NAD^+ ratios in mice treated with the Complex I inhibitor metformin (Patgiri et al., 2020). Therefore, directly targeting elevated lactate: pyruvate and

NADH: NAD^+ ratios is viable *in vivo* and may provide therapeutic benefits in Leigh syndrome patients and NDUFS4 KO mice.

Lee *et al.* found that administration of nicotinamide mononucleotide (NMN, an NAD^+ precursor) to counter the reductive stress or dimethyl-ketoglutarate (DMKG, an α-ketoglutarate precursor that inhibits HIF-1α) improved the lifespan of NDUFS4 KO mice to 100 d (Lee et al., 2019). α-ketoglutarate supplementation may provide fuel that better supports Complex II-dependent respiration in NDUFS4 KO mice (Kayser et al., 2016).

Given the sensitivity to infection and chronic lesion microgliosis observed in Leigh syndrome patients and NDUFS4 KO mice, I hypothesize that the augmentation of itaconate using a cell-permeable itaconate ester may offer benefit in affected brain regions. 4-octyl itaconate (4OI) is a cell-permeable itaconate derivative that inhibits pro-inflammatory IL-1β production through modification of KEAP1 and stabilization of NRF2-induced increases in anti-inflammatory gene expression, including *Hmox1* (Mills et al., 2018; Muri et al., 2020). 4OI was selected for our study as it showed the most potent activation of the NRF2 target NAD(P)H:quinone oxidoreductase-1 (NQO1) of the several metabolite esters assessed (Mills et al,. 2018). In addition, 4OI inhibits pro-inflammatory increases in glycolytic activity and IL-1β and IL-6 cytokine production through alkylation and inhibition of lactate dehydrogenase and glyceraldehyde 3-phosphate dehydrogenase (GAPDH) (Muri et al., 2020; Liao et al., 2019; Mills et al., 2018; Swain et al., 2020). Therefore, in the context of investigating the activation of NDUFS4 KO macrophages and microglia, we explored the efficacy of 4OI

treatment on the motor endurance and coordination, body temperature, and disease severity of NDUFS4 KO mice.

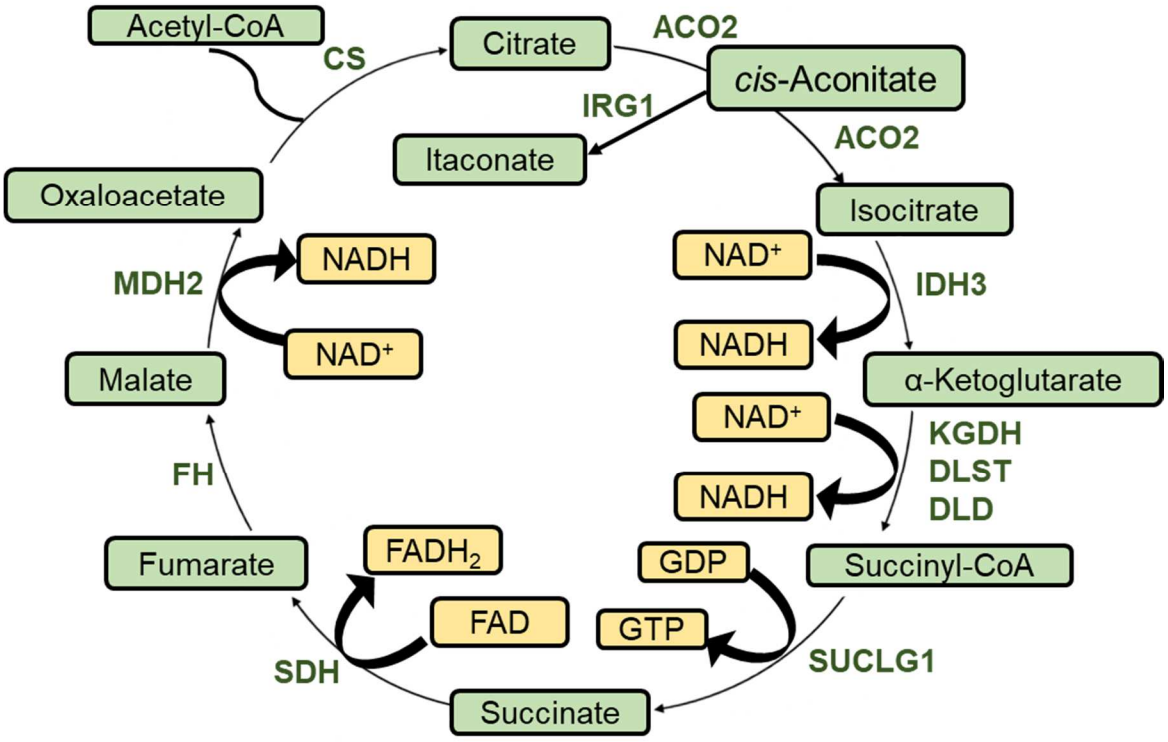

Figure 1.1 The Krebs Cycle. Acetyl-CoA enters the Krebs cycle operating in oxidative metabolism to generate 3 NADH, 1 GTP, and 1 $FADH_2$ for oxidative phosphorylation by the electron transport chain. The enzyme immune responsive gene 1 (IRG1) is included to highlight the synthesis of itaconate, a metabolite with important roles in immunometabolism, from *cis*-aconitate.

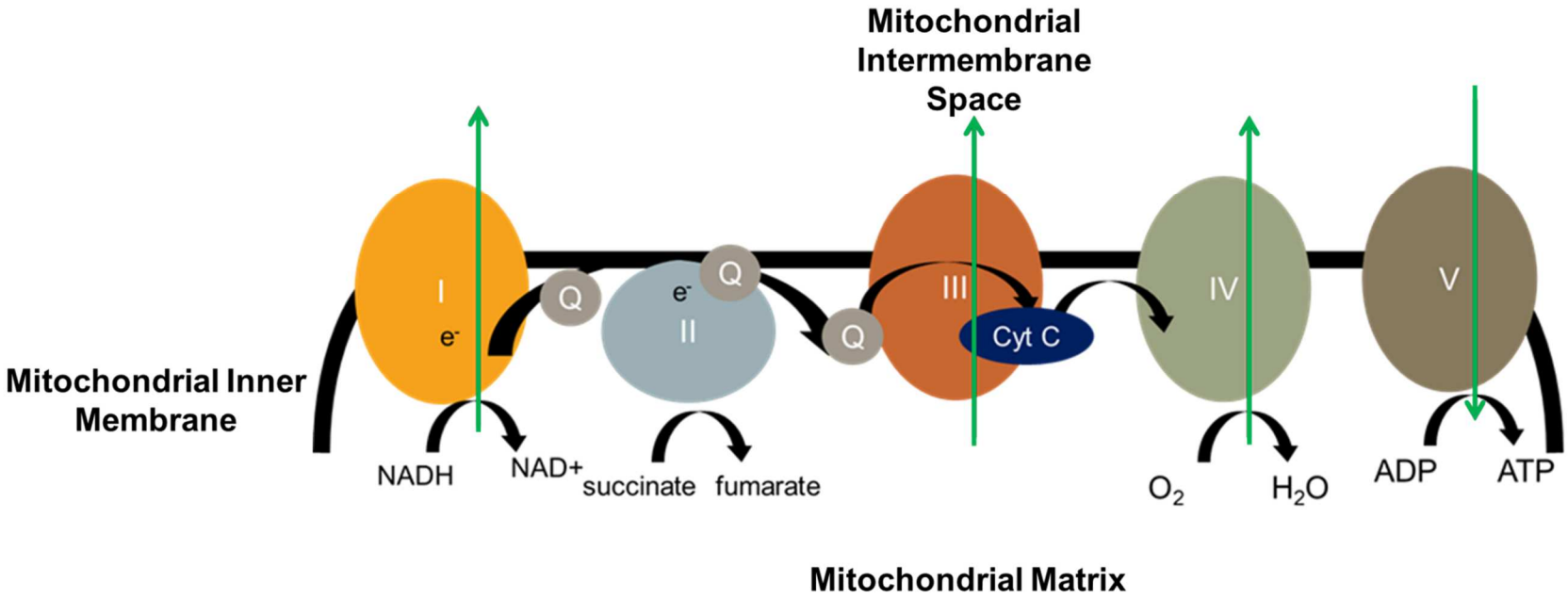

Figure 1.2 The Electron Transport Chain. Complexes I-IV of the electron transport chain use the high-energy intermediates (NADH and $FADH_2$) generated by the Krebs cycle to form a proton gradient across the mitochondrial inner membrane. Protons are pumped into the intermembrane space, as indicated by the green arrows, as the electrons (e^-) are transferred across the complexes. Complex V uses the potential energy of the proton gradient to form ATP as the protons return to the mitochondrial matrix.

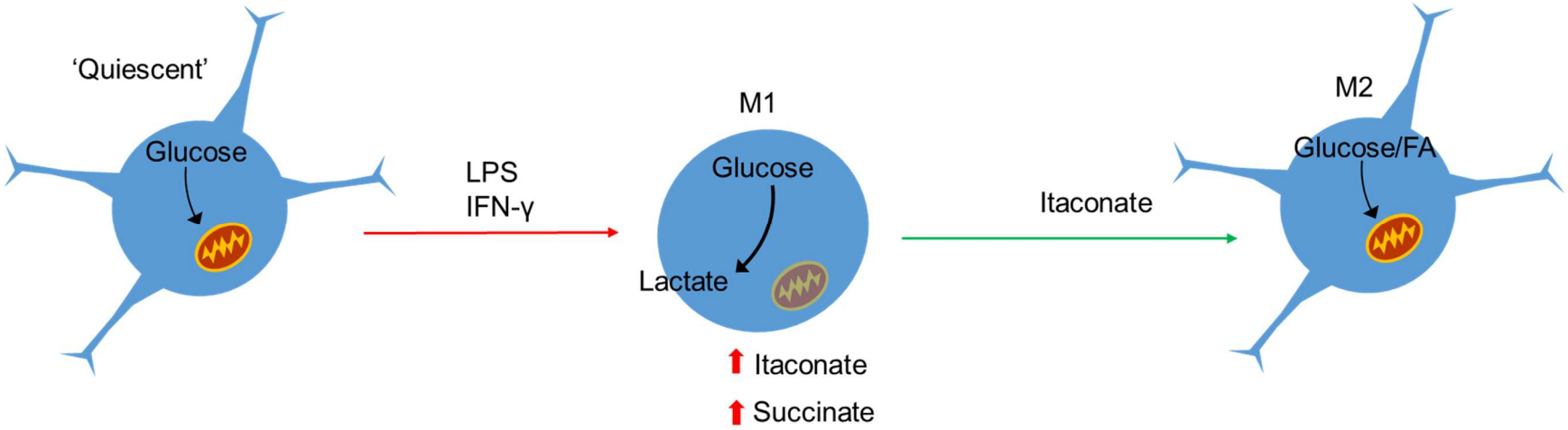

Figure 1.3 Macrophage and Microglial Metabolic Reprogramming. Quiescent macrophages metabolize glucose and generate ATP via oxidative metabolism. Pro-inflammatory stimuli, including LPS and IFN-γ, cause macrophages to undergo a metabolic switch by decreasing their oxidative phosphorylation and increasing their glycolytic metabolism as they enter the M1, or pro-inflammatory, state. The metabolic shift promotes Krebs cycle remodeling and the accumulation of itaconate and succinate. Persistent accumulated itaconate stimulates anti-inflammatory (M2) activity to resolve the inflammatory activation. Specific mechanisms by which these metabolites impact the inflammatory profile are shown in **Figure 1.4**.

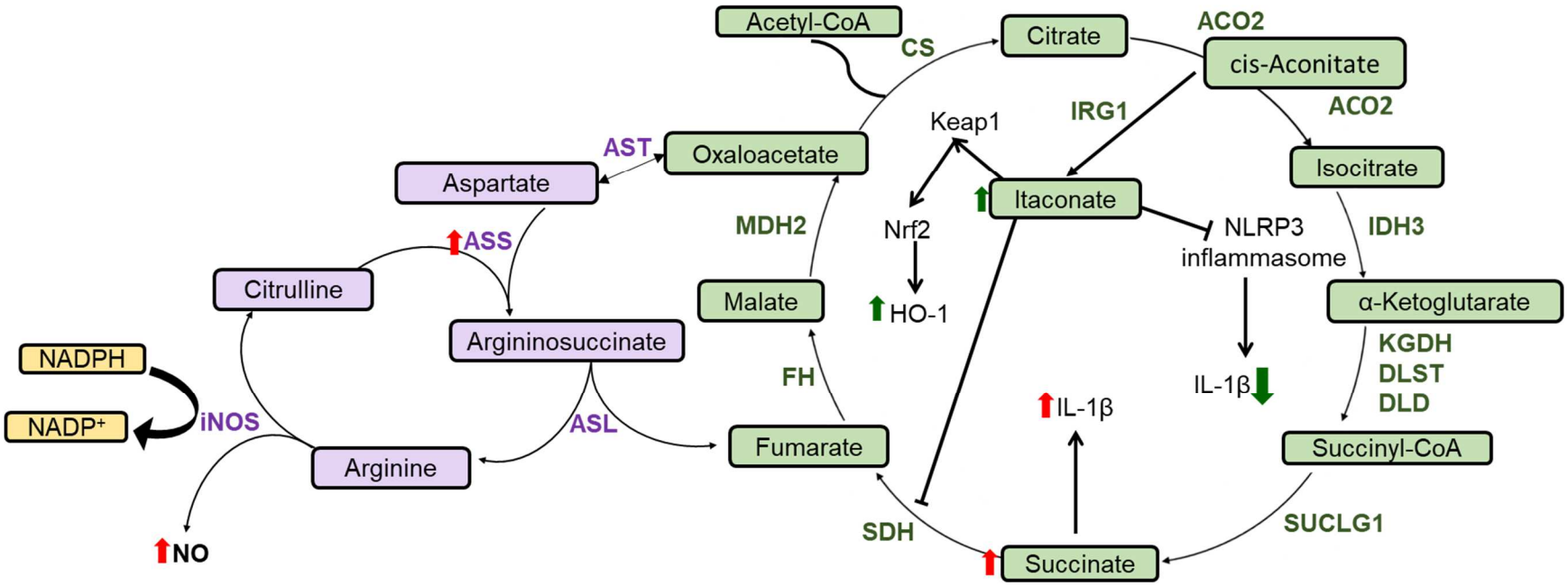

Figure 1.4 Immunometabolism: The Role of the Krebs Cycle and the Argininosuccinate Shunt. The Krebs Cycle is rewired during the cellular response to inflammation. Increased itaconate competitively inhibits SDH to promote succinate accumulation, increased IL-1β, and pro-inflammatory activity. Sustained itaconate dicarboxypropylates NLRP3, inhibiting IL-1β production. Itaconate also modifies KEAP1 to allow NRF2 to increase heme oxygenase-1 (HO-1) gene expression and promote anti-inflammatory activity. To sustain nitric oxide (NO), macrophages use the argininosuccinate shunt. Argininosuccinate is produced by upregulated argininosuccinate synthetase (ASS) using aspartate and citrulline. Argininosuccinate lyase (ASL) metabolizes the argininosuccinate to produce arginine and fumarate. Arginine is consumed by iNOS with NADPH to form NO, citrulline, and nicotinamide adenine dinucleotide phosphate ($NADP^+$). Fumarate anaplerotically supplies aspartate using mitochondrial aspartate aminotransferase (AST) in the malate-aspartate shuttle.

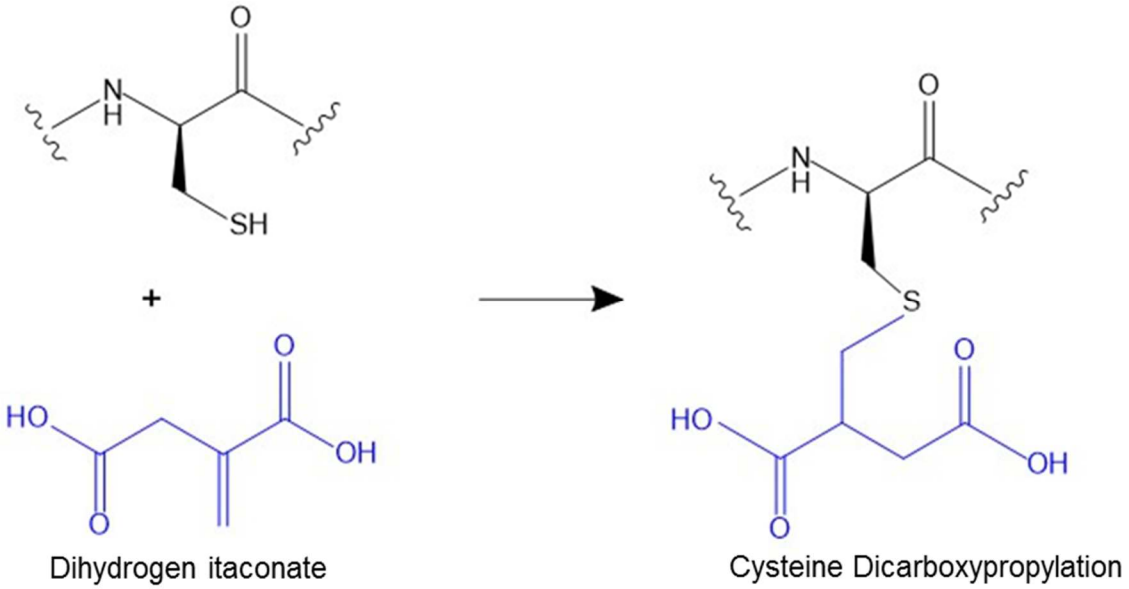

Figure 1.5 Protein Dicarboxypropylation by Itaconate. Itaconate irreversibly alkylates free cysteine thiols to generate 2,3-dicarboxypropylcysteine, referred to as protein dicarboxypropylation.

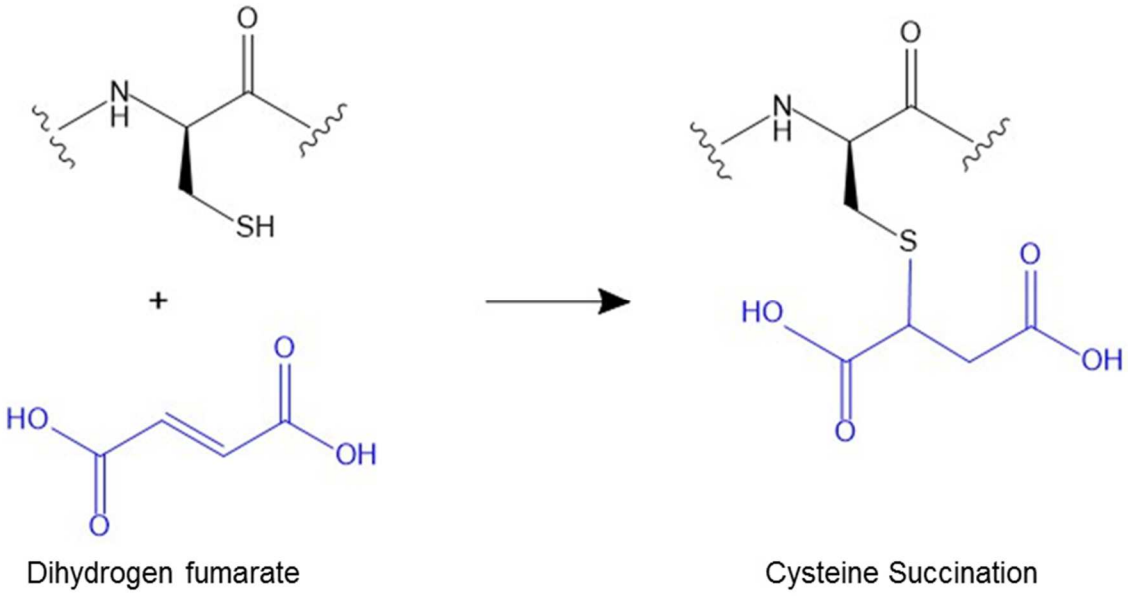

Figure 1.6 Protein Succination by Fumarate. Protonated fumarate irreversibly modifies free cysteine thiols through Michael addition to form S-2-succinocysteine, also known as protein succination.

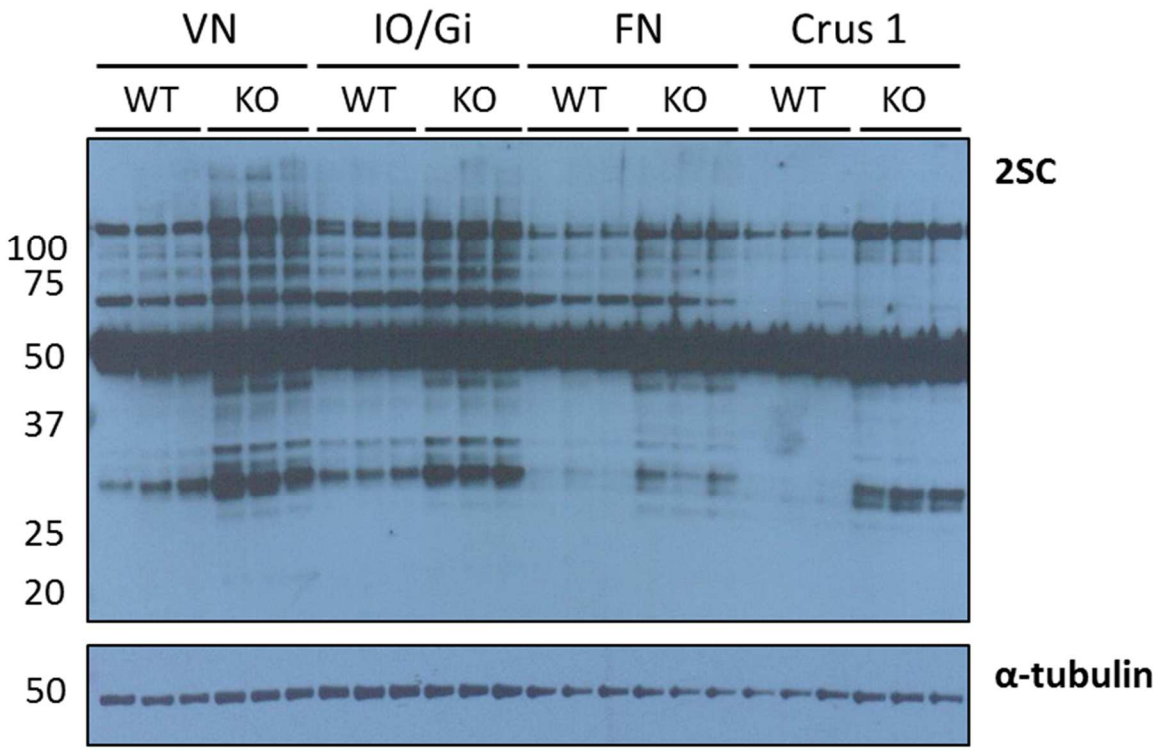

Figure 1.7 Protein Succination is Increased in the NDUFS4 Knockout brain. Regional brain tissue was collected from WT and NDUFS4 KO mice at P63. Micropunches (1 mm) of vestibular nuclei (VN) and inferior olive/gigantocellular reticular nucleus (IO/Gi) of the BS, and the fastigial nucleus (FN) and crus 1 ansiform lobule (Crus 1) of the cerebellum were homogenized, and proteins were separated by SDS-PAGE followed by immunoblotting. Probing of immunoblots with the anti-2SC antibody revealed increased protein succination in all the regions in the NDUFS4 KO mice, with more intense modification in the BS nuclei (2SC panel). The intensely modified band detected in both WT and KO at ~50 kDa was tubulin and was one of the most endogenously succinated proteins detected in the brain. α-tubulin was used as a loading control (α-tubulin panel).

Reprinted from *Molecular Cell Proteomics*. 12/2. Piroli, G.G., Manuel, A.M. Clapper, A.C., Walla, M.D., Baatz, J.E., Palmiter, R.D., Quintana, A., and Frizzell, N. Succination is Increased on Select Proteins in the Brainstem of the NADH dehydrogenase (ubiquinone) Fe-S protein 4 (Ndufs4) Knockout Mouse, a Model of Leigh Syndrome. 445-461. 2016

CHAPTER 2

LINKING ALTERED IMMUNOMETABOLISM TO AN IMPAIRED INFLAMMATORY RESPONSE IN THE NDUFS4 KNOCKOUT MOUSE MODEL OF LEIGH SYNDROME

McCain, R.S.[1], Swaminathan, S.S.[1], Smith, H.H.[1], Tran, E.[1], Piroli, G.G.[1], Cotham, W.E.[2], Walla, M.D.[2], Fan, D.[3] Quintana, A.[4], and Frizzell, N.[1]

1) Department of Pharmacology, Physiology & Neuroscience, School of Medicine, University of South Carolina, Columbia, SC 29209, USA
2) Department of Chemistry and Biochemistry, University of South Carolina, Columbia, SC 29208, USA
3) Department of Cell Biology and Anatomy, School of Medicine, University of South Carolina, Columbia, SC 29209, USA
4) Institut de Neurociències, Universitat Autònoma de Barcelona, Bellaterra (Barcelona), Spain

To be submitted

2.1 Introduction

Both Leigh syndrome patients and NDUFS4 KO mice develop unresolved lesions with marked microgliosis (van Erven et al., 1987; Finsterer, 2008; Kruse et al., 2008; Quintana et al., 2010). In addition, Leigh syndrome patients are particularly vulnerable to injury and infection as they accelerate the disease progression (Cavanagh and Harding, 1994; Van Coster et al., 1991). As the immune system is regulated by metabolism, mitochondrial bioenergetic deficits may impact the strength of the neuroimmune response.

Microglia, which respond to stimuli similar to macrophages, are the resident innate immune cells of the brain. Microglia and macrophages consume dead cells and debris through phagocytosis (Amici et al., 2017). During phagocytosis, the material is engulfed by the plasma membrane that forms an phagosome and then fuses with lysosomes. Lysosomes contain cathepsin proteases that are active at the acidic pH of the lysosomal interior, where they digest the engulfed material (Kim et al., 2020; Nakanishi 2020). The acidity of this compartment is maintained through the vacuolar H^+ ATPase (V-ATPase), a proton pump on the lysosomal transmembrane that consumes ATP (Mindell et al., 2012). More recently, phagocytosis has been shown to be crucial for the disposal of dysfunctional mitochondria expelled from neutrophils through mitocytosis to maintain the mitochondrial membrane potential and for pruning synapses in neurodevelopment (Amici et al., 2017; Jiao et al., 2021). Microglia and macrophages regulate the inflammatory state of the brain and periphery, respectively, through the release of pro and anti-inflammatory cytokines (Amici et al., 2017). In many cases, necrotic

neuronal lesions release DAMPs that induce a pro-inflammatory phenotype in resident microglia (Fan et al., 2020; Bajwa et al., 2019; Yun et al., 2021). Chronic stimulation of pro-inflammatory microglia triggers further neuronal death through TNFα-induced BAX activation and reactive oxygen species-associated damage (Guadagno et al., 2013; Yun et al., 2021; Takeda et al., 2021).

The original characterization of the NDUFS4 KO mouse brain by Quintana *et al.* documented a greater number of ionized calcium binding molecule 1 (IBA1) positive cells with a hypertrophic appearance in vacuolated areas of neuronal loss, namely the inferior olivary nucleus along with the surrounding gigantocellular and parapyramidal regions of the brainstem, the peri-glomerular outer plexiform layer of the OB, and the deep cerebellar nuclei (Quintana et al., 2010). In contrast, sparse, ramified microglia were present in the WT controls. Immunofluorescence to detect $CD11b^{+}$ microglia confirmed the presence of phagocytic cells in the lesioned regions, and GFAP positive astrocytes were present on the periphery of these areas. Staining with FluroJade C demonstrated degenerating neurons on the edges of the lesions (Quintana et al., 2010). Subsequent studies on NDUFS4 KO bone marrow-derived macrophages suggested a pro-inflammatory phenotype as a 2-fold increase in pro-inflammatory IL-1β gene expression was documented (Jin et al., 2014). Separately, mutation of mitochondrial polymerase gamma (*Polg*), a DNA polymerase whose mutation impairs mtDNA replication, led to mtDNA mediated activation of the pro-inflammatory DNA sensor cyclic GMP-AMP synthase (cGAS). cGAS promotes cGAS-stimulator of interferon genes (STING), driving Type I interferon inflammatory responses, including NRF2 inhibition (Lei et

al., 2021). The combined evidence from these studies suggested that active microglia in mitochondrial disease may manifest a pro-inflammatory phenotype. However, immunometabolic dysfunction in NDUFS4 KO microglia is understudied. Therefore, we sought to characterize the inflammatory phenotype of NDUFS4 KO microglia within the neuroinflammatory necrotizing lesions *in vivo* and to examine the effects of NDUFS4 KO on microglia and macrophages *in vitro*. We hypothesized that the cells would exhibit an M1-like pro-inflammatory phenotype where IL-1β was elevated within the necrotic regions and that impaired production of anti-inflammatory itaconate would prevent their polarization to an M2 phenotype, thereby sustaining inflammation.

2.2 Results

Given that necrotizing lesions develop in the NDUFS4 KO mouse olfactory bulb (OB) by the mid-stage of the disease (P26-38), we examined the gene expression of several inflammatory markers in P35-38 NDUFS4 knockout OB *in vivo* versus age-matched WTs (Quintana et al., 2010; de Haas et al., 2016). The NDUFS4 knockout OB was investigated as the lesions in this region contain the highest concentration of microglia (Quintana et al., 2010). We confirmed a significant increase in microglial presence through the ~16-fold increase in IBA1 protein in the NDUFS4 KO OB by immunoblotting (**Figure 2.1**). In addition, ≥2-fold increases in *Iba1*, *Trem2*, and *CD68* gene expression in the NDUFS4 knockout OB (**Figure 2.2**) were detected by real-time quantitative polymerase chain reaction (qRT-PCR). The assessment of the expression of pro-inflammatory cytokine genes (*Il1b*, *Il6*, *Tnfa*, *Il17*, *Irf3*, and *Irf7*) and the inflammasome sensor gene *Nlrp3*

revealed no increase in the OB (**Figure 2.3, 2.4**). *Irf3* and *Irf7* expression were unchanged, suggesting no basal engagement of the cGAS-STING-IFN-I axis previously described in the POLG mutator mice (**Figure 2.4A-B**) (Lei et al., 2021). Previous transcriptional profiling of conditional *Ndufs4* KO mouse brainstem suggested enrichment of select pro-inflammatory T helper cells, including Th17. However, *Il17* expression was not elevated (**Figure 2.4C**) (Bolea et al., 2019). The levels of *Il12* and *Arg1* were not significantly changed (**Figure 2.5**). We also quantified the expression levels of *Irg1*, which facilitates itaconate production, and anti-inflammatory *Hmox1* and *Il10* and found no significant differences in KO vs. WT olfactory bulb (**Figure 2.6**), suggesting limited inflammatory cytokine production by the resident microglia in the lesions. Quantification of IL-1β and IL-10 protein confirmed no detectable levels of these cytokines in the OB tissue or serum of the KO and WT mice (not shown). Since we were profiling the OB at ~P35 when more IBA1 positive cells were present, we next examined an earlier time point as Jin *et al.* found increased pro-inflammatory signaling in the periphery of P22 NDUFS4 KO mice (Jin et al., 2014). We quantified peripheral (liver) and OB levels of *Il1b*, *Tnfa*, *Il12*, *Nlrp3*, and *Iba1*. While we confirmed the expected increase in Iba1 in the OB, we found no increase in the expression of other genes in the OB or livers of the P22 mice (**Figure 2.7**).

Although hypertrophic microglia accumulate in the pathologically affected brain regions (Quintana et al., 2010), we considered that the absence of NDUFS4 might impact the ability of microglial mitochondria to adapt during activation, thereby impacting the production of inflammatory mediators. Given that the Krebs

cycle is central to immune cell activation, in part by significantly increasing succinate and itaconate (**Figure 1.4**) (Lampropoulou et al., 2016; Seim et al., 2019), we quantified the levels of TCA intermediates in the KO vs. WT OB by mass spectrometry. NDUFS4 knockout OBs exhibit a $\geq$2-fold increase in fumarate, pyruvate, malate, and isocitrate. However, itaconate levels were not significantly increased, and a significant decrease in succinate was detected compared to WT controls (**Figures 2.8, 2.9**). The lack of itaconate and succinate alteration parallels the absence of increases in inflammatory cytokine gene expression but is surprising given the prevalent neuroinflammatory component of the NDUFS4 knockout OB.

Since the OB contains a mixed cell population, including the degenerating neurons, we examined the metabolic profile of WT and NDUFS4 KO peritoneal macrophages as they respond to stimulation in a phenotypically similar manner to microglia. Unlike bone marrow-derived macrophages (BMDMs), the peritoneal macrophages are differentiated *in vivo* prior to collection and can be reliably obtained from the young NDUFS4 KO mice (Amici et al., 2017). The peritoneal macrophages were challenged with lipopolysaccharide (LPS) to elicit their response to an inflammatory stimulus. Primary peritoneal macrophages were stimulated for 1 h with 100 ng/mL LPS as this dose is commonly used to stimulate a pro-inflammatory response in macrophages (Mills et al., 2018; Liao et al., 2019; Swain et al., 2020), and their respiratory profile was analyzed following both mitochondrial and glycolytic metabolic stress tests in an extracellular flux analyzer. Measurement of basal respiration and ATP production under unstimulated

conditions confirmed that NDUFS4 KO macrophages had ~50% of the capacity of unstimulated WT macrophages. LPS stimulation significantly reduced mitochondrial oxygen consumption and ATP production, as expected (Tannahill et al., 2013; Tannahill et al., 2015), by 50% in both phenotypes (**Figure 2.10A-B**). Assessment of glycolytic metabolism demonstrated that NDUFS4 KO macrophages operate at maximal glycolytic capacity, with little to no glycolytic reserve under basal conditions (**Figure 2.10C-D**). The lack of glycolytic reserve is indicative of an impaired metabolic capacity in response to stressors (McDowell et al., 2020). LPS-stimulation of both WT and NDUFS4 KO macrophages increased the rate of glycolysis by ≥2-fold. However, WT macrophages had a more robust increase in their glycolytic reserve versus NDUFS4 KO macrophages in response to LPS stimulation (**Figure 2.10D**), confirming impaired metabolic flexibility when acutely challenged. Therefore, while both WT and NDUFS4 KO macrophages respond to LPS stimulation by increasing their glycolytic metabolism, their capacity to maximally respond is diminished in the KO cells, which may be significant in the necrotic lesion environment where NDUFS4 KO microglia accumulate.

Given that the NDUFS4 KO macrophages exhibited altered LPS-induced metabolic responses, we analyzed the expression of pro-inflammatory *Tnfa*, *Il1b*, and *Il6*, as well as *Irg1*, *Hmox1*, and *Il10* following LPS stimulation by qRT-PCR. While *Tnfa* expression was induced to a similar level in WT and NDUFS4 KO macrophages stimulated by LPS (**Figure 2.11A**), both *Il1b* and *Il6* were expressed at ~10-fold higher levels in LPS-stimulated WT macrophages versus stimulated KO cells (**Figure 2.11B-C**). The expression of *Irg1* was robustly increased in both

genotypes in response to LPS with a 400-fold increase in WT cells and a 130-fold increase in KO cells (**Figure 2.12A**). *Il10* expression was significantly increased by 20-fold in WT cells, but only 2.5-fold in KO cells, by LPS stimulation (**Figure 2.12B**). In addition, immunoblotting to detect cleaved IL-1β and HO-1 levels confirmed these findings at the protein level. Pronounced reductions in IL-1β and HO-1 levels were observed in the stimulated NDUFS4 KO macrophages vs. WT (**Figure 2.13**).

Since the levels of CD68, a lysosomal membrane protein (Walker and Leu, 2015), were increased in the NDUFS4 KO OB (**Figure 2.2C**), and Quintana *et al.* detected increased phagocytic $CD11b^+$ microglia in the OB lesions (Quintana et al., 2010), we sought to determine whether loss of NDUFS4 altered phagocytic activity. Both WT and NDUFS4 KO macrophages increase the uptake of fluorescently labeled latex beads in response to LPS (**Figure 2.14A**). However, the LPS-stimulated increase in phagocytic uptake trended 50% lower in KO macrophages versus WT counterparts. The LPS-stimulated WT macrophages demonstrated a 3.1-fold increase in bead uptake, whereas the LPS-stimulated KO macrophages showed only a 2.4-fold increase versus their respective controls. This diminished response indicates that the capacity for phagocytic uptake in the NDUFS4 KO macrophages is lower, mirroring the impairments observed in inflammatory cytokine production (**Figure 2.11, 2.12, 2.13, 2.14**). We examined the OB expression of *Ctsb* and *Ctsd* as Cathepsins B and D are both abundantly expressed in active microglia and are crucial for the digestion and clearance of lysosomal debris (Kim et al., 2020; Nakanishi et al., 2020). Despite elevated $IBA1^+$

microglia, the expression of *Ctsb* was significantly reduced in the Ndufs4 KO OB compared to WT controls (**Figure 2.14B-C**). This data suggests that although the macrophages and microglia can respond to inflammatory and environmental stimuli, knockout of NDUFS4 limits the extent of the increase in cytokine signaling and phagocytic activity *in vivo* and *in vitro*.

As the loss of *Ndufs4* altered the metabolic poise of the macrophages, we further investigated how TCA cycle metabolism was impacted in NDUFS4 KO macrophages following LPS stimulation. Our laboratory has used an antibody, anti-2SC antibody, that detects fumarate modified proteins (protein succination) as a readout of elevated fumarate (Alderson et al., 2006; Nagai et al., 2007; Frizzell et al., 2009) and has shown elevated regional succination in the NDUFS4 KO brain (**Figure 1.7**, Piroli et al., 2016). We first examined the levels of protein succination in unstimulated and LPS-stimulated WT and NDUFS4 KO peritoneal macrophages. LPS treatment globally increased metabolite-induced protein modification (**Figure 2.15**). The intensity of the modified protein bands detected was greater in WT macrophages treated with LPS than in NDUFS4 KO macrophages treated with LPS, except for a band at ~50 kDa that was detected only in the KO macrophages prior to LPS stimulation (**Figure 2.15**, red arrow). TCA metabolites were quantified by LC-MS/MS in WT and NDUFS4 KO macrophages with or without LPS treatment. Surprisingly, the levels of fumarate were decreased in WT macrophages after LPS stimulation (**Figure 2.16A**), contrasting with anti-2SC detection (**Figure 2.15**). Fumarate levels slightly increased in NDUFS4 KO macrophages after 18h LPS stimulation, but this increase was not significant. Both

itaconate and succinate were significantly increased in LPS stimulated WT macrophages, with a ~40-fold increase in itaconate and a 2-fold increase in succinate levels. LPS-stimulated NDUFS4 KO macrophages showed a 10-fold elevation in itaconate, and no increase in succinate levels, as expected (**Figure 2.16-1**7) (Cordes et al., 2016). The striking reductions in both itaconate and succinate suggest that an impaired ability to rewire the TCA cycle in response to the LPS challenge, underlying the defective NDUFS4 KO inflammatory response.

To further understand the abundance of 2SC-positive protein modification during LPS stimulation, in the absence of increased fumarate, we used the HAPI microglial cell line as an alternative model (Cheepsunthorn et al., 2001). Immunodetection using anti-2SC antibody confirmed an increase in protein modification following 18 h LPS stimulation (**Figure 2.18A**). Primary cultures of microglia from WT mice challenged with LPS also showed increased modification on select proteins using the anti-2SC antibody (**Figure 2.18B**). We considered the structural similarity between fumarate-induced protein succination and itaconate-induced dicarboxypropylation, with both adducts displaying a succinate moiety that might be recognized by the anti-2SC antibody (**Figure 2.19A**). Therefore, we sought to determine whether the anti-2SC antibody might also detect itaconate-derived protein dicarboxypropylation. Unstimulated, control HAPI cell lysates were treated ±10 mM itaconate for 24 h followed by immunoblotting alongside LPS-stimulated HAPI cells as a positive control for antibody detection. **Figure 2.19B** demonstrates that itaconate-derived adducts are detected on proteins by the anti-2SC antibody. The label ‘anti-2SC/succinate moiety’ on these immunoblots reflects

that the antibody previously referred to exclusively as anti-2SC actually recognizes a succinate moiety present after cysteine modification by either fumarate or itaconate. The lower panel shows a slightly longer exposure where detection is enhanced, and **Figure 2.20A** demonstrates dramatic itaconate-derived protein modification when exposure was extended to detect maximal modification. In addition to our anti-2SC antibody (Nagai et al., 2007), a commercially available anti-2SC antibody (Discovery Antibodies®) has been marketed to confirm fumarate-derived protein modification (Burgener et al., 2019; Casey et al., 2020; Gupta et al., 2020; Äyräväinen et al., 2020). Duplicate immunoblots comparing our anti-2SC preparation to the commercial antibody demonstrated similar detection of itaconate-derived protein dicarboxypropylation (**Figure 2.20B**). Therefore, currently available antibodies that detect succinated protein cysteines also detect dicarboxypropylated protein cysteines, therefore, caution should be taken when interpreting data where active immune cells may also be present and producing itaconate. LC-MS/MS analysis of Krebs cycle metabolites confirmed a significant >10-fold increase in itaconate and no change in fumarate levels in response to LPS stimulation in the HAPI cells (**Figure 2.21A-B**). In parallel with itaconate, succinate levels were also increased by 1.5-fold, isocitrate levels were decreased by 0.6-fold, and other metabolites were unchanged (**Figure 2.21C, 2.22**). Shorter incubations with LPS for 3 h also confirmed a 4-fold increase in itaconate and no change in fumarate levels in HAPI microglia (**Figure 2.23, 2.24**).

While examination of LPS-induced changes in metabolites confirms the impaired macrophage/microglial response to acute inflammation, our studies

originally sought to characterize the microglia accumulating in lesions in response to neurodegeneration. We previously detected fumarate-driven protein succination in the pathologically affected brain regions, including the brainstem, and confirmed this in the olfactory bulb (**Figure 2.25A**). As both HAPI cells and primary microglia showed increased dicarboxypropylation in response to LPS (**Figure 2.18**), we isolated primary $CD11b^{+}$ WT and NDUFS4 KO microglia exclusively from the olfactory bulb and brainstem to determine whether *Ndufs4* loss increased metabolite-induced protein modification *in vivo*. Immunoblotting did not detect any increase in fumarate or itaconate-induced protein modification in NDUFS4 KO OB and BS microglia *in vivo* (**Figure 2.25B**), despite abundant enrichment of IBA1 positive microglia. Furthermore, the $CD11b^{-}$ flow-through (non-glial cell types) did not have detectable levels of IBA1 and showed increased metabolite-induced protein modification in the NDUFS4 KO OB and BS mix (**Figure 2.25C**). Therefore, neither protein succination nor dicarboxypropylation is increased in the NDUFS4 KO microglia, reflecting the impaired generation of itaconate in the OB. The increase in fumarate that was detected in the OB (**Figure 2.8**) drives the increase in protein succination that is observed in non-microglial cells (**Figure 2.25A**). The limited immunometabolism of the NDUFS4 KO macrophages and microglia may explain the lack of inflammatory factors and reduced phagocytosis within the lesions of the NDUFS4 KO OB, sustaining microgliosis (**Figure 2.26**).

2.3 Discussion

Despite abundant and sustained microglial presence, we did not detect an increase in inflammatory metabolite production or cytokine generation in the OB

lesions within the NDUFS4 KO mouse. The lack of inflammatory cytokine detection within the region typically described as ‘neuroinflammation’ was initially surprising, as the microglia were present but did not show a pro-inflammatory phenotype in the presence of neuronal degeneration. These findings contrast with the report of Jin *et al.*, in which Complex I was viewed as an inflammatory suppressor, and its absence was associated with elevated basal levels of inflammation. However, more recent studies align with our findings that inflammatory cytokines do not drive pathological neuroinflammation as NDUFS4 knockout BMDM did not show increased expression of inflammatory markers (Miller et al., 2021).

The peritoneal macrophages provided a model to acutely challenge immune cells (with LPS) to determine their capacity to respond. This was used to model a different metabolic challenge, such as exposure to an infection in the NDUFS4 KO mice. Macrophages demonstrated that knockout of NDUFS4 shifted metabolism from oxidative phosphorylation to glycolysis. However, the already limited glycolytic reserve was decreased further in NDUFS4 KO macrophages during LPS-stimulation, significantly impairing the cellular responsiveness to further stressors in challenging environments. NDUFS4 KO macrophages had reductions in LPS-stimulated accumulation of immunometabolites itaconate and succinate, contributing to the measured impairments in inflammatory signaling and phagocytic activity. Therefore, pro-inflammatory and anti-inflammatory phenotypes are impaired due to NDUFS4 deficiency, potentially exacerbating the microgliosis observed in the affected brain regions.

Electron microscopy demonstrated that the phagocytic microglia that accumulate adjacent to degenerating neurons in NDUFS4 KO mice have multiple lipid-rich inclusions (Quintana et al., 2010). A more recent study confirmed increased lipid droplet accumulation in NDUFS4 KO OB and VN microglia and astrocytes (Quintana et al., 2010). Lipid droplets are lipid-storing organelles, and the accumulation of lipid droplets is a marker of cellular inflammation and stress in non-adipocytes because of lipid peroxidation by reactive oxygen species (Liu et al., 2015). Lipid-droplet accumulating aged microglia have impaired phagocytic uptake, increased reactive oxygen species production, and exaggerated LPS-stimulated release of pro-inflammatory IL-1β, TNFα, and IL-6 and anti-inflammatory IL-10 (Marschallinger et al., 2020). Therefore, lipid droplet accumulation in vivo may impair NDUFS4 KO microglial activity. This impairment, along with the NDUFS4 KO-induced impairments to glycolytic reserves (**Figure 2.10**) and accumulation of inflammatory metabolites (**Figure 2.16**), may explain the lack of pro-inflammatory signaling within the necrotizing lesion environment. Given that phagocytic activity is also reliant on ATP-dependent vacuolar proton pumps to acidify the lysosome (Mindell et al., 2012), it is possible that the NDUFS4 KO microglia cannot sustain sufficient ATP production to maintain optimal cathepsin protease activity. The microglia recruited to remove degenerating neurons may ultimately become exhausted in the absence of sufficient ATP generation (Marschallinger et al., 2020; Liu et al., 2015).

While microglia and peritoneal macrophages are differentiated in the NDUFS4 KO mice and fulfill similar functional roles, there may be differences

between the inflammatory capacity of NDUFS4 KO intraperitoneal macrophages and microglia that merit further study. In addition, LPS is commonly coupled with IFN-γ for pro-inflammatory stimulation (Rattigan et al., 2018; Jha et al., 2015). While the addition of IFN-γ may alter the fluctuations of metabolites, the overall impairments resulted from NDUFS4 deficiency will likely remain unchanged. Therefore, evaluating the differences between NDUFS4 KO microglia and macrophages, in addition to how different inflammatory stimuli alter the metabolic flux of NDUFS4 KO microglia, remains an important direction for future studies.

Previous studies have relied on anti-2SC antibodies to identify fumarate-induced protein succination (Gupta et al., 2020; Alderson et al., 2006). Here we demonstrated that NDUFS4 KO microglia isolated from lesions did not show increased protein dicarboxypropylation, reflecting the limited generation of itaconate in the glia. In contrast, abundant fumarate accumulation parallels detection of protein succination in the OB and non-microglial component, suggesting that the majority of succinate moiety detected by the anti-2SC antibody in the NDUFS4 KO is due to fumarate-mediated succination in neurons (Piroli et al., 2016; Piroli et al., 2021). These results also highlight that this antibody should also be considered an important tool for confirmation of active immunometabolism, given its ability to detect the fumarate and itaconate-derived succinate moiety in parallel with metabolomics. Our laboratory routinely verifies fumarate-modified cysteine residues by mass spectrometry using the mass of the fumarate adduct (Piroli et al., 2016; Manuel et al., 2017). Future detection of fumarate and itaconate-induced protein modifications should be verified by mass spectrometry.

Future identification of abundant modified proteins detected by the antibody will contribute to our expanding understanding of the role of itaconate in regulating macrophage activity.

We were surprised to note that LPS stimulation did not increase fumarate production in peritoneal macrophages or microglia, considering the proposed role of the argininosuccinate shunt to supply nitric oxide during inflammation. Prior studies using bone marrow-derived macrophages had documented increased fumarate (Tannahill et al., 2013; Jha et al., 2015; Rattigan et al., 2018). Anaplerotic fumarate generated by the argininosuccinate shunt during inflammation can be used to support the TCA cycle after the SDH breakpoint (**Figure 1.4**). The utilization of fumarate in these circumstances suggests that fumarate is less likely to accumulate, and this has been documented by others as well. For example, Fall *et al.* observed increased argininosuccinate but not fumarate in LPS-treated lung alveolar macrophages (Fall et al., 2020).

We found that NDUFS4 KO microglia and macrophages have several metabolic deficiencies in response to a pro-inflammatory stimulus. This includes an impaired glycolytic reserve, itaconate accumulation, and thus succinate accumulation. These immunometabolite deficiencies are coupled with impairments in inflammatory signaling and phagocytic activity, preventing the proper pro-inflammatory response within the necrotizing neuronal lesions. Therefore, targeted treatment of impaired microglia may assist in resolving the necrotizing lesions in NDUFS4 KO mice and Leigh syndrome patients.

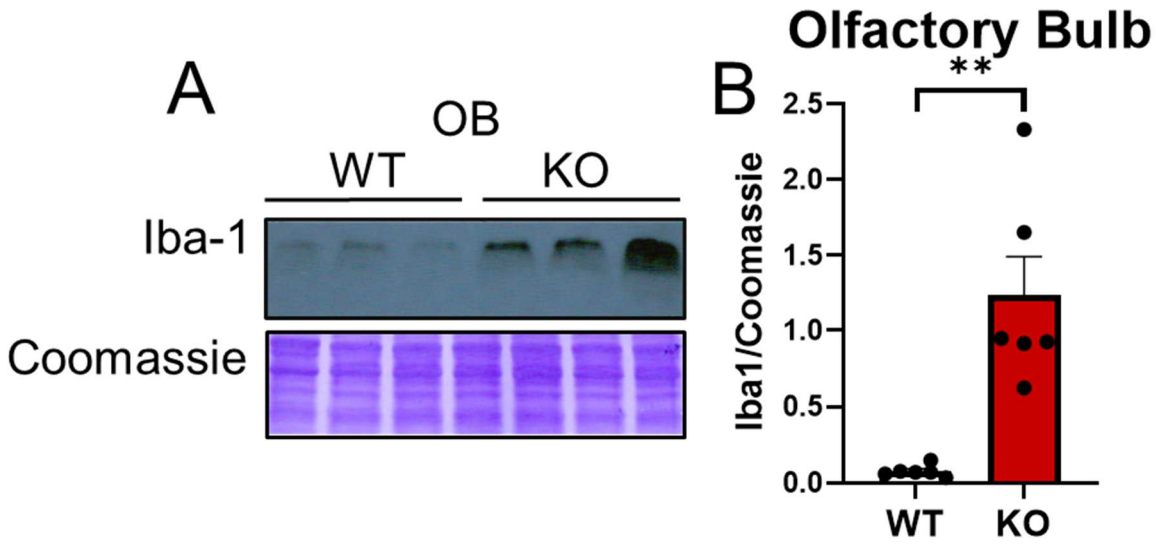

Figure 2.1 NDUFS4 Knockout Microglia Are Increased in the Olfactory Bulb *in vivo*. A: Protein lysates from P35-38 WT and NDUFS4 KO OBs (20 µg protein) were separated by SDS-PAGE, and immunoblotting was performed to detect IBA1 levels (17 kDa). The representative blot shows a pronounced increase in the IBA1 content in the NDUFS4 KO. Coomassie staining was used as a loading control. **B**: Quantification of P35-38 WT and NDUFS4 KO OB Iba1 content used Coomassie staining as a loading control. NDUFS4 KO OB Iba1 is 16-fold higher than WT controls. Data are mean ± SE (**p < 0.01; unpaired t-test with Welch's correction) with n=6/group.

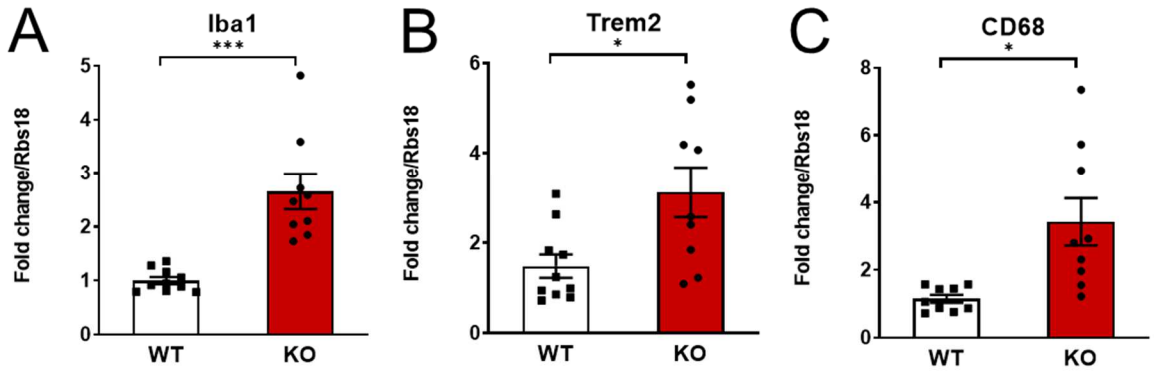

Figure 2.2 NDUFS4 Knockout Microglial Gene Expression Is Increased in the Olfactory Bulb *in vivo*. A-C: Gene expression in the OB of P35-38 WT and NDUFS4 KO mice was quantified by qRT-PCR. Increased expression of microglial markers (*Iba1*, *Trem2*, *CD68*) was confirmed in the NDUFS4 KO OB. Data are mean ± SE (*p < 0.05; ***p < 0.001; unpaired t-test with Welch's correction) with n=9-10/group.

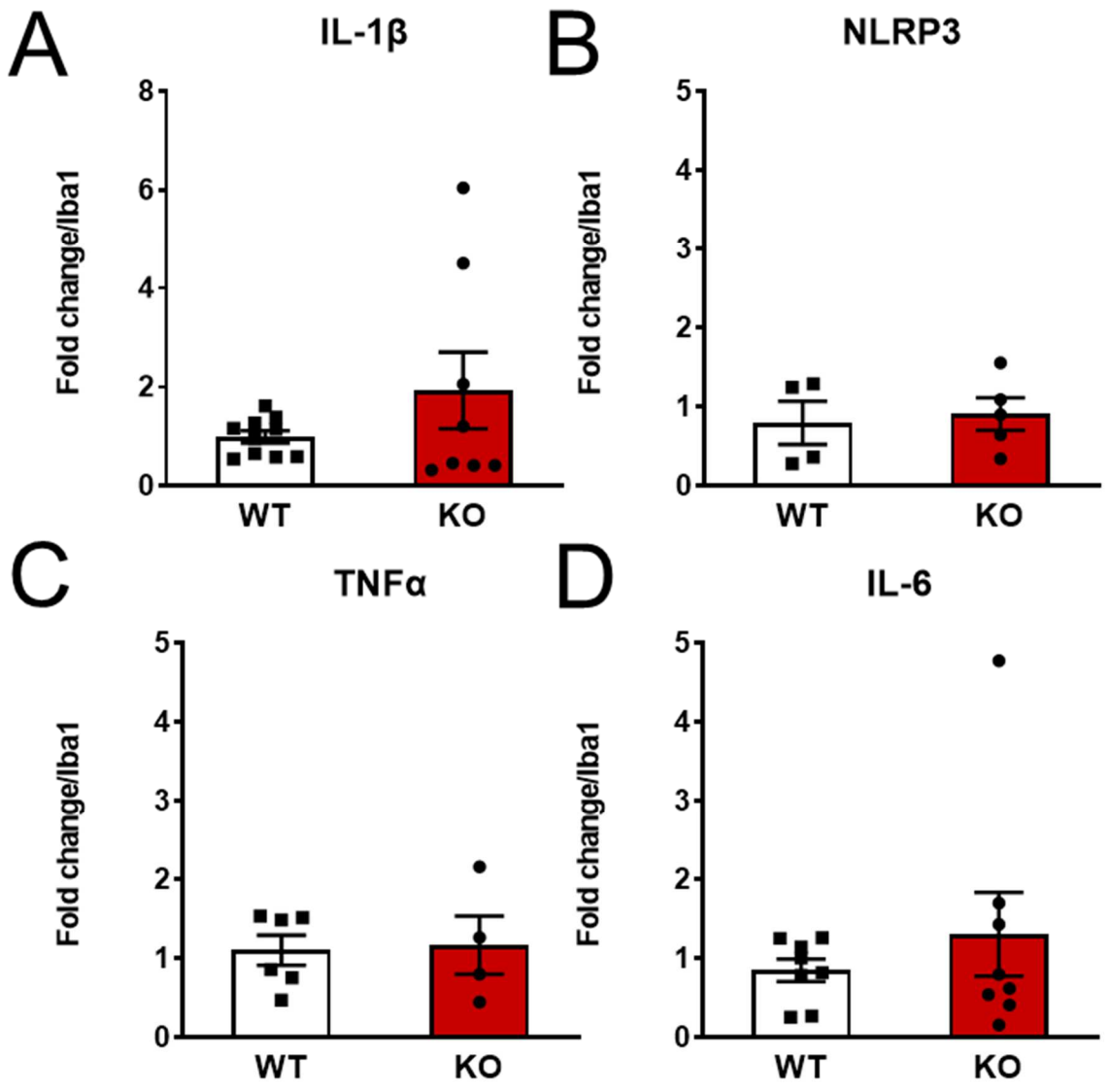

Figure 2.3 Pro-Inflammatory Factors Are Not Increased in the NDUFS4 Knockout OB. A-D: Gene expression in the OB of P35-38 WT and NDUFS4 KO mice was measured by qRT-PCR. No increases in pro-inflammatory (*Il1b*, *Nlrp3*, *Il6*, *Tnfa*) cytokine expression were detected in the OB with knockout of NDUFS4. Data are mean ± SE (unpaired t-test with Welch's correction) with n=4-10/group.

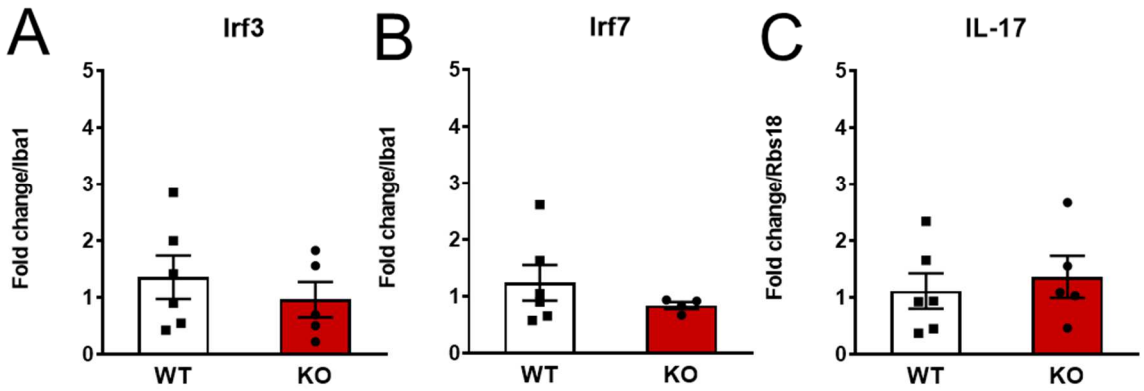

Figure 2.4 Pro-Inflammatory Factors Are Not Increased in the NDUFS4 Knockout OB. A-C: Gene expression in the OB of P35-38 WT and NDUFS4 KO mice was measured by qRT-PCR. Knockout of NDUFS4 did not increase pro-inflammatory *Irf3*, *Irf7*, and *Il17* expression in the OB. Data are mean ± SE (unpaired t-test with Welch's correction) with n=4-6/group.

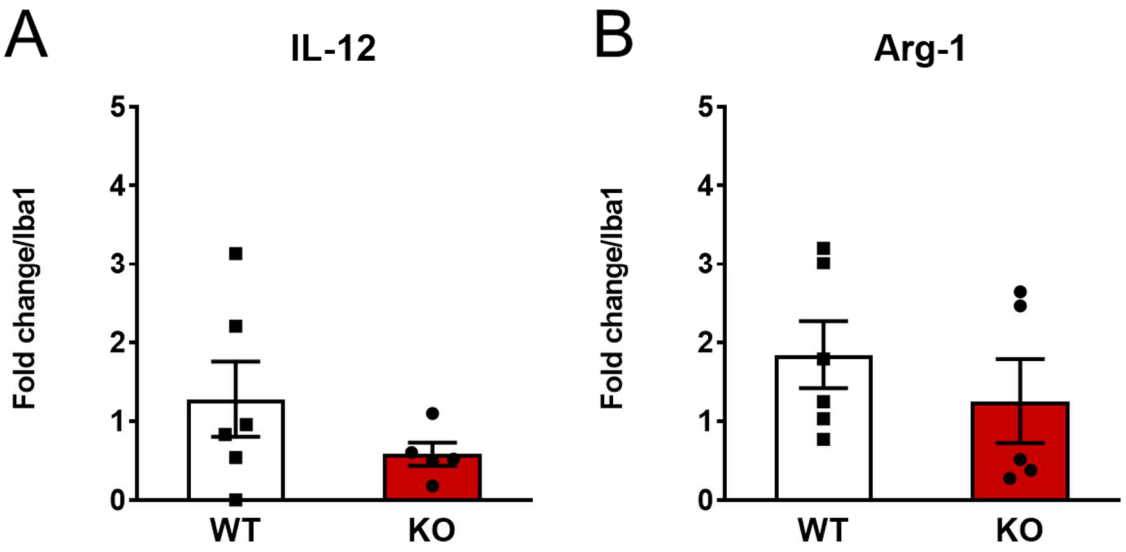

Figure 2.5 Pro-Inflammatory Factors Are Not Increased in the NDUFS4 Knockout OB. A-B: Gene expression in the OB of P35-38 WT and NDUFS4 KO mice was measured by qRT-PCR. No increases in pro-inflammatory *Il12* and *Arg1* expression were detected with knockout of NDUFS4. Data are mean ± SE (unpaired t-test with Welch's correction) with n=6/group.

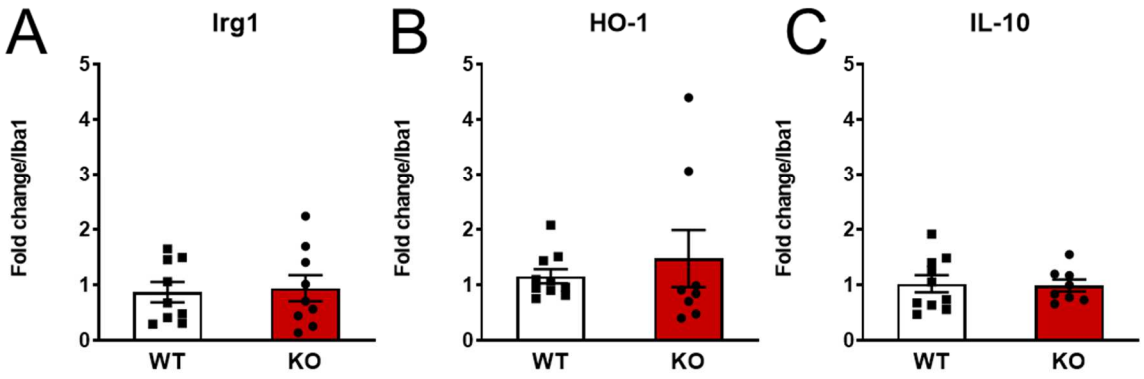

Figure 2.6 Anti-Inflammatory Factors Are Not Increased in the NDUFS4 Knockout OB. A-C: Gene expression from P35-38 WT and NDUFS4 KO OBs was measured by qRT-PCR. Knockout of NDUFS4 did not alter the expression of anti-inflammatory *Irg1*, *Hmox1*, and *Il10* detected in the OB. Data are mean ± SE (unpaired t-test with Welch's correction) with n=8-10/group.

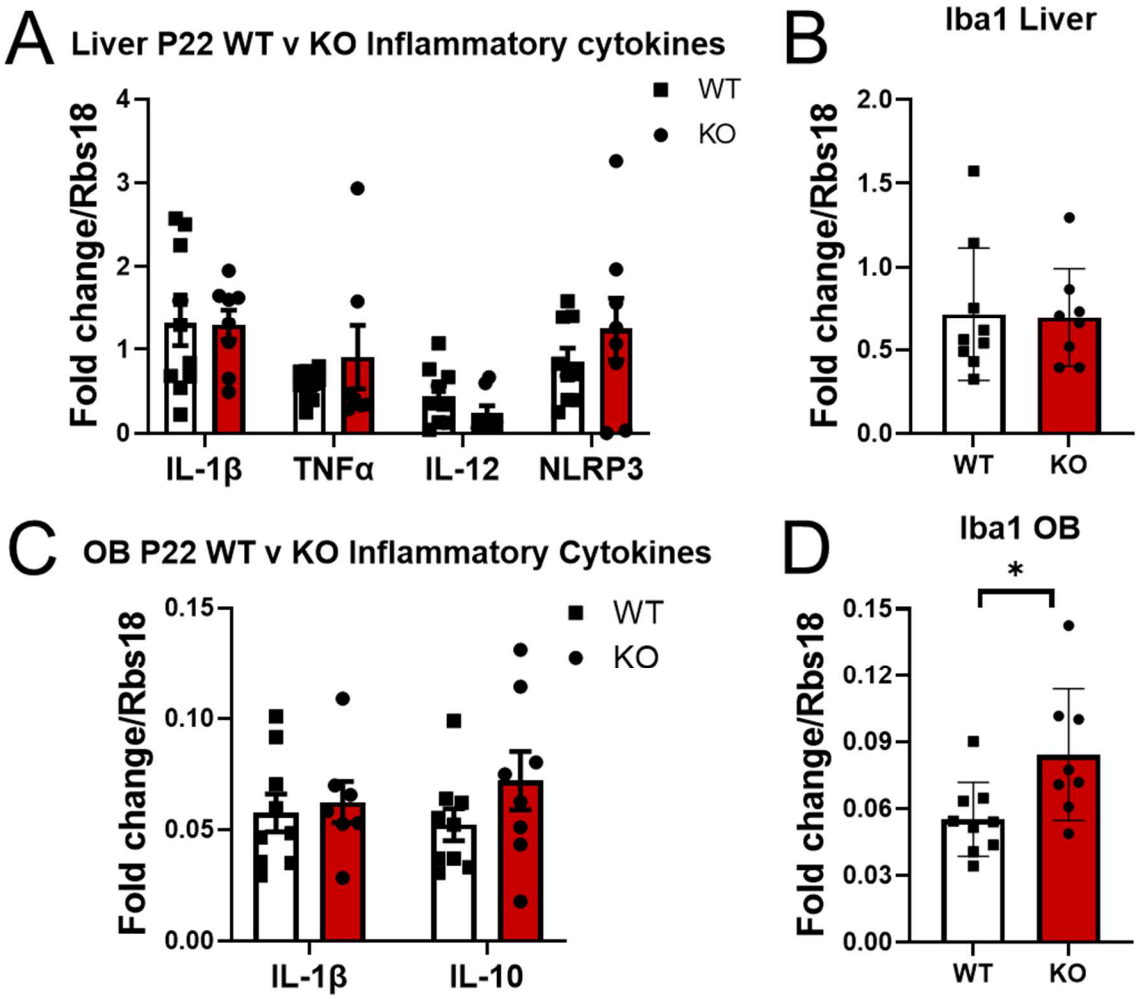

Figure 2.7 Inflammatory Factors Are Not Increased in the P21-22 NDUFS4 Knockout Liver or OB. A-D: Gene expression in the liver (**A-B**) and OB (**C-D**) of P22 WT and NDUFS4 KO mice were measured by qRT-PCR. **A-B**: No increases in *Iba1* or pro-inflammatory *Il1b*, *Tnfa*, *Il12*, or *Nlrp3* gene expression were detected in the NDUFS4 KO liver. **C-D**: Increased OB microglia (*Iba1*) but not pro-inflammatory *Il1b* or anti-inflammatory *Il10* gene expression were detected in the OB with the knockout of NDUFS4. Data are mean ± SE (*p < 0.05; unpaired t-test with Welch's correction) with n=8-10/group.

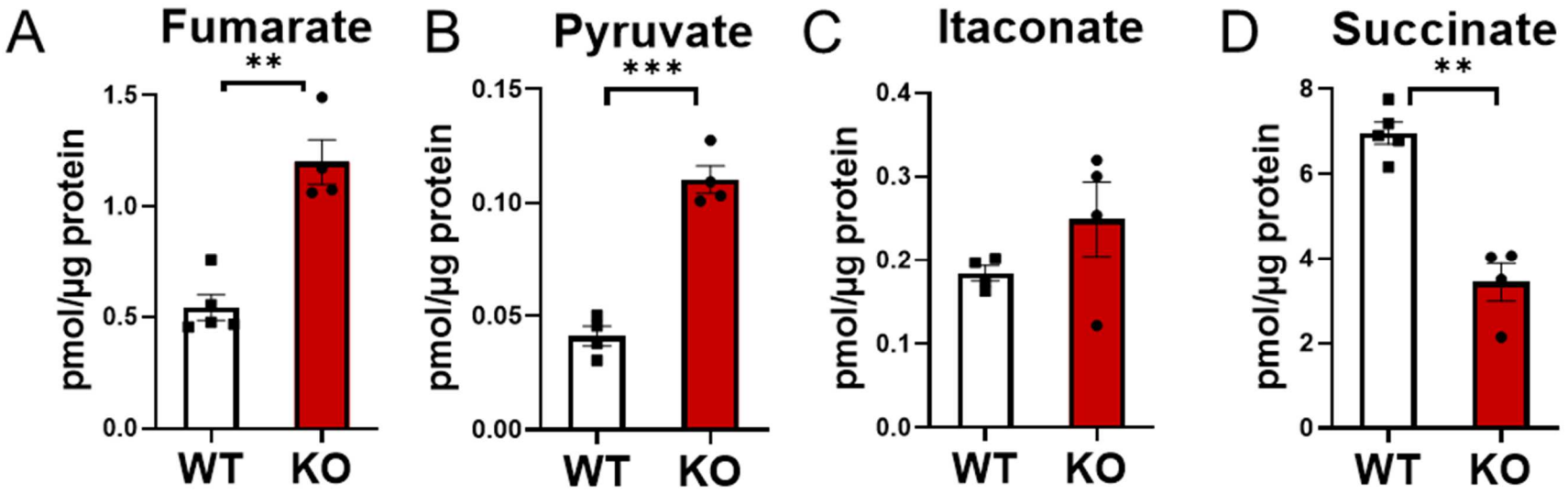

Figure 2.8 Quantification of Krebs cycle metabolites in the NDUFS4 Knockout Olfactory Bulb. P35-38 WT and NDUFS4 KO OBs were quantified by mass spectrometry. **A-D**: NDUFS4 KO OBs show ≥2-fold increase in fumarate and pyruvate, no increase in itaconate, and a 0.5-fold decrease in succinate compared to WT controls. Data are mean ± SE (**p < 0.01; ***p < 0.001; unpaired t-test with Welch's correction) with n=4-5/group.

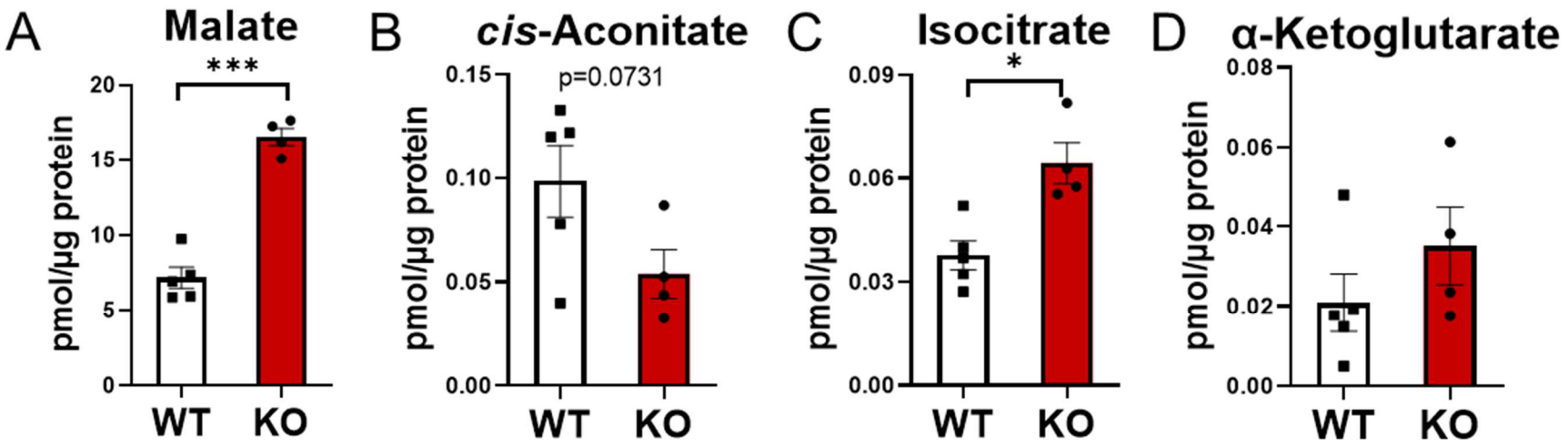

Figure 2.9 Quantification of Krebs cycle metabolites in the NDUFS4 Knockout Olfactory Bulb. P35-38 WT and NDUFS4 KO OBs were quantified by mass spectrometry. **A-D**: NDUFS4 KO OBs shows increased isocitrate and malate with no change in *cis*-aconitate or α-ketoglutarate compared to WT controls. Data are mean ± SE (*p < 0.05; ***p < 0.001; unpaired t-test with Welch's correction) with n=4-5/group.

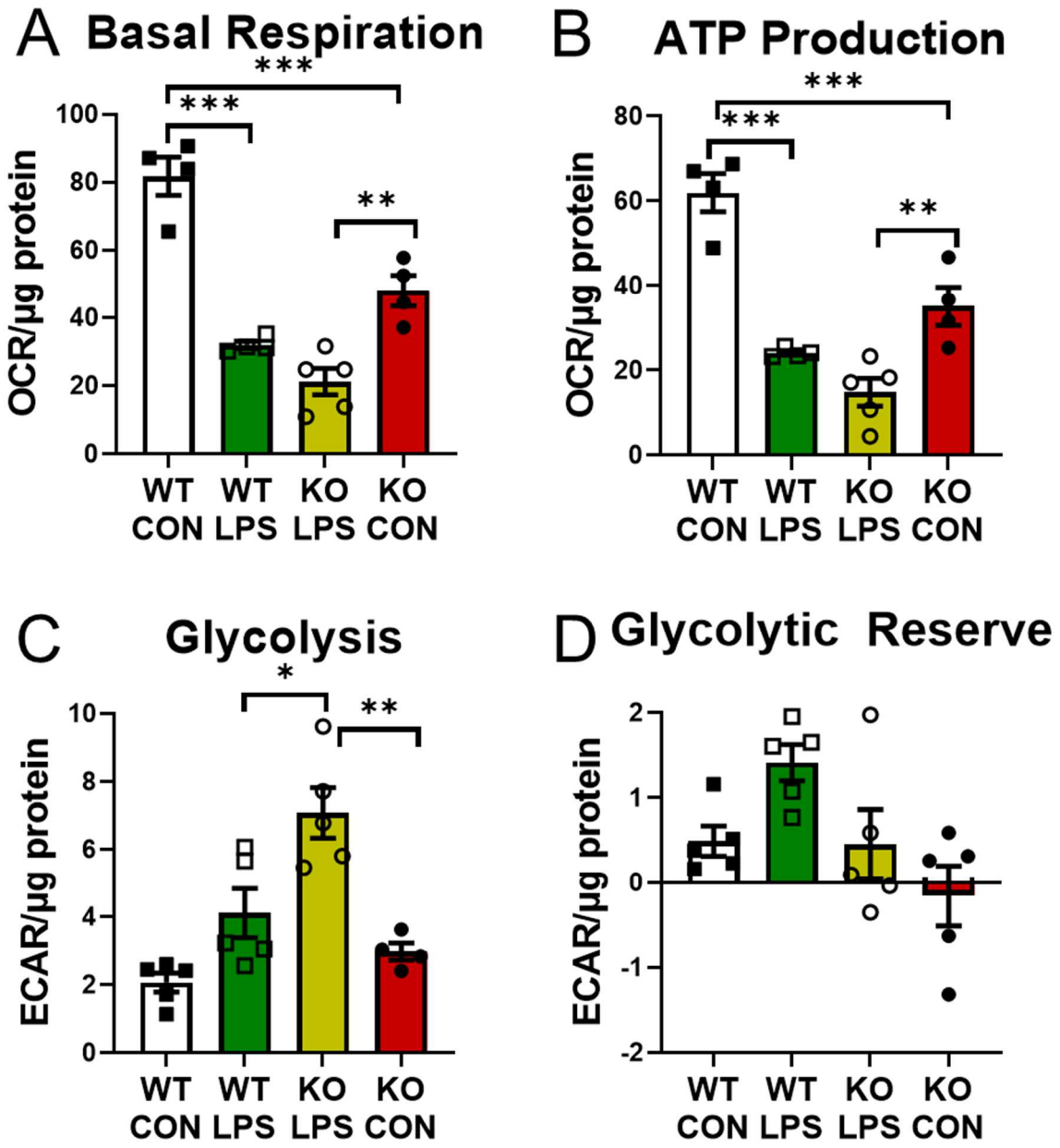

Figure 2.10 Knockout of NDUFS4 Promotes Altered Metabolic Flexibility in Response to Immune Stimulation. The respiratory profile of WT and KO P42 mouse primary macrophages stimulated for 1 h ±100 ng/mL LPS was analyzed on a Seahorse XF24 extracellular flux analyzer. **A-B**: WT and NDUFS4 KO macrophages have a 4-fold reduction in basal respiration (**A**) and ATP production (**B**) under LPS stimulation, and NDUFS4 KO macrophages have a 1.5-fold reduction in mitochondrial oxygen consumption and ATP production compared to WT counterparts in a mitochondrial stress test. LPS-stimulation significantly reduced mitochondrial oxygen consumption and ATP production. **C-D**: Macrophages were treated with a glycolytic stress test. LPS-stimulated macrophages show a 2-fold increase in glycolytic metabolism (**C**), and WT

macrophages show a 4-fold increase in glycolytic reserve under LPS-stimulation (**D**). NDUFS4 KO macrophages have little to no glycolytic reserve under basal conditions and have a 3-fold reduction in glycolytic reserve under LPS-stimulation (**D**) compared to WT macrophages. Therefore, NDUFS4 KO macrophages can switch from mitochondrial to glycolytic activity in pro-inflammatory conditions but with an impaired metabolic capacity. Data are mean ± SE (*$p < 0.05$; **$p < 0.01$; ***$p < 0.001$; two-way ANOVA) with n=4-5/group.

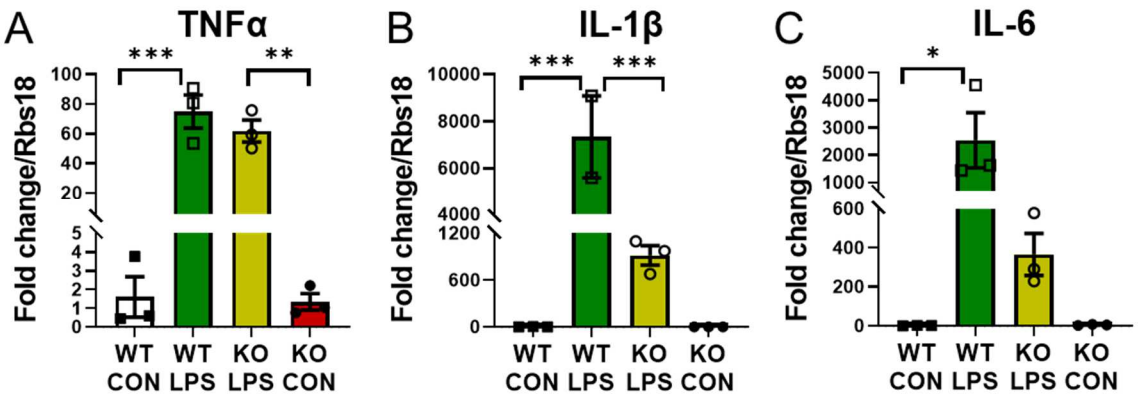

Figure 2.11 Knockout of NDUFS4 Impairs LPS-Induced Increases in Pro-Inflammatory Gene Expression. **A-C**: Gene expression in P42 WT and NDUFS4 KO macrophages stimulated for 18 h ±100 ng/mL LPS was measured by qRT-PCR. LPS-stimulated WT macrophages significantly increase the expression of *Tnfa*, *Il1b*, and *Il6*, while LPS-stimulated NDUFS4 KO macrophages only significantly increase the levels of *Tnfa*. Pro-inflammatory *Tnfa* trends toward a reduction to LPS-induced increases, and *Ill1b* and *Il6* show a 10-fold reduction to LPS-induced increases with knockout of NDUFS4. Data are mean ± SE (*p < 0.05; **p < 0.01; ***p < 0.001; two-way ANOVA) with n=2-3.

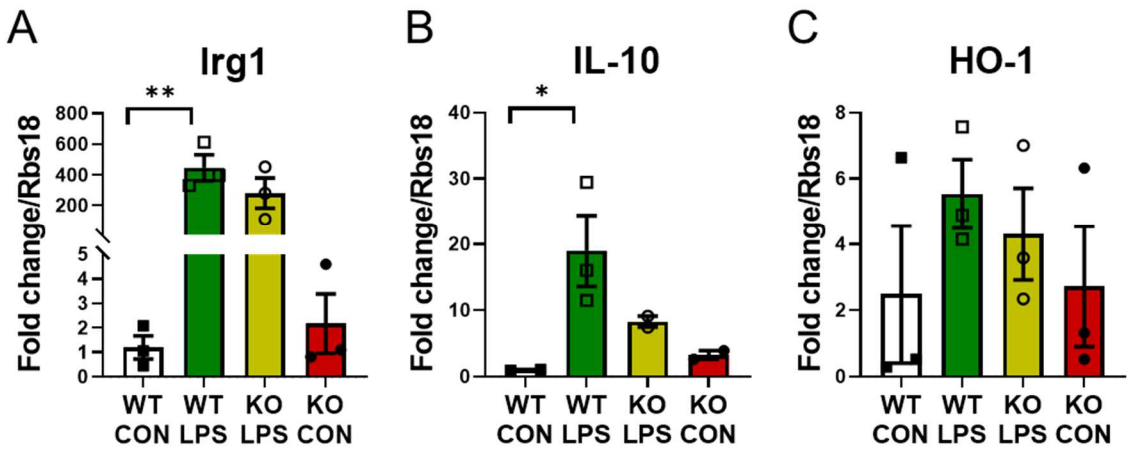

Figure 2.12 Knockout of NDUFS4 Impairs LPS-Induced Increases in Anti-Inflammatory Gene Expression. **A-C**: Gene expression in P42 WT and NDUFS4 KO macrophages stimulated for 18 h ±100 ng/mL LPS was measured by qRT-PCR. LPS-stimulated WT macrophages significantly increase the expression of *Il10* and *Irg1*. Anti-inflammatory *Irg1* shows a 3-fold reduction, *Hmox1* trends toward a reduction, and *Il10* shows an 8-fold reduction to LPS-stimulated increases in gene expression with knockout of NDUFS4. Data are mean ± SE (*$p < 0.05$; **$p < 0.01$; two-way ANOVA) with n=2-3.

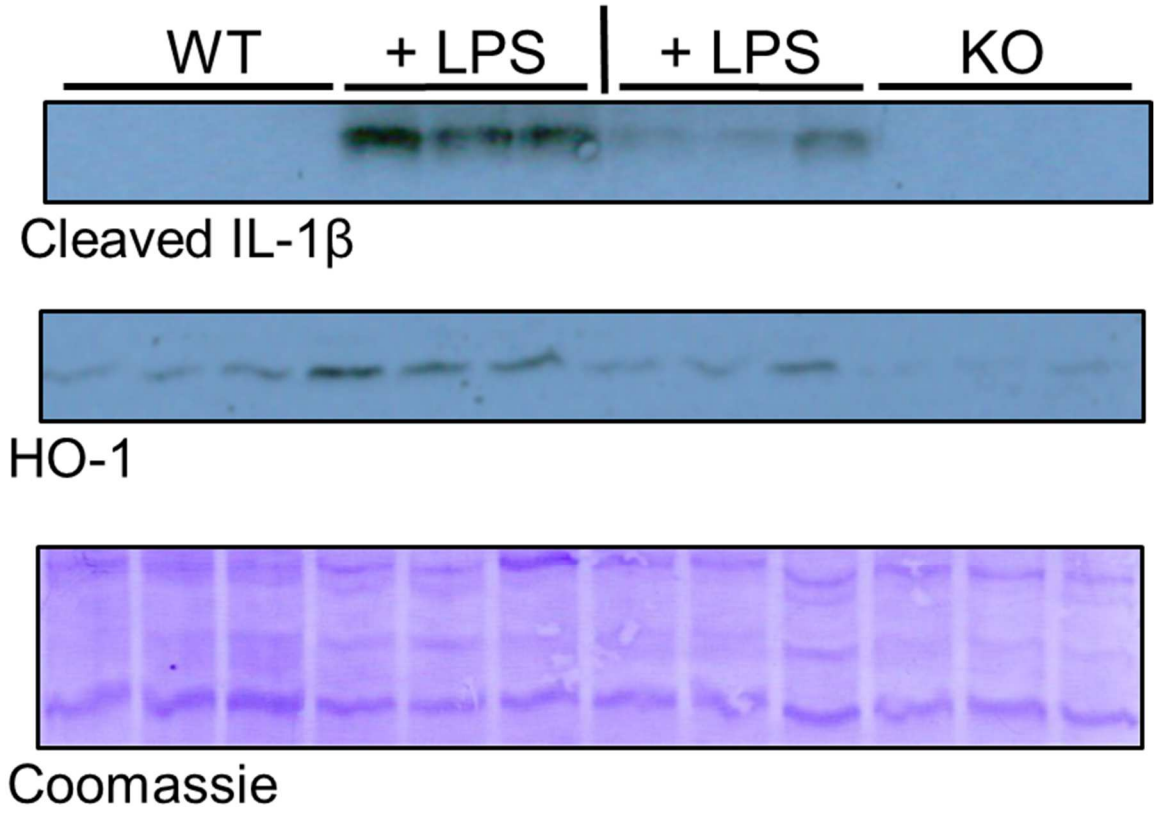

Figure 2.13 Knockout of NDUFS4 Impairs LPS-Induced Increases in Inflammatory Protein Production. Protein lysates (20 µg protein) from P42 WT and NDUFS4 KO mouse primary macrophages stimulated for 18 h ±100 ng/mL LPS were separated by SDS-PAGE followed by immunoblotting. IL-1β and HO-1 immunodetection show pronounced reductions in LPS-induced increases with knockout of NDUFS4. Coomassie staining was used as a loading control.

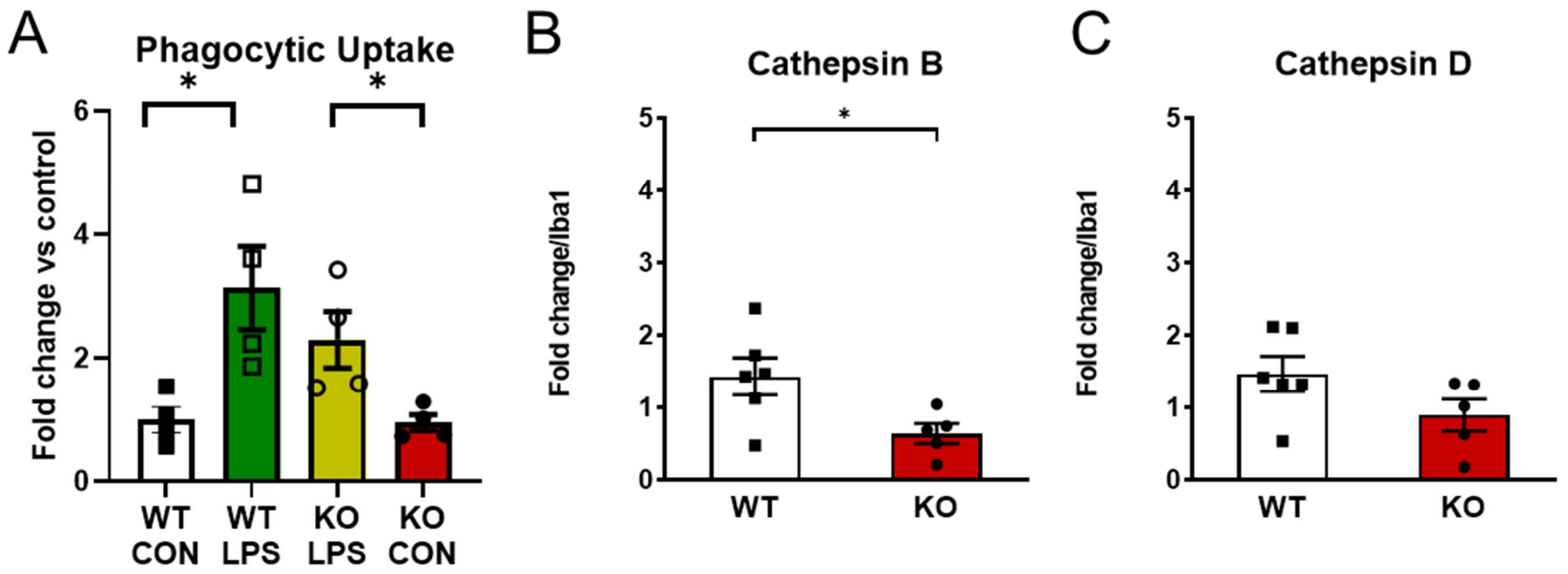

Figure 2.14 Lipopolysaccharide-stimulated Increases in Phagocytic Activity Are Impaired with Knockout of NDUFS4. A. The uptake of fluorescently labeled latex beads after 3 h for P42 WT and KO mouse primary macrophages stimulated for 18 h ±100 ng/mL LPS was measured by immunofluorescence imaging. NDUFS4 KO macrophages show a 1.3-fold reduction to LPS-stimulated increases in phagocytic uptake. Data are mean ± SE (*$p < 0.05$; two-way ANOVA) with n=4/group. **B-C**: Gene expression from P35-38 WT and NDUFS4 KO OBs was measured by qRT-PCR. Decreased *Ctsb* but not *Ctsd* gene expression was confirmed with knockout of NDUFS4. Data are mean ± SE (*$p < 0.05$; unpaired t-test with Welch's correction) with n=5-6/group.

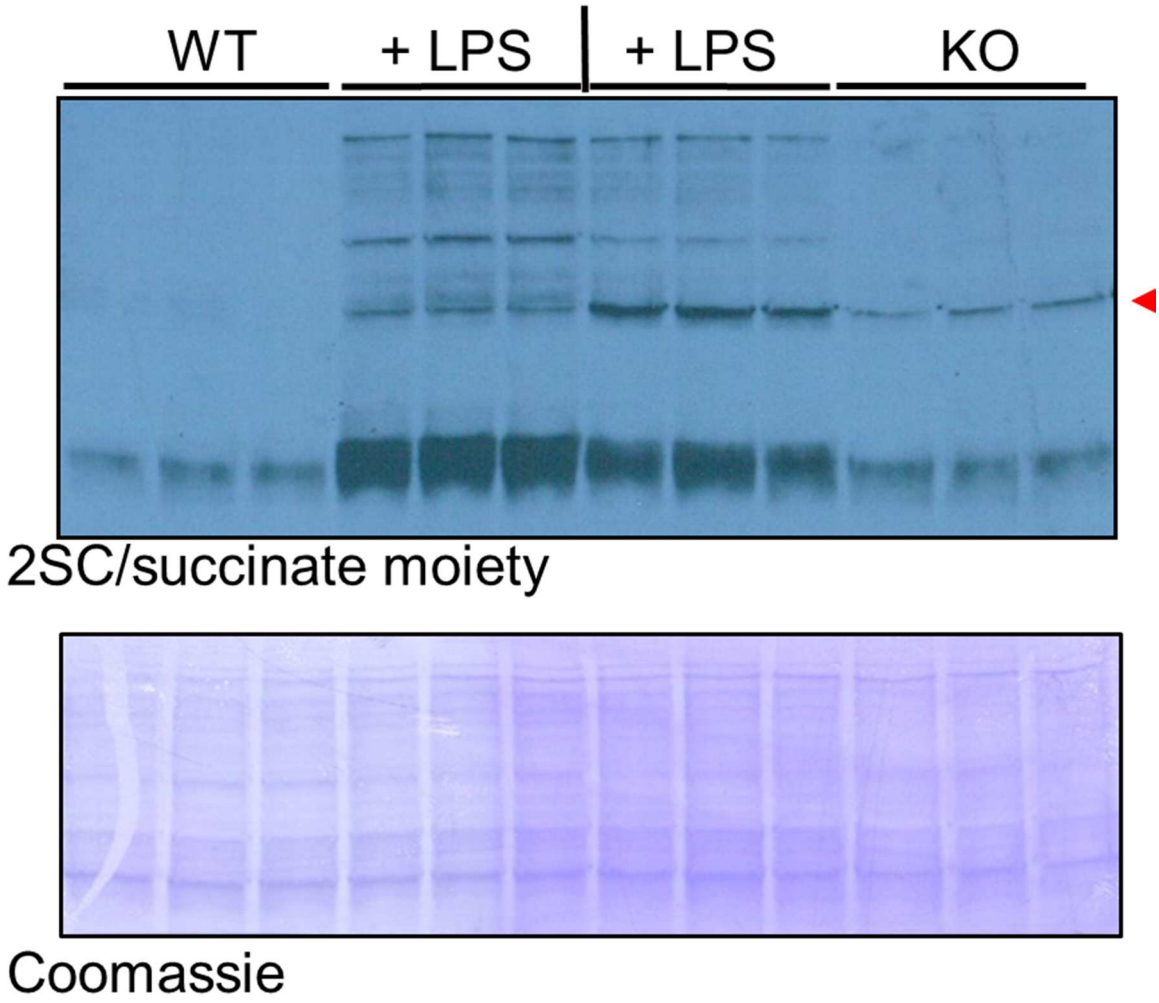

Figure 2.15 Lipopolysaccharide-stimulated Increases in Metabolite-Induced Protein Modifications Are Impaired Upon Knockout of NDUFS4. Protein lysates from P42 WT and KO mouse primary macrophages (20 µg protein) stimulated for 24 h ±5 µg/mL LPS were separated by SDS-PAGE followed by immunoblotting. 2SC/succinate moiety immunodetection was increased in response to LPS (2SC panel) in both WT and KO macrophages. However, NDUFS4 KO LPS-stimulated increases in succinate moieties are impaired compared to LPS-stimulated WT except for a band at ~50 kDa that was detected only in the KO macrophages prior to LPS stimulation.

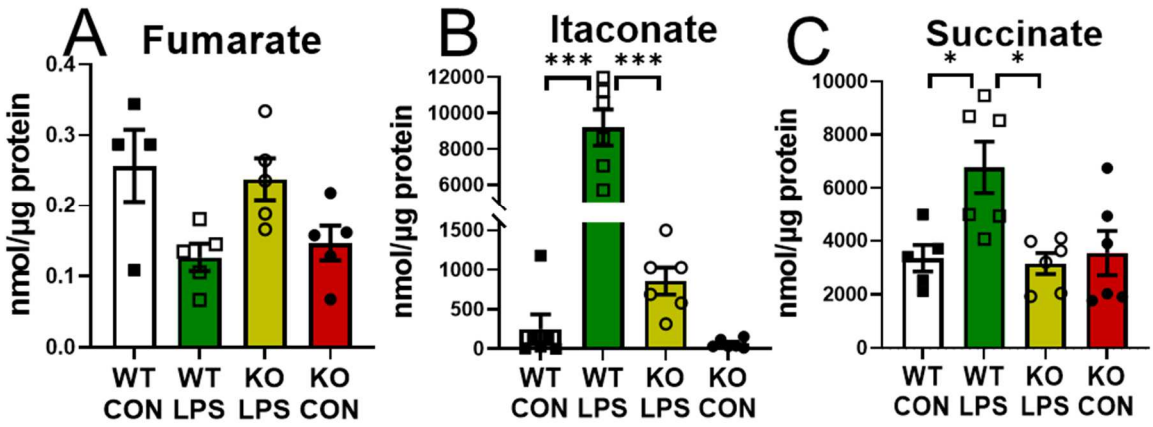

Figure 2.16 Knockout of NDUFS4 Impairs LPS-Stimulated Inflammatory Metabolite Accumulation. A-C: WT and NDUFS4 KO P42 mouse primary macrophages stimulated for 18 h ±100 ng/mL LPS were quantified by mass spectrometry. Itaconate and succinate but not fumarate increase due to LPS stimulation in WT macrophages, suggesting that the increase in succinate moieties due to LPS stimulation is not due to fumarate-induced protein succination. Only a 10-fold increase in itaconate and no increase in succinate were measured in LPS-stimulated NDUFS4 KO macrophages compared to a 40-fold and 2-fold increase, respectively, in LPS-stimulated WT macrophages. Data are mean ± SE (*$p < 0.05$; ***$p < 0.001$; two-way ANOVA) with n=4-5/group.

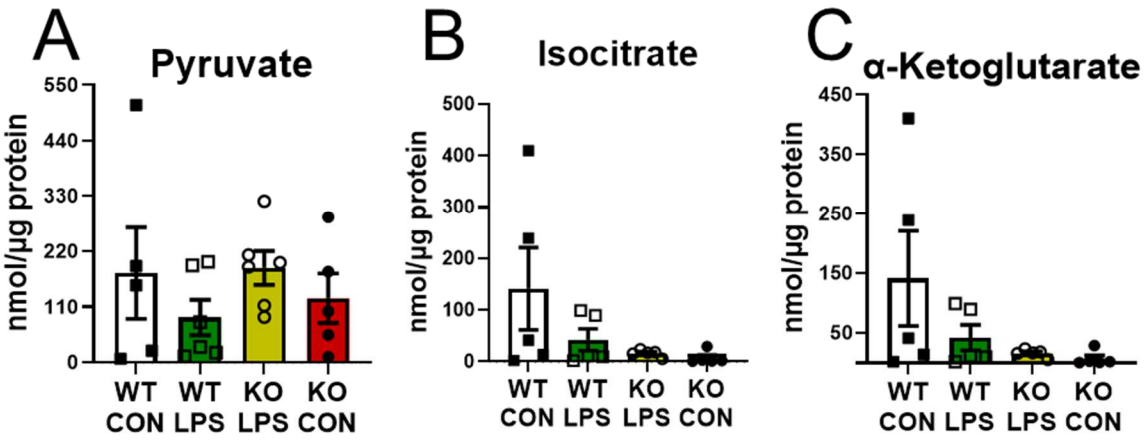

Figure 2.17 Knockout of NDUFS4 Does Not Alter Select Metabolite Levels. A-C: WT and NDUFS4 KO P42 mouse primary macrophages stimulated for 18 h ±100 ng/mL LPS were quantified by mass spectrometry. Pyruvate, isocitrate, and α-ketoglutarate are not changed due to LPS stimulation or the knockout of NDUFS4 in mouse macrophages. Data are mean ± SE (two-way ANOVA) with n=4-5/group.

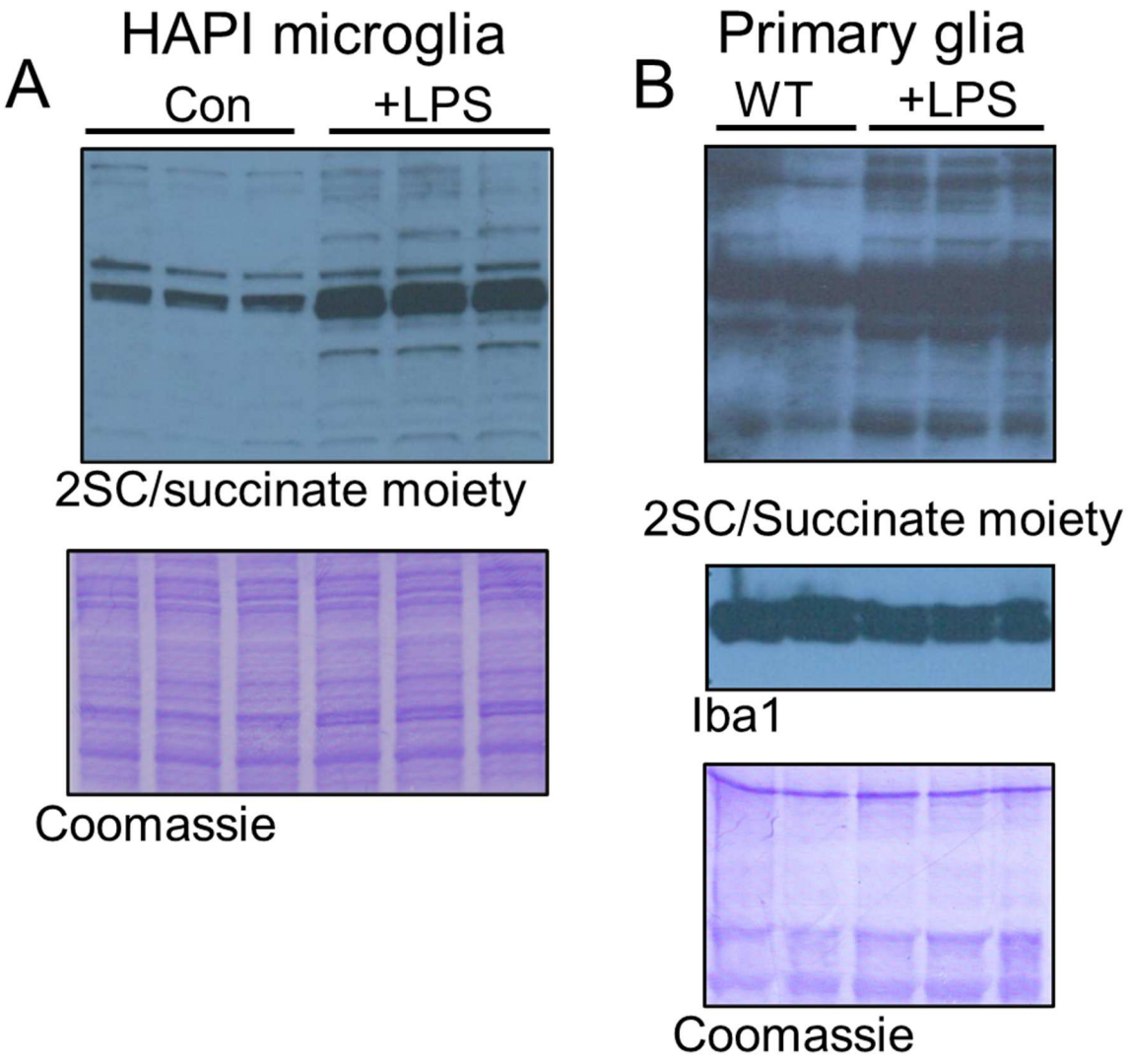

Figure 2.18 Lipopolysaccharide Stimulates Increased Metabolite-Induced Protein Modifications in Microglia. A: Protein lysates (20 µg protein) from HAPI cells stimulated for 18 h ±100 ng/mL LPS were separated by SDS-PAGE followed by immunoblotting and showed increased reactivity with the anti-2SC antibody that recognizes the succinate moieties following LPS treatment. Coomassie staining was used as a loading control. **B**: Protein lysates (20 µg protein) from isolated WT P42 mouse primary microglia stimulated for 24 h ±5 µg/mL LPS were separated by SDS-PAGE followed by immunoblotting and showed increased succinate moieties with LPS treatment.

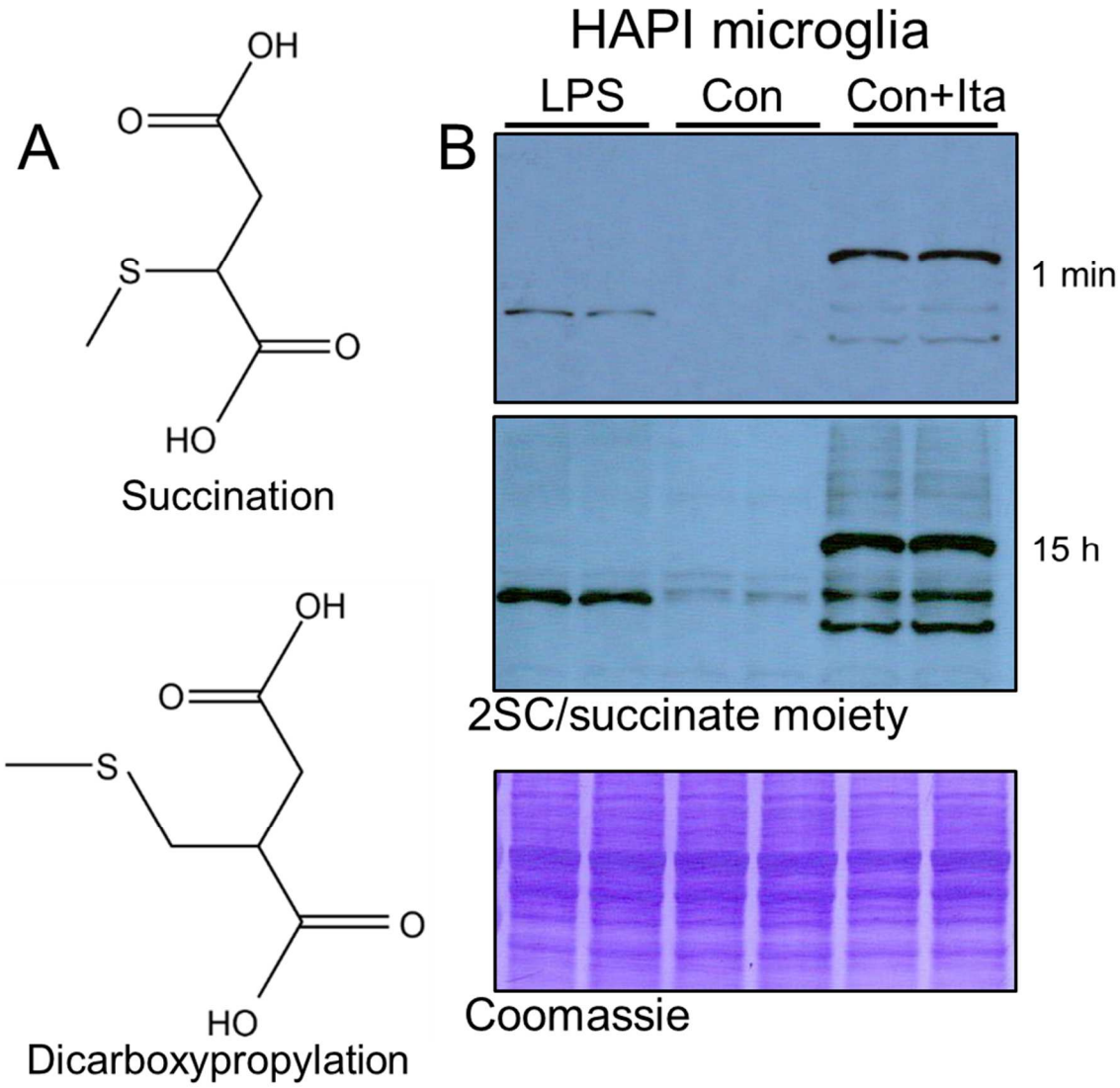

Figure 2.19 Anti-2SC Antibody Detects Itaconate-Induced Dicarboxypropylation **A**: Diagram of protein succination and dicarboxypropylation. Given the structural similarities between protein succination and dicarboxypropylation, we sought to determine whether the LPS-stimulated increase in succinate moieties detected by our 2SC antibody is due to protein dicarboxypropylation. **B**: Protein lysates (20 µg protein) of HAPI cells incubated for 24 h ±10 mM itaconate and positive controls stimulated for 18 h with 100 ng/mL LPS were separated by SDS-PAGE followed by immunoblotting. LPS treatment and incubation with itaconate show increased metabolite-induced protein modification. Coomassie staining was used as a loading control.

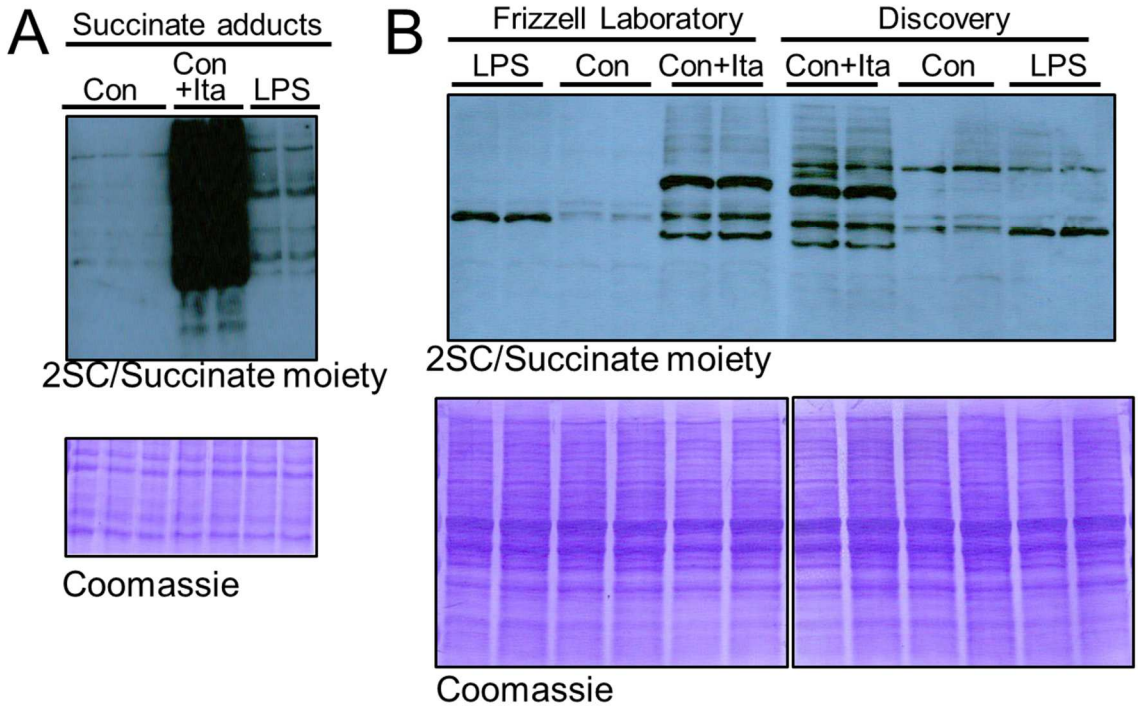

Figure 2.20 Immunodetection of Protein Dicarboxypropylation. A: Protein lysates (20 µg protein) from HAPI cells incubated ±10 mM itaconate for 24 h along with positive controls stimulated for 18 h with 100 ng/mL LPS were separated by SDS-PAGE followed by immunoblotting. LPS treatment and incubation with itaconate had increased metabolite-induced protein modification. Coomassie staining was used as a loading control. **B**: Protein lysates (20 µg protein) from HAPI cells incubated ±10 mM itaconate for 24 h along with positive controls stimulated for 18 h with 100 ng/mL LPS were separated by SDS-PAGE followed by immunoblotting. LPS treatment and incubation with itaconate increased metabolite-induced protein modification with our 2SC antibody and the Discovery 2SC antibody (crb2005017).

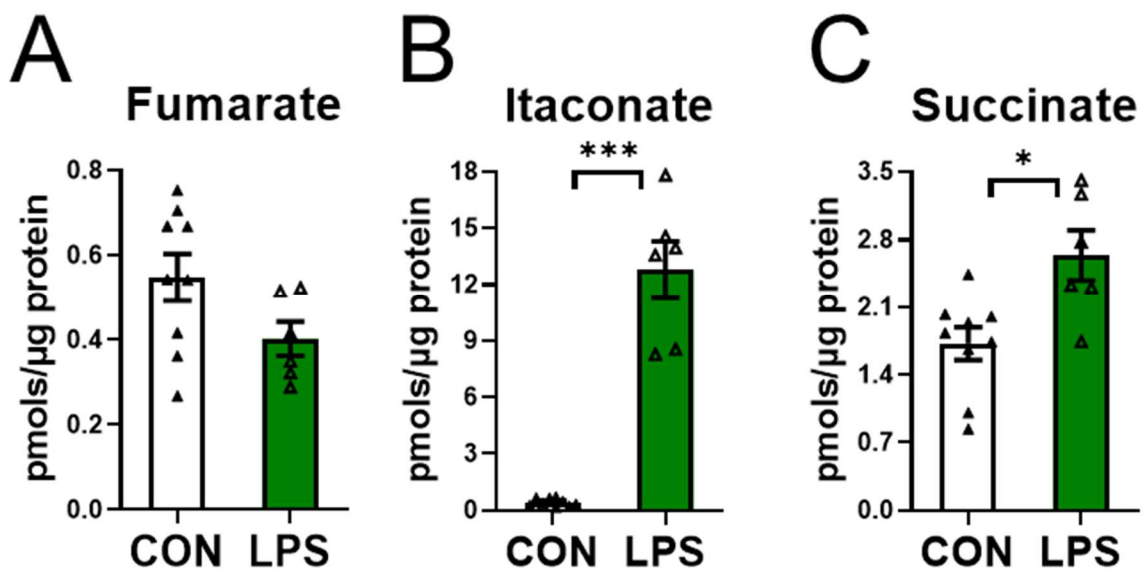

Figure 2.21 Itaconate is Significantly Increased in LPS-Stimulated HAPI Cells. A-C: HAPI microglial cells stimulated for 24 h ±5 µg/mL LPS were quantified by mass spectrometry. Itaconate and succinate but not fumarate increase due to LPS stimulation. Therefore, the changes in macrophage and microglia succinate moieties detected by our 2SC antibody are due to changes in itaconate-induced protein dicarboxypropylation. Data are mean ± SE (*$p < 0.05$; ***$p < 0.001$; unpaired t-test with Welch's correction) with n=5-8/group.

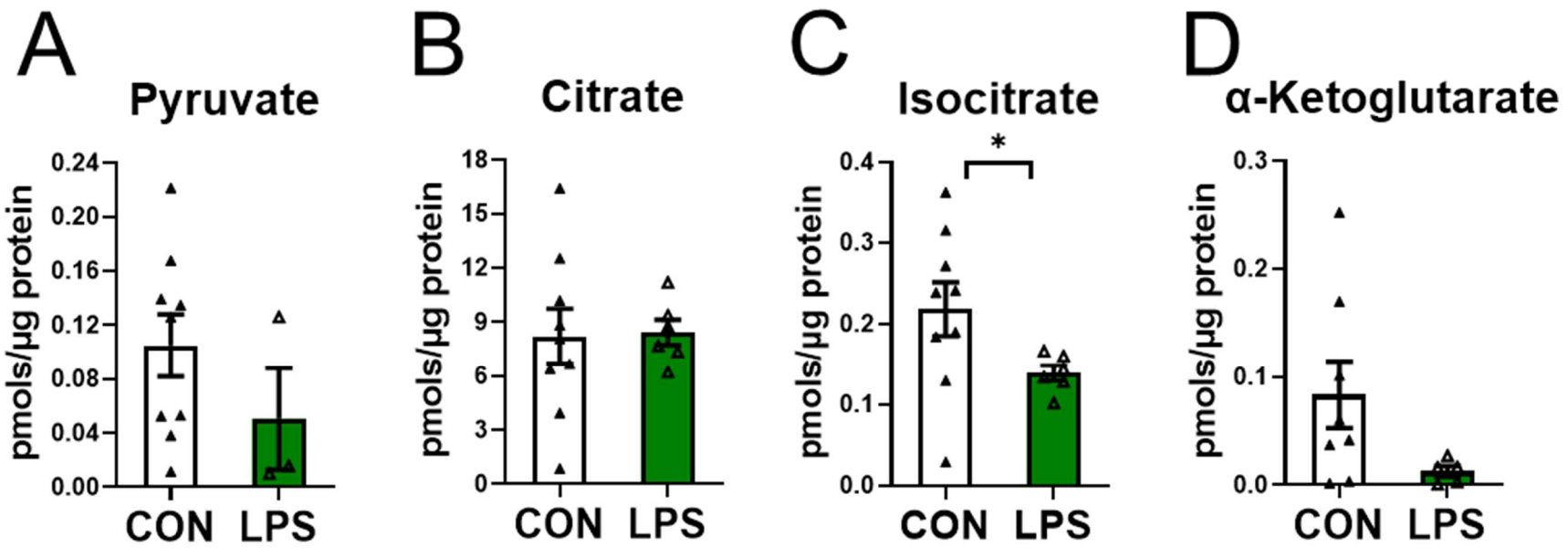

Figure 2.22 Select Metabolites Are Not Increased by LPS Stimulation in HAPI Cells. A-D: HAPI microglial cells stimulated for 24 h ±5 µg/mL LPS were quantified by mass spectrometry. Pyruvate, citrate, and α-ketoglutarate are unchanged, and isocitrate is significantly decreased due to LPS stimulation in HAPI microglia. Data are mean ± SE (*p < 0.05; unpaired t-test with Welch's correction) with n=3-8/group.

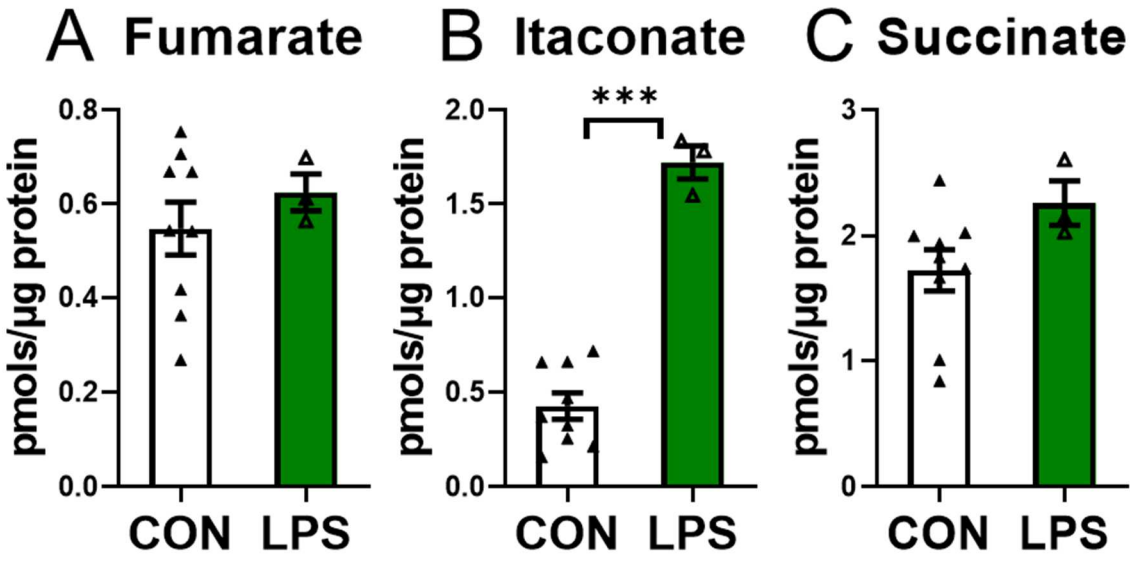

Figure 2.23 HAPI Cells Accumulate Itaconate. HAPI microglial cells stimulated for 3 h ±5 µg/mL LPS were quantified by mass spectrometry. **A-C**: Itaconate but not fumarate or succinate increases due to LPS stimulation. Therefore, the changes in macrophage and microglia succinate moieties detected by our 2SC antibody are due to consistent changes in itaconate-induced protein dicarboxypropylation. Data are mean ± SE (***p < 0.001; unpaired t-test with Welch's correction) with n=3-8/group.

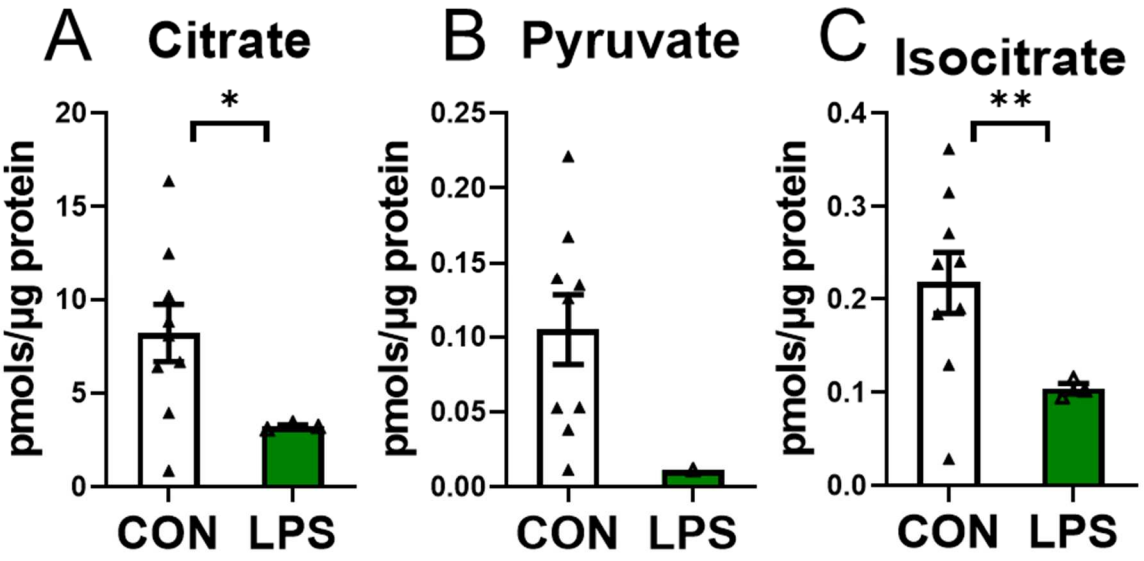

Figure 2.24 Select Metabolites Are Not Increased After LPS Stimulation. A-C: HAPI microglial cells stimulated for 3 h ±5 µg/mL LPS were quantified by mass spectrometry. Citrate and isocitrate were significantly decreased, and α-ketoglutarate was unchanged due to LPS stimulation in HAPI cells Data are mean ± SE (*p < 0.05; **p < 0.01; unpaired t-test with Welch's correction) with n=3-8/group.

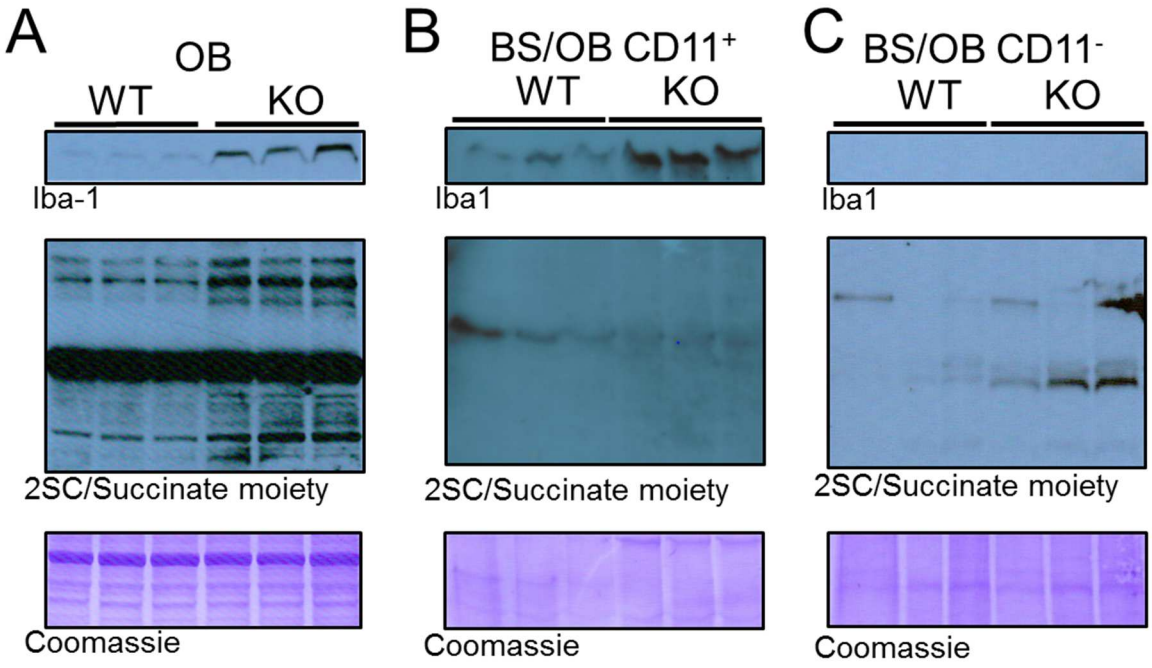

Figure 2.25 NDUFS4 Knockout Microglia *in vivo* Do Not Accumulate Metabolite-Induced Protein Modification. A: Protein lysates (20 µg protein) from the OB of P42 WT and NDUFS4 KO mice were separated by SDS-PAGE followed by immunoblotting and run with the Frizzell laboratory antibodies. Increased Iba1 and succinate moieties were detected with knockout of NDUFS4. Coomassie staining was used as a loading control. **B**: Protein lysates (20 µg protein) from $CD11^+$ P42 WT and NDUFS4 KO OB and BS were separated by SDS-PAGE followed by immunoblotting. The microglial ($CD11^+$) fraction confirms NDUFS4 KO BS and OB have increased Iba1 but no change in 2SC immunodetection, reflecting the limited generation of itaconate in the glia. Coomassie staining was used as a loading control. **C**: Protein lysates (20 µg protein) from non-microglial $CD11^-$P42 WT and NDUFS4 KO OB and BS were separated by SDS-PAGE followed by immunoblotting. 2SC immunodetection shows increased presence of a succinate moiety from the non-glial cell types ($CD11^-$) fraction with knockout of NDUFS4 due to fumarate-mediated succination of neurons (Piroli et al., 2016; Piroli et al., 2021). Iba1 was not detected in WT or NDUFS4 KO $CD11^-$ BS and OB, confirming separation of microglia. Coomassie staining was used as a loading control.

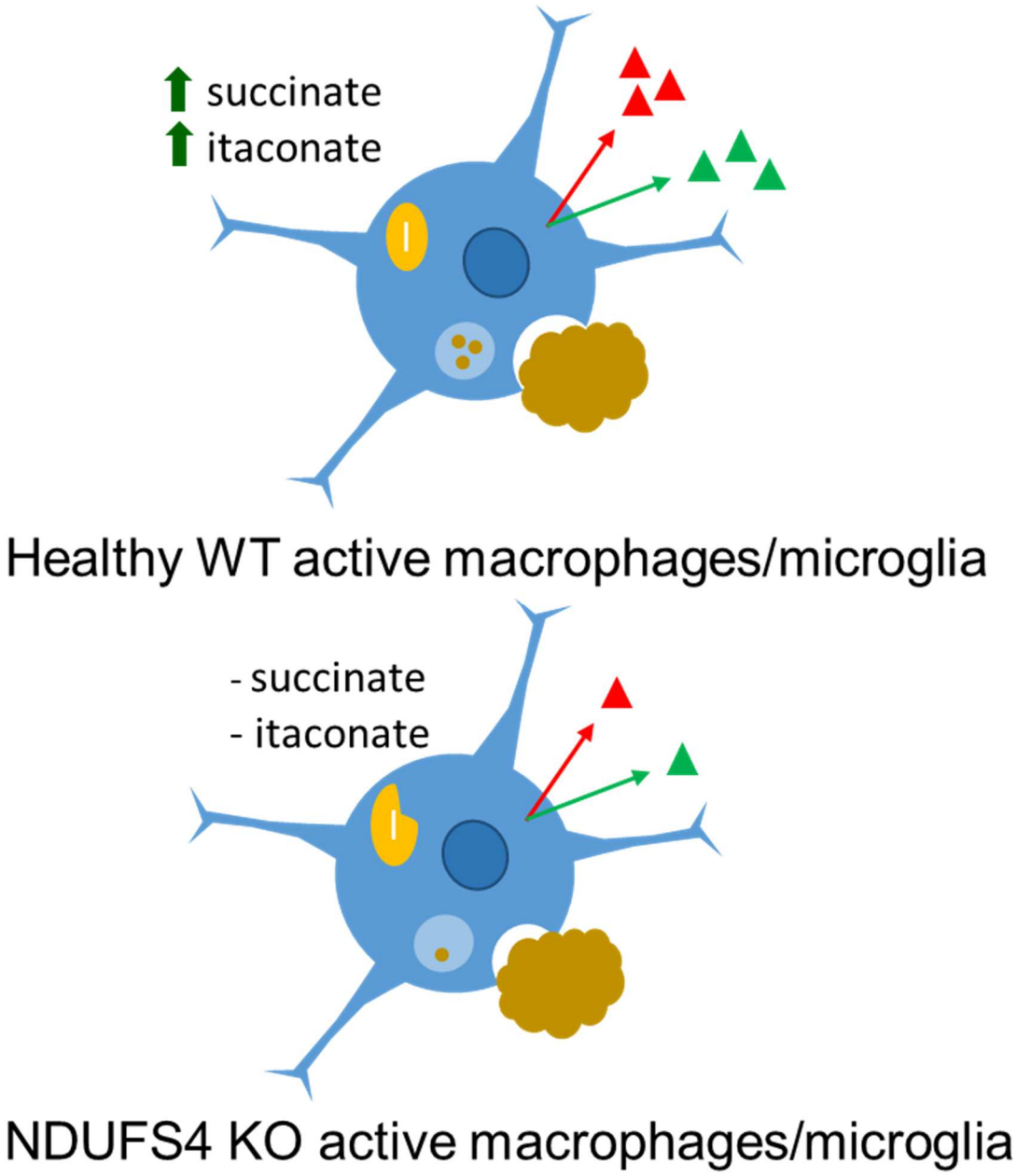

Figure 2.26 Impaired Immunometabolism in NDUFS4 Knockout Macrophages and Microglia. Knockout of NDUFS4 impairs increases in itaconate and succinate during pro-inflammatory activation. The reduction in itaconate and succinate accumulation impairs the ability of the microglia to produce inflammatory factors or phagocytize debris within the necrotizing lesion environment. These impairments prevent the resolution of inflammation, prolonging a positive feedback loop between chronic microgliosis and necrotizing neurons.

CHAPTER 3

ASSESSMENT OF THE POTENTIAL OF 4-OCTYL ITACONATE IN AMELIORATING MOTOR DEFICITS IN NDUFS4 KNOCKOUT MICE

McCain, R.S.[1], Piroli, G.G.[1], Martin, S.L.[1], Smith, H.H.[1], Shtutman, M.[2], and Frizzell, N.[1]

1) Department of Pharmacology, Physiology & Neuroscience, School of Medicine, University of South Carolina, Columbia, SC 29209, USA
2) Department of Drug Discovery & Biomedical Sciences (DDBS), College of Pharmacy, University of South Carolina, Columbia, SC 29209, USA

To be submitted

3.1 Introduction

Current strategies for the treatment of mitochondrial diseases incorporate electron carriers and antioxidants, including vitamins and quinone analogs, but these only slow the progression of conditions such as Leigh syndrome (Hargreaves, 2014**;** Turunen et al., 2004; Garcia-Cazorla et al., 2008; Parikh et al., 2015). Both Leigh syndrome patients and NDUFS4 KO mice have unresolved microgliosis in pathologically relevant brain regions with increased disease severity (Quintana et al., 2010; Leigh, 1951; van Erven et al., 1987). Glia-specific knockdown of a Complex I homolog in *Drosophilia* was sufficient to cause neurotoxicity (Hegde et al., 2014), indicating that loss of sufficient mitochondrial function in glia may contribute to the neuronal decline. We have demonstrated impairments in inflammatory metabolite accumulation, reduced activation of inflammatory signaling, and lower phagocytic activity in NDUFS4 KO macrophages and the OB (Chapter 2). Therefore, strategies that augment microglial function may offer benefit to prevent or limit neuropathology for Leigh syndrome patients.

Microglia are the resident immune system of the brain and regulate the inflammatory state of the brain through the release of pro and anti-inflammatory cytokines (Amici et al., 2017; Lampropoulou et al., 2016; Cordes et al., 2016; Tannahill et al., 2013). Recent studies have outlined several sex-specific differences in microglial function. Microglia in males are more developmentally delayed by maternal stress and less able to resolve cerebral ischemia. In addition, microglia in males have less phagocytic activity and a stronger association with

select pro-inflammatory gene expression, especially NF-κβ. These sex-specific differences persist *in vitro* and *in vivo*, across-sex transplantation, and are not solely due to the anti-inflammatory activity of estrogens in females (Nelson et al., 2017; Bilbo et al., 2018; Villa et al., 2018).

As the NDUFS4 KO glia have diminished production of itaconate in the lesions where they accumulate, and in response to LPS-stimulation in macrophages, we sought to augment microglial function through the administration of exogenous itaconate. Exogenous itaconate application to macrophages enhanced their phagocytic capacity and ability to clear *E. coli* infection. It also reduced neuronal tissue damage after spinal cord injury (O'Callaghan et al., 2021; Cordes et al., 2020; Fan et al., 2020; Bajwa et al., 2019**;** Yun et al., 2021). 4-Octyl itaconate (4OI) is a cell-permeable derivative of the immunometabolite itaconate (**Figure 3.1**) and is capable of cysteine dicarboxypropylation to irreversibly modify proteins. 4OI modifies KEAP1, stabilizing NRF2 and promoting anti-inflammatory gene expression, including *Hmox1* (Mills et al., 2018; Swain et al., 2020). As a result, 50 mg/kg 4OI inhibits pro-inflammatory IL-1β, lactate, and IL-6 production *in vivo*, and 4OI inhibits GAPDH and lactate dehydrogenase activity in macrophages (Muri et al., 2020; Liao et al., 2019; Mills et al., 2018; Swain et al., 2020). 450 mg/kg total exogenous itaconate over 30 min reduced reactive oxygen species, increased glutathione levels, and improved survival rates by 4-fold in a mouse model of ischemic-reperfusion injury (Cordes et al., 2020). 400 mg/kg of dimethyl itaconate, alternative itaconate ester, alleviated blood-brain-barrier disruption and suppressed microglial activation in a mouse model of experimental

autoimmune encephalomyelitis (Kuo et al., 2020). In addition, dimethyl itaconate treatment inhibited LPS-stimulated increases in IκBζ and prevented the development of pathology in the imiquimod stimulated mouse model of psoriasis (Bambouskova et al., 2018)

Given that itaconate esters have shown benefit in the above conditions, we hypothesized that 4OI would benefit the NDUFS4 KO microglia, perhaps by improving their function and preventing their accumulation in lesions. Improved microglial activity may preserve neuronal health and offer benefits to prevent motor deficits. We administered 4OI to the mice ~P25 after assessment of their motor behavior prior to treatment. Motor behaviors were assessed prior to the termination of 4OI administration to determine if exogenous itaconate offered benefit. We started with 50 mg/kg as it effectively reduced LPS-stimulated increases in serum pro-inflammatory factors (IL-1β, TNFα, IL-6) in prior studies and increased the dosage to 100 mg/kg as it decreased ROS and inflammatory cytokines in LPS-induced lung injury (Mills et al., 2018; Liao et al., 2019; Li et al., 2020).

3.2 Results

Prior to using 4-octyl itaconate in mice, we first confirmed the specificity of 4OI immunoregulatory action using HAPI microglia (Cheepsunthorn et al., 2001). The microglia were pretreated ±62.5 μM 4OI for 2 h prior to stimulation with ±100 ng/mL LPS for 18 h. The expression levels of genes previously impacted by itaconate and itaconate derivatives (Mills et al., 2018; Sun et al., 2020; Singh et al., 2021) were assessed by qRT-PCR. As expected, LPS stimulation increased

the expression of *Irg1* and *Hmox1* in addition to *Nlrp3* and *Tnfa* (**Figure 3.2**). 4OI treatment attenuated LPS-stimulated increases in pro-inflammatory (*Nlrp3* and *Tnfa*) and *Irg1* gene expression (**Figure 3.2A-C**). 4OI treatment also promoted increased anti-inflammatory factor (*Hmox1*) gene expression in LPS-stimulated HAPI cells (**Figure 3.2D**), a known target of NRF2-mediated transcriptional activation by 4OI (Mills et al., 2018). Therefore, 4OI suppresses the pro-inflammatory phenotype in activated microglia exposed to LPS.

We have previously shown that NDUFS4 KO macrophages have diminished LPS-stimulated production of itaconate and reduced phagocytic uptake versus WT macrophages (**Figure 2.14, 2.16**). As itaconate drives macrophage polarization towards an anti-inflammatory profile, we sought to determine if 4OI treatment would benefit NDUFS4 KO mice and prevent microglial accumulation. Several studies with varied doses and duration of 4OI treatment were performed after the mice were assigned to their treatment groups (**Figure 3.3**). The studies were designed to begin treatments as early as possible after baseline behavior measurements following genotyping. This allowed early intervention with itaconate treatment to determine if microglial accumulation could be limited or resolved. P22 mice (1 d post-weaning and genotyping) were habituated on the rotarod and inclined balance beam prior to baseline testing of their motor performance. 50 mg/kg of 4OI was administered once every 3 days over the course of 16 days prior to post-treatment motor behavior testing and tissue collection (**Figure 3.3A**). Body weight analysis demonstrated that the NDUFS4 KO mice showed an expected decrease in body weight at P26 (**Figure 3.4A**). 4OI treatment did not alter the body

weight of WT or NDUFS4 KO mice. The motor endurance of the mice on the rotarod was assessed using the total time spent walking (see Methods). NDUFS4 KO mice had a 50% decrease in endurance on the rotarod in the post-treatment test, which is expected for NDUFS4 KO mice starting at ~P35 (Kruse et al., 2008; Quintana et al., 2010). However, 4OI treatment had no significant effect on this motor behavior (**Figure 3.4B**). Assessment of fine motor control on the balance beam was calculated as the time taken to cross the 1 m x 7 mm beam with a 4^{o} incline, as well as the number of paw slips observed as they crossed. NDUFS4 KO mice showed a significant increase in the time to cross and an increase in the number of paw slips compared to their WT counterparts. 4OI treatment had no significant effects on either of these parameters (**Figure 3.4C-D**).

Since 4OI was well-tolerated by the mice, we increased the dose to 100 mg/kg and administered more frequently, once every 2 d for 14 d prior to post-treatment motor behavior testing and tissue collection (**Figure 3.3B**). Body weight analysis demonstrated that the NDUFS4 KO mice showed an expected decrease in body weight at P23 and 4OI treatment does not significantly impact WT or NDUFS4 KO body weight (**Figure 3.5A**). Assessment of motor endurance confirmed behavioral impairments with knockout of NDUFS4 (**Figure 3.5B**), with an expected 50% decrease in time spent walking. Strikingly, 4OI significantly preserved NDUFS4 KO motor endurance capacity by ~94% exclusively in male mice. Specifically, the cyclodextrin vehicle-treated males showed a 53% decline in endurance, whereas 4OI-treated males showed only a 3% decline in endurance (**Figure 3.5C**). This outcome was not observed in female mice. The original study

was not designed to look for sex differences, but since the large group size (n=9-10) contained 5 males, we were able to detect these differences. Assessment of fine motor coordination confirmed NDUFS4 KO-induced impairments (**Figure 3.6**). In contrast to motor endurance, 4OI treatment did not significantly affect fine motor performance across the genotypes (**Figure 3.6**).

To determine if 4OI treatment altered microglial content in the OB tissue, we analyzed *Iba1* expression by qRT-PCR and protein production through immunoblotting. qRT-PCR confirmed that knockout of NDUFS4 had increased microglial (*Iba1*) gene expression (**Figure 3.7A**). Surprisingly, 4OI did not noticeably decrease the expression of *Iba1* and thus the chronic microgliosis. qRT-PCR was used to analyze whether 4OI promoted increased anti-inflammatory gene expression and decreased pro-inflammatory and *Irg1* gene expression as expected. Strikingly, 4OI treatment did not alter pro-inflammatory (*Tnfa*, *Il1b*, *Nlrp3*, and *Il6*), *Irg1*, or anti-inflammatory gene expression (*Hmox1* and *Il10*) in the NDUFS4 knockout OB vs. WT (**Figure 3.7B-D, 3.8**).

Given the positive effects of 4OI treatment on motor endurance, we considered that 4OI treatment may extend the lifespan of NDUFS4 KO mice if the treatment was prolonged. Administration of 100 mg/kg 4OI started at ~4 weeks (P28) and continued until ~P75. At that point, clinical assessment of the mouse phenotype found that both the vehicle-treated and 4OI-treated mice had significant motor impairments with no sign of clinical improvement. Therefore, compassionate euthanasia was performed on both vehicle and 4OI-treated NDUFS4 KO mice. Although lifespan was not extended, several additional parameters were assessed

to determine if 4OI improved other clinical outcomes. Body weight, surface body temperature, gait, and hindlimb curling were assessed in NDUFS4 KO vehicle and 4OI-treated mice. The NDUFS4 KO-induced decline in body weight was unchanged following 4OI treatment (**Figure 3.9A**). However, 4OI treatment tended to slow NDUFS4 KO-induced decline in body temperature as measured by a surface thermometer on the abdomen (**Figure 3.9B**). Right gait overlap, a measure of gait instability, had a 50% decrease with 4OI treatment vs. vehicle-treated KOs (**Figure 3.9C**) (de Haas et al., 2016). Finally, assessment of hindlimb curling provided a readout of the onset of motor dysfunction. Only 71% of 4OI-treated NDUFS4 KO mice had developed curling by P49 while 100% of vehicle-treated controls demonstrated this behavior when picked up by the tail (**Figure 3.9D**). While these parameters did not achieve statistical significance with this group size, they suggest that 4OI may improve several 'quality of life' clinical measures in the KO mice.

Since 4OI is a cell-permeable ester that can enter any cell type, we considered that it might also directly impact neuronal health, independent of effects on microglia. To measure the effects of 4OI treatment on neuronal health, protein lysates from the 14 d 4OI-treated (100 mg/kg) NDUFS4 KO mouse cerebellum were separated by SDS-PAGE followed by immunoblotting. 4OI treatment increased the levels of PSD95, a marker of neuronal synapses, in the NDUFS4 KO cerebellum (**Figure 3.10**) (Coley and Gao, 2018). While further exploration is needed to clarify the sex-specific effects and mechanism of action for 4-octyl itaconate, this metabolite is a promising adjunct treatment for NDUFS4 KO mice.

3.3 Discussion

We explored the utility of 4-octyl itaconate as a treatment for Leigh syndrome modeled in the NDUFS4 KO mouse. Preliminary testing using a rat microglial cell line confirmed the ability of 4OI to inhibit pro-inflammatory (*Nlrp3* and *Tnfa*) and *Irg1* gene expression and promote an anti-inflammatory phenotype (*Hmox1*) during LPS stimulation, confirming the original observations by Mills et al. (Mills et al., 2018).

While 4OI (50 mg/kg) treatment over 16 days failed to improve motor function in NDUFS4 KO mice, the 4OI (100 mg/kg) treatment over a 14-day period did significantly slow NDUFS4 KO-induced decline in motor endurance by ~94% in males. Classical Leigh Syndrome in humans typically affects males and females in equal numbers, with similar disease progression. In addition, male and female NDUFS4 KO mice have similar disease progression (Kruse et al., 2008; Bolea et al., 2019). In this study, we found that 4OI offered significantly more protection to males than females, although the reasons for this remain unclear. Several sex-specific distinctions of microglia in the brains of mice may underlie the specific increase in the efficacy of 4OI we observed for NDUFS4 KO males. As male microglia have less phagocytic activity and a stronger association with pro-inflammatory NF-κβ gene expression, the anti-inflammatory effects of 4OI may be more effective at alleviating chronic microgliosis in males by inhibiting NF-κβ levels (Liao et al., 2019; Nelson et al., 2017; Bilbo et al., 2018; Villa et al., 2018).

However, examination of microglial content, determined by *Iba1* expression in the olfactory bulb, did not show any differences after 4OI treatment in males (**Figure 3.7A**), suggesting this benefit was independent of total microglia content. However, the activity of the microglia may have been beneficially altered, and this remains to be investigated further.

4OI administered at 100 mg/kg over 45 days did not extend lifespan as anticipated. Several other recent treatment strategies (Ferrari et al., 2017; Johnson et al., 2013; Johnson et al., 2015; Lee et al., 2019) improved the P55 NDUFS4 KO median lifespan from P100 up to P270. Therefore, it was disappointing that 4OI did not confer additional survival to the KO mice. Despite this, 4OI had several beneficial trends to improve clinical measures such as body temperature, gait, and development of curling in NDUFS4 KO mice. Quality of life in Leigh syndrome patients is reduced as a result of being wheelchair-bound due to motor impairments and being hospitalized following minor infections with a slower recovery (Cavanagh and Harding, 1994; Van Coster et al., 1991). Therefore, the benefits of 4OI on quality of life outcomes are worth investigating independent of the effects on limiting disease progression.

The lack of significant changes to microglial levels or the inflammatory state of the OB with the 4OI (100 mg/kg) over 14 days of treatment was initially surprising. However, this confirms our previous observation that increased inflammatory signaling appears to be absent in the NDUFS4 KO OB (**Figure 2.26, 3.7, 3.8**). 4OI had no significant impact on the targets (*Tnfa*, *Nlrp3*, *Irg1*, and *Hmox1*) that were modulated *in vivo* in the presence of pro-inflammatory LPS.

However, we detected increased PSD95 in the NDUFS4 KO cerebellum with 14 d 4OI (100 mg/kg) treatment. Therefore, the beneficial effects of 4OI may arise from alternative microglial modulation, for example, by pruning synapses in neurodevelopment or direct effects on the impaired neurons in the NDUFS4 KO brain. 4OI is an ester form of itaconate that will chemically modify protein thiols when it enters the cell. This activity is similar to the fumarate ester dimethyl fumarate (DMF), which is used clinically for the treatment of relapsing-remitting multiple sclerosis (Gold et al., 2015). DMF has been shown to modify Keap1 to augment NRF2 driven antioxidant response and modify protein kinase C θ to decrease T cell reactive oxygen species production (Linker et al., 2011; Blewett et al., 2016; Wu et al., 2018). In addition, DMF is known to modulate the actin and tubulin-associated proteins, cofilin-1, and collapsing response mediator protein 2 (CRMP2), thereby modulating the cytoskeleton (Piroli et al., 2019). It is expected that exogenous itaconate may modulate a similar range of targets, and these actions may contribute to neuroprotection at growth cones or synaptic processes, which may benefit the NDUFS4 knockout mouse during development. Further evidence that 4OI may act through direct neuronal regulation is suggested by the fact that itaconate improves viral resistance in primary neuronal cultures (Daniels et al., 2019). Therefore, further exploration at a proteomic level is needed to determine the mechanism underlying 4OI-derived preservation of motor endurance in the NDUFS4 KO mouse.

While 4OI treatment serves as a surrogate for endogenous itaconate, itaconate and its derivatives act distinctly. While macrophages take up itaconate

and its derivatives (dimethyl itaconate and 4-octyl itaconate), these derivatives act directly instead of being metabolized into itaconate (Swain et al., 2020). Dimethyl itaconate and 4-octyl itaconate strongly induce the NRF2 electrophilic stress and inhibit IκBζ, IL-6, and IL-10 in contrast to itaconate. While they all inhibit ATP-induced increases in the IL-1β independent of NRF2, 4-octyl itaconate and dimethyl itaconate inhibit pro-IL-1β production, unlike itaconate. Surprisingly, itaconate pretreatment increased the LPS-induced production of IFN-β, in contrast to the inhibitory effects of dimethyl itaconate and 4-octyl itaconate (Swain et al., 2020). Therefore, itaconate acts as a crucial immunomodulator, and derivatives, including 4OI, have distinct effects through their unique electrophilic profiles. This will need to be considered as these derivatives actions are studied in the future.

We found that 4OI treatment promotes an anti-inflammatory phenotype in microglia exposed to LPS *in vitro*. In addition, 4OI administration significantly slowed NDUFS4 KO-induced decline in endurance in males. 4OI administration demonstrated encouraging trends in clinical symptom improvement as shown by reductions in NDUFS4 KO-induced right gait overlap and slowing of NDUFS4 KO-induced decline in body temperature and increase in hindlimb curling. Therefore, 4OI offers some promise as a therapeutic alternative for NDUFS4 KO mice and Leigh syndrome patients.

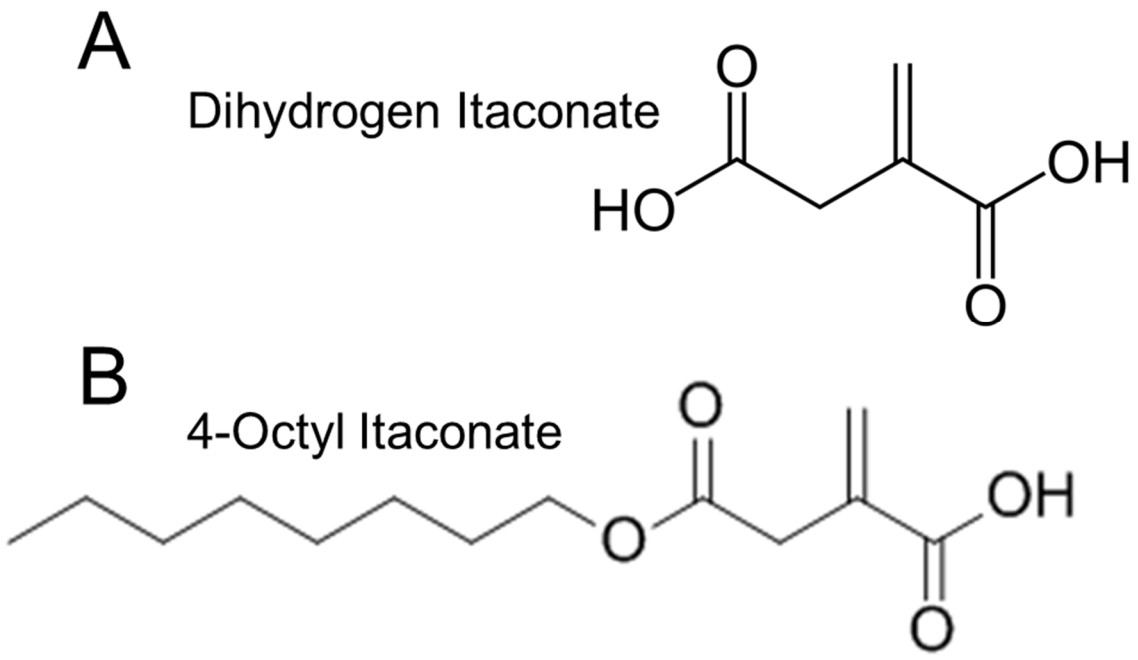

Figure 3.1 The Structure of Itaconate and 4-Octyl Itaconate. The addition of an octyl group to itaconate confers cell membrane permeability and should permit 4OI to cross the blood-brain barrier.

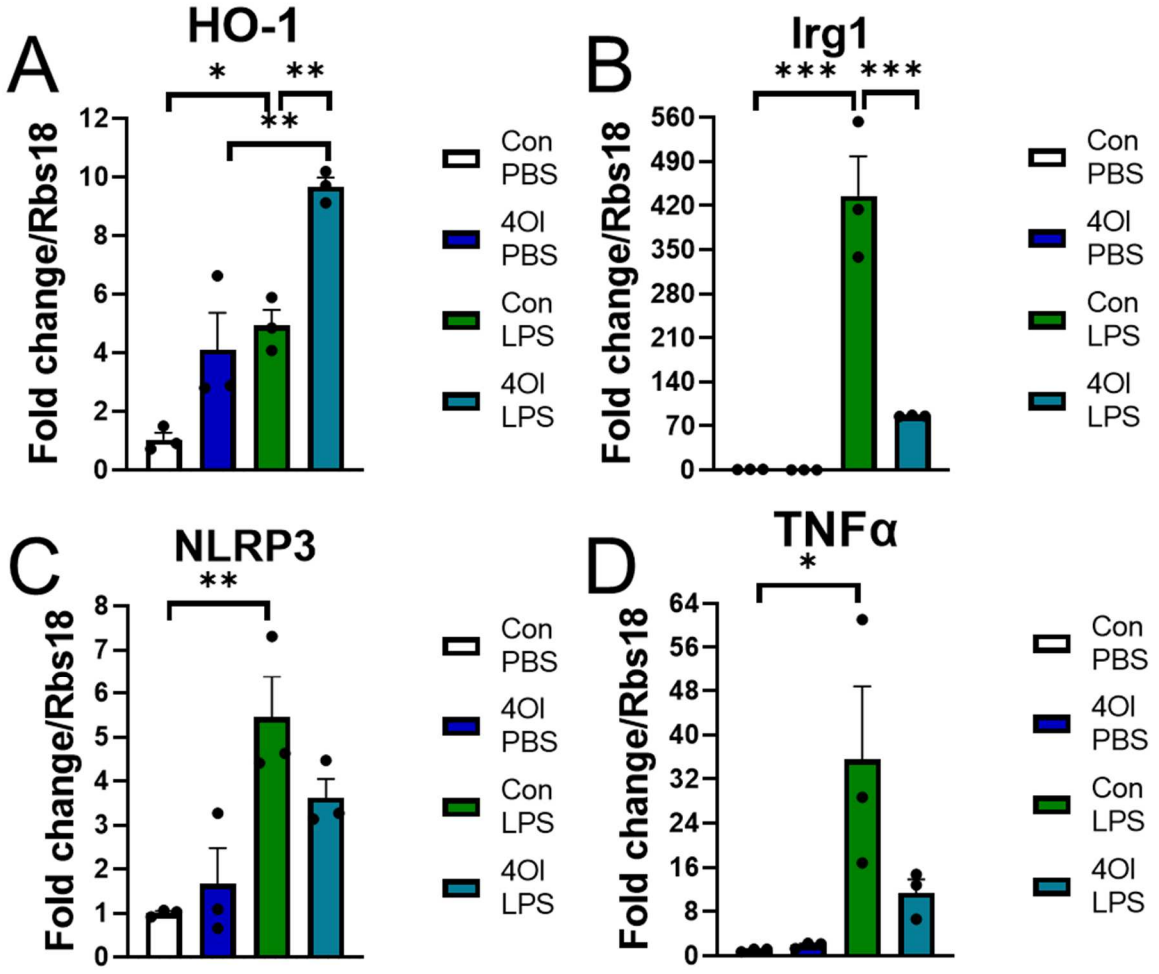

Figure 3.2 4-Octyl Itaconate Promotes an Anti-inflammatory Phenotype *in vitro*. Gene expression in HAPI microglial cells pretreated 2 h ±62.5 µM 4OI prior to stimulation for 18 h ±5 µg/mL LPS was measured by qRT-PCR. **A-D**: LPS stimulation increased the expression of *Irg1* and *Hmox1* in addition to pro-inflammatory *Nlrp3* and *Tnfa*. 4OI pretreatment prevented LPS-induced increases in *Irg1* and pro-inflammatory *Nlrp3* and *Tnfa* and enhanced LPS-induced increases in anti-inflammatory *Hmox1* gene expression. Data are mean ± SE (*p < 0.05; **p < 0.01; ***p < 0.001; two-way ANOVA) with n=3/group.

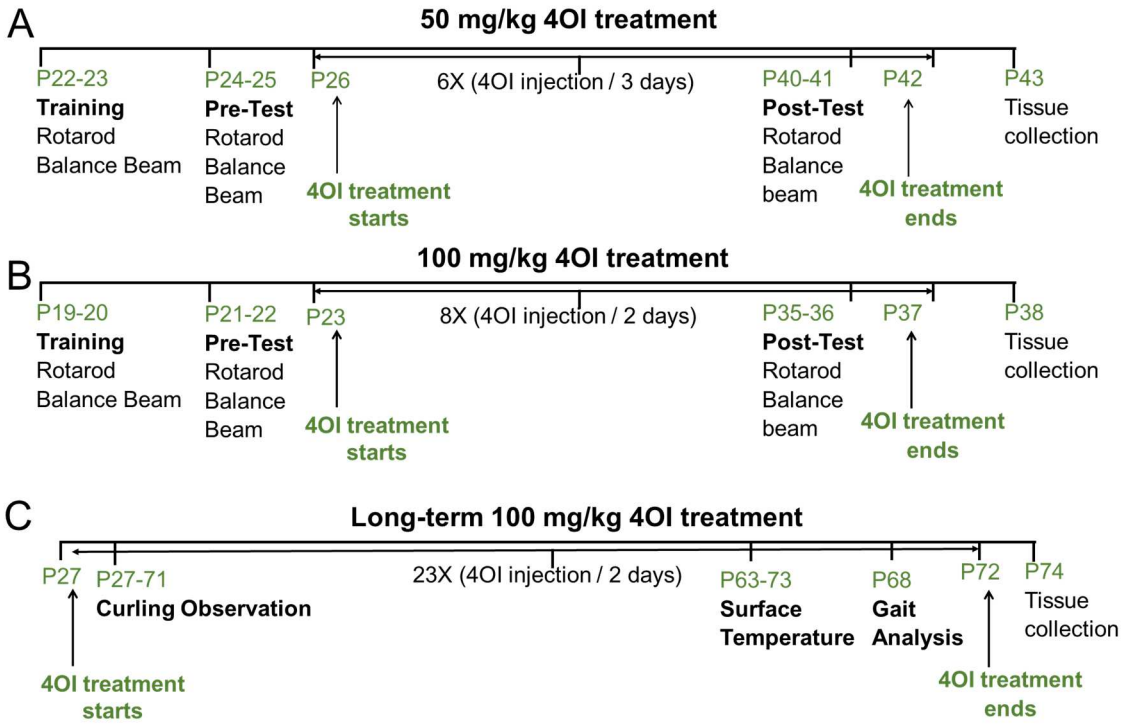

Figure 3.3 Overview of 4OI Treatment Strategies. A: P22 mice were habituated prior to baseline testing on the rotarod and an inclined balance beam prior to intraperitoneal injections of ±50 mg/kg 4OI (once every 3 d) for 16 d. Following this, the motor behaviors were again assessed at P40-41 prior to sacrifice and tissue collection. **B**: P19 mice were habituated and given baseline testing in the rotarod and inclined balance beam behaviors before intraperitoneal injections of ±100 mg/kg 4OI (every other day) for 14 d. Following this, the motor behaviors were again assessed at P35-36 prior to sacrifice and tissue collection. **C**: P27 mice were given intraperitoneal injections of ±100 mg/kg 4OI (every other day) for 45 d to determine if 4OI treatment would improve NDUFS4 KO mouse survival. From P27-71, mice were observed for the development of NDUFS4 KO-induced hindlimb curling. From P63-73, the surface temperature of mice was taken. The gait of P68 mice was analyzed using painted paw print patterns along a path to a food reward. P74 mice were sacrificed, and tissue was collected for later analysis.

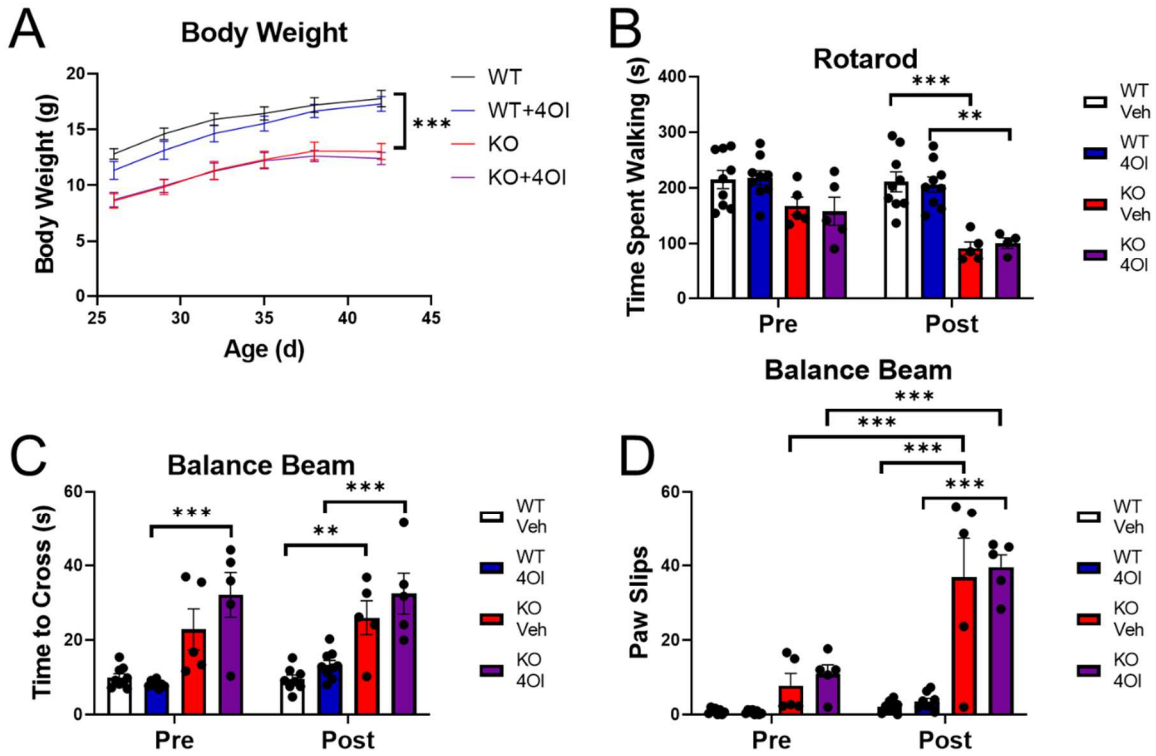

Figure 3.4 4-Octyl Itaconate (50 mg/kg) Does Not Significantly Improve NDUFS4 Knockout Motor Behavior. NDUFS4 KO mice were IP-injected ±50 mg/kg 4OI once every 3 days for 15 d. **A**: While NDUFS4 KO mice have decreased body weight, 4OI treatment did not noticeably alter body weight for WT or NDUFS4 KO mice. **B-D**: Mice were given the rotarod and inclined balance beam behavioral tasks with a baseline test before 4OI treatment and a post-treatment test after. NDUFS4 KO mice have decreased time walking (**B**), increased time to cross the beam (**C**), and increased number of paw slips (**D**). However, 4OI treatment does not noticeably impact motor activity for WT or NDUFS4 KO mice (**B-D**). Data are mean ± SE (**p < 0.01; ***p < 0.001; two-way ANOVA) with n=5-8/group.

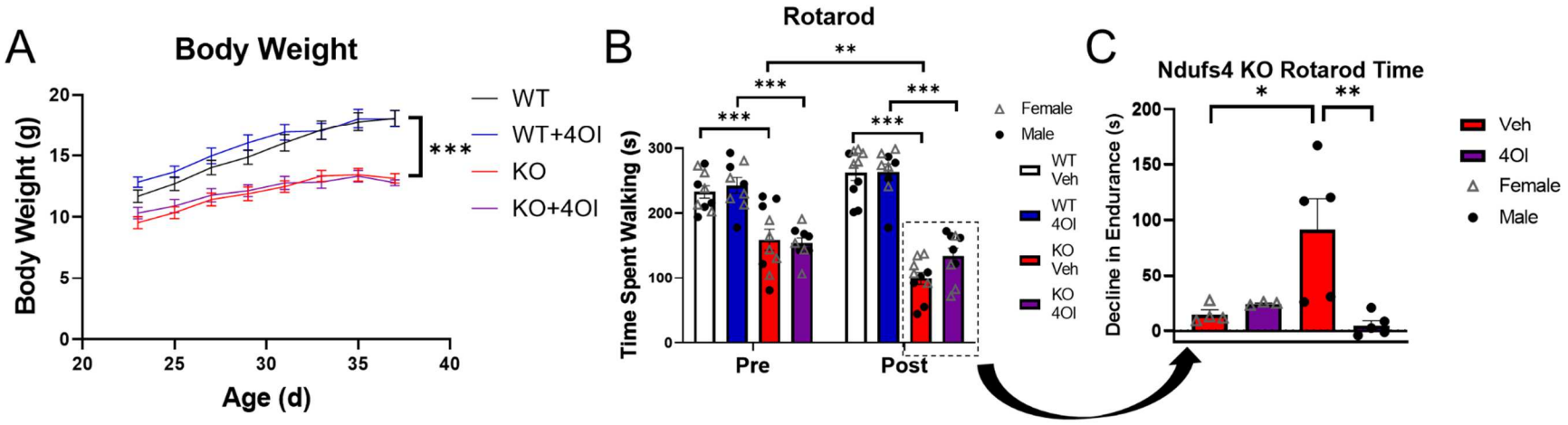

Figure 3.5 4-Octyl Itaconate (100 mg/kg) Significantly Slows NDUFS4 Knockout-Induced Decline in Motor Endurance in Males. NDUFS4 KO mice were IP-injected ±100 mg/kg 4OI once every 2 days for 16 d. **A**: While NDUFS4 KO mice have decreased body weight, 4OI treatment did not noticeably alter body weight for WT or NDUFS4 KO mice. **B-C**: Mice were given the rotarod behavioral task with a baseline test before 4OI treatment and a post-treatment test after. While NDUFS4 KO mice had decreased motor endurance (**B**), 4OI treatment slowed NDUFS4 KO-induced decline in motor endurance by 94% in male mice (**C**). Data are mean ± SE (*$p < 0.05$; **$p < 0.01$; ***$p < 0.001$; two-way ANOVA) with n=3-5/group.

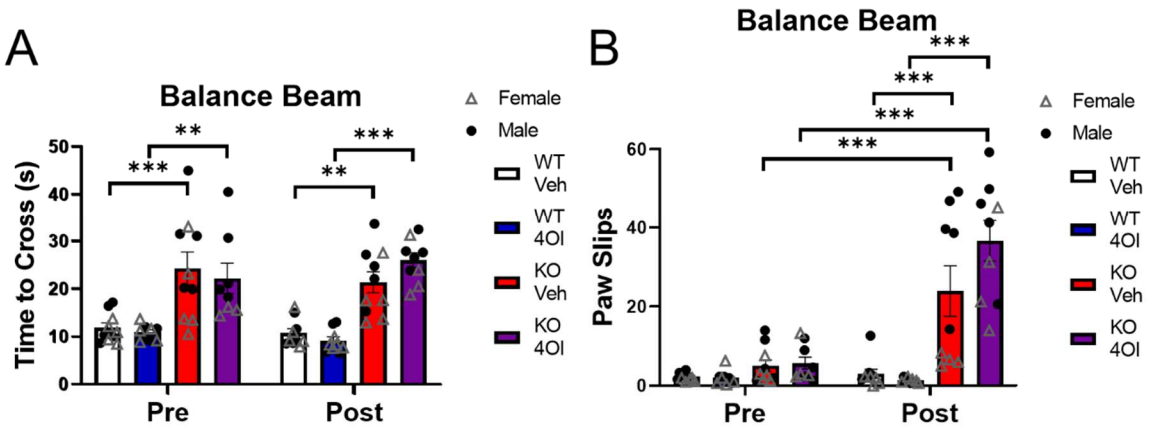

Figure 3.6 4-Octyl Itaconate (100 mg/kg) Does Not Alter NDUFS4 Knockout-Induced Decreases in Motor Coordination. NDUFS4 KO mice were IP-injected ±100 mg/kg 4OI once every 2 days for 16 d. **A-B**: Mice were given the inclined balance beam behavioral task with a baseline test before 4OI treatment and a post-treatment test after. NDUFS4 KO mice have increased time to cross (**A**) and the number of paw slips (**B**). However, 4OI does not significantly alter either the time to cross or the number of paw slips in WT and NDUFS4 KO mice (**A-B**). Data are mean ± SE (**p < 0.01; ***p < 0.001; two-way ANOVA) with n=4-5/group.

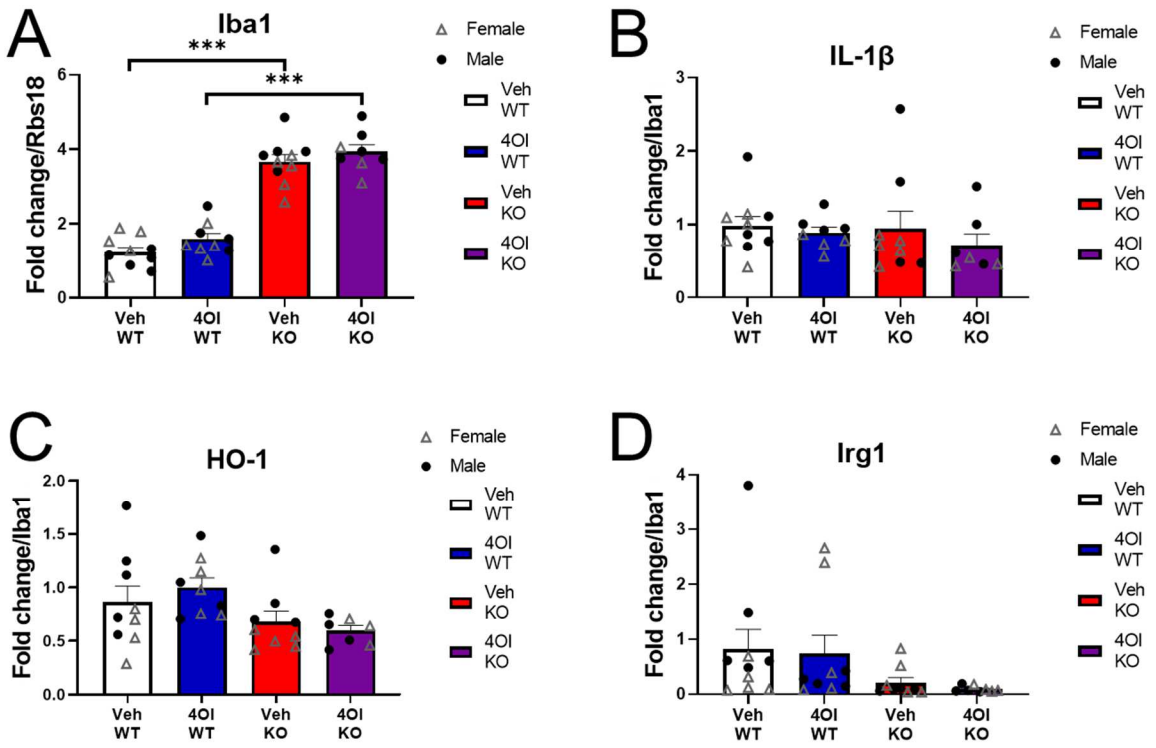

Figure 3.7 4-Octyl Itaconate (100 mg/kg) Does Not Significantly Alter Olfactory Bulb Inflammatory Gene Expression. NDUFS4 KO mice were IP-injected ±100 mg/kg 4OI once every 2 days for 16 d. Gene expression in the OB of WT and NDUFS4 KO mice was measured by qRT-PCR. **A-D**: While the NDUFS4 KO OB had increased *Iba1*, no increases in *Il1b*, *Hmox1*, or *Irg1* were detected. 4OI treatment does not noticeably impact OB gene expression in WT or NDUFS4 KO mice. Data are mean ± SE (***p < 0.001; two-way ANOVA) with n=3-5/group.

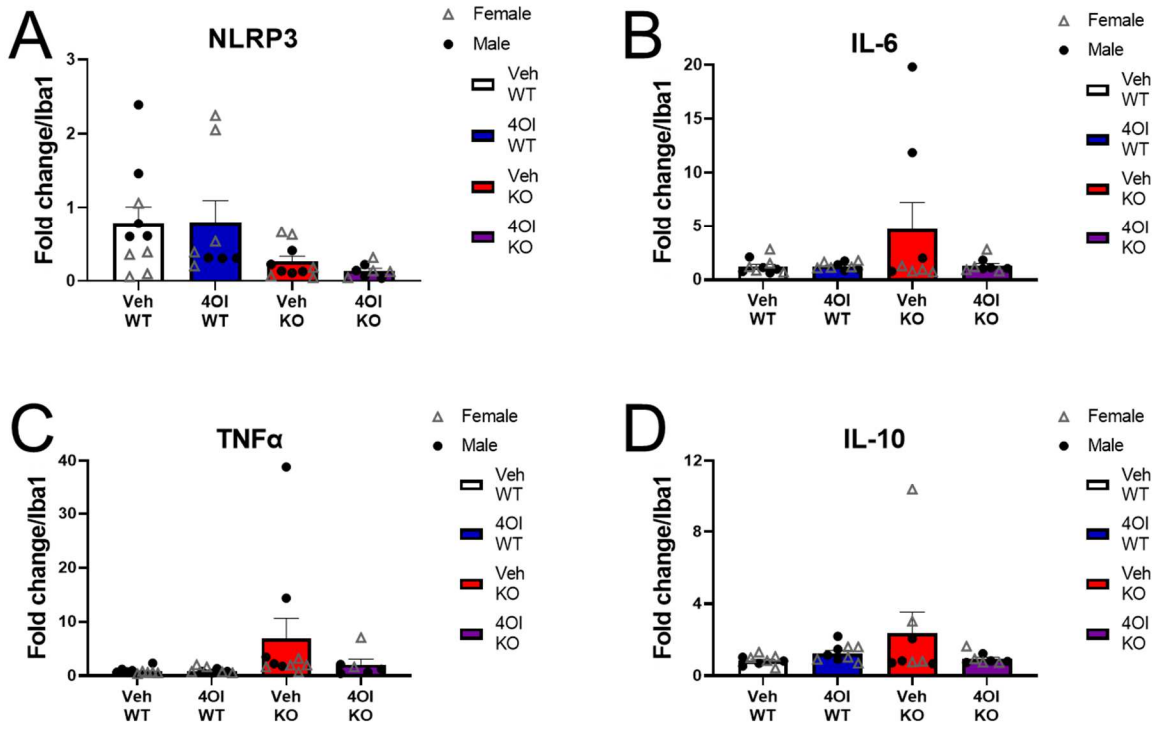

Figure 3.8 4-Octyl Itaconate (100 mg/kg) Does Not Significantly Alter Olfactory Bulb Inflammatory Gene Expression. NDUFS4 KO mice were IP-injected ±100 mg/kg 4OI once every 2 days for 16 d. Gene expression in the OB of WT and NDUFS4 KO mice was measured by qRT-PCR. **A-D**: Knockout of NDUFS4 did not alter the gene expression of *Nlrp3*, *Il6*, *Tnfa*, or *Il10*. 4OI treatment does not noticeably impact OB gene expression in the WT or NDUFS4 knockout mouse olfactory bulb. Data are mean ± SE (two-way ANOVA) with n=2-5/group.

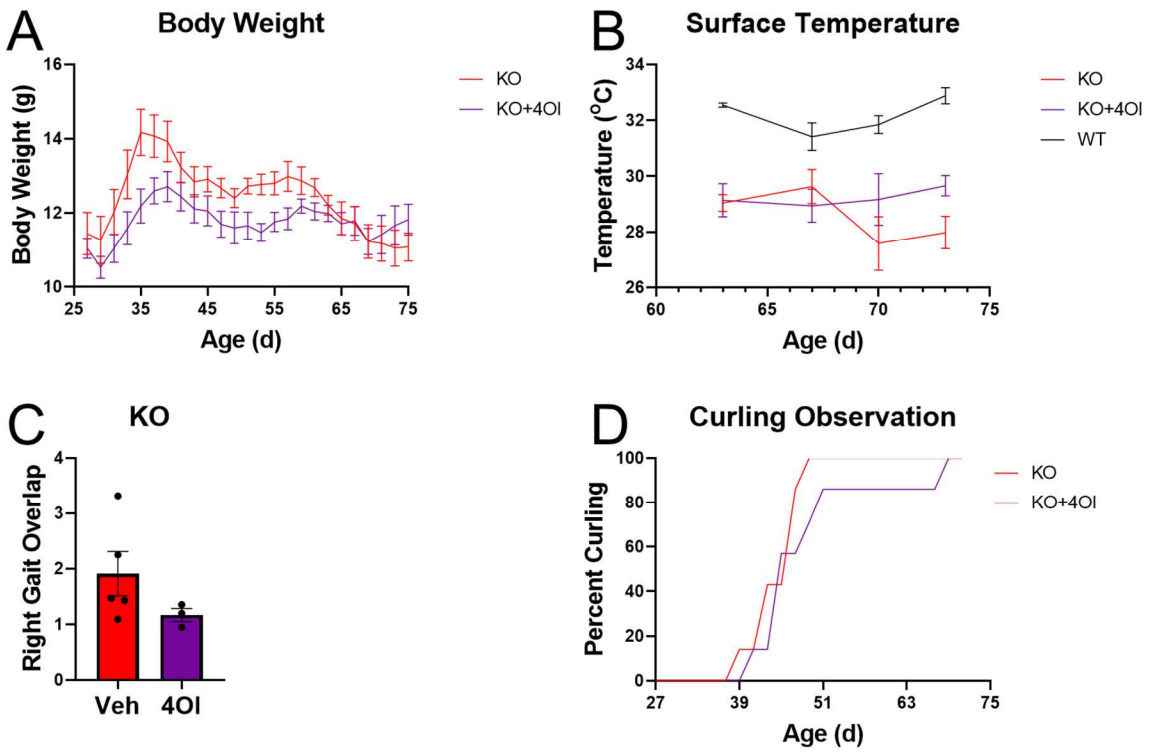

Figure 3.9 4-Octyl Itaconate (100 mg/kg) Treatment Improves the Body Temperature and Gait of NDUFS4 Knockout Mice. NDUFS4 KO mice were IP-injected ±100 mg/kg 4OI once every 2 days for 45 d. **A-B**: 45 d 4OI treatment did not noticeably alter body weight but tended to slow the decline in surface temperature in NDUFS4 KO mice. Data are mean ± SE (repeated measures ANOVA) with n=5-7/group. **C**: The gait of NDUFS4 KO mice was measured by recording the painted paw prints of mice walking on paper to a food reward. 4OI treatment decreased right gait overlap, a measure of imbalance, by 50% versus vehicle-treated KOs. Data are mean ± SE (unpaired t-test with Welch's correction) with n=3-5/group. **D**: The development of NDUFS4 KO-induced hindlimb curling was measured from P27-73. 4OI-treated NDUFS4 KO mice tended to develop curling behaviors slower than untreated KOs. By P49, 71% of 4OI-treated NDUFS4 KO mice had developed curling by P49 in contrast to 100% of vehicle controls. Data are mean with n=5-7/group.

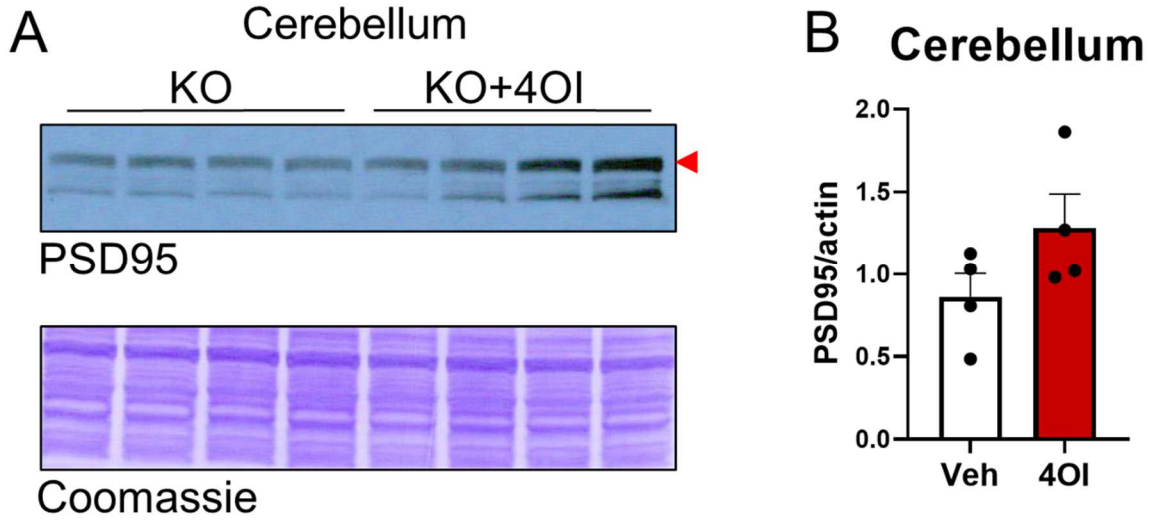

Figure 3.10 4-Octyl Itaconate Treatment Increased PSD95 in the NDUFS4 Knockout Cerebellum. NDUFS4 KO mice were IP-injected ±100 mg/kg 4OI once every 2 days for 16 d. **A-B**: Protein lysates (30 µg protein) from the cerebellum of P38 NDUFS4 KO mice were separated by SDS-PAGE followed by immunoblotting. 4OI treatment increased the levels of PSD95, a neuronal marker of synapses, indicated by the upper band (red arrow) in the NDUFS4 KO cerebellum. Coomassie staining was used as a loading control (n=4/group). Band intensity was quantified by densitometry with ImageJ software (NIH; http://rsbweb.nih.gov/ij/). Data are mean ± SE (unpaired t-test with Welch's correction) with n=4/group.

CHAPTER 4

QUANTIFICATION OF 2-HYDROXYGLUTARATE AND LACTATE ENANTIOMERS IN THE NDUFS4 KNOCKOUT MOUSE

McCain, R.S.[1], Piroli, G.G.[1], Smith, H.H.[1], Cotham, W.E.[2], Walla, M.D.[2], and Frizzell, N.[1]

1) Department of Pharmacology, Physiology & Neuroscience, School of Medicine, University of South Carolina, Columbia, SC 29209, USA
2) Department of Chemistry and Biochemistry, University of South Carolina, Columbia, SC 29208, USA

To be submitted

4.1 Introduction

Chapters 2 and 3 primarily focused on the impaired metabolism of non-neuronal cell populations in the NDUFS4 KO. In separate studies performed in our laboratory, we investigated the fumarate-mediated succination of the mitochondrial protein dihydrolipoyllysine-residue succinyltransferase (DLST) (Piroli et al., 2021). DLST is the E2 component of the α-ketoglutarate dehydrogenase (αKGDH) complex that mediates the oxidative decarboxylation of α-ketoglutarate to succinyl CoA (Sheu and Blass, 1999), and its localization appears to be restricted exclusively to neurons (Dobolyi et al., 2020). Succination of DLST by fumarate reduces the activity of the α-KGDH complex by ~25% in the OB and BS of NDUFS4 KO mice. This reduced activity results in decreased succinate and reduced substrate-level phosphorylation, an important alternative for ATP generation in the bioenergetically compromised NDUFS4 KO (Piroli et al., 2021). We were surprised to note that despite the reduced activity of the αKGDH complex, the upstream TCA metabolite α-ketoglutarate (αKG) did not accumulate (**Figure 2.9**). This lack of accumulation led us to consider alternative fates of αKG, including the production of 2-hydroxyglutarate (**Figure 4.1, 4.2**).

While malate dehydrogenase (MDH2) normally favors the redox conversion of malate to oxaloacetate, the promiscuous activity of MDH2 during metabolic acidosis favors the generation of the metabolite L-2-hydroxyglutarate (L-2-HG) from αKG (**Figure 4.1**) (Nadtochiy et al., 2016; Intlekofer et al., 2017). The formation of L-2-HG by MDH2 under acidic conditions utilizes NADH rather than NAD^+, and this would be favored in the NDUFS4 KO model where the NADH/NAD^+

ratio is elevated and lactic acidosis is present (Kruse et al., 2008; Quintana et al., 2010). These conditions also promote fumarate accumulation (as the MDH2-mediated forward conversion of malate is limited), contributing to sustained succination in neurons (Chapter 1, section 1.4.3). A mechanism to remove accumulated L-2-HG is also present, whereby the FAD^+-dependent L-2-HG dehydrogenase (L2HGDH) converts L-2-HG back to αKG while generating $FADH_2$. The importance of L-2-HG removal was only recognized when it was realized that mutations in L2HGDH are the cause of L-2-HG aciduria (Christen et al., 2021; Du et al., 2021). Patients with L2HGDH mutations develop hydroxyglutaric aciduria, cerebellar ataxia, and delayed development, similar to other mitochondrial encephalopathies (Mazzei et al., 2011; Ullah et al., 2018; Zhang et al., 2018B). L-2-HG has also been described as an immunometabolite that enhances the proliferation and persistence of $CD8^+$ T cells (Tyrakis et al., 2016), and its increases during hypoxia have been shown to act as a reservoir for reducing equivalents (Intlekofer et al., 2015; Oldham et al., 2015).

In contrast to L-2-HG, its enantiomer D-2-hydroxyglutarate (D-2-HG) is generated by the enzyme D-3-phosphoglycerate dehydrogenase (PHGDH) (**Figure 4.2**). PHGDH is the first enzyme in the serine biosynthetic pathway but has a promiscuous activity to generate D-2-HG (and not L-2-HG) when αKG is abundant (Fan et al., 2015). This activity has been documented in select cancers, leading to the consideration of D-2-HG as an oncometabolite (Fan et al., 2015; Zhao and Winkler, 1996; Bunse et al., 2018). Somatic mutations in isocitrate dehydrogenase (IDH) also result in specific D-2-HG accumulation, and these

mutations occur in >80% of patients with diffuse WHO grade II-III gliomas (Reiter-Brennan et al., 2018; Ye et al., 2018). In this context, D-2-HG may also act as an immunometabolite that suppresses the immune system by decreasing the proliferation of $CD8^+$ T cells, the polarization of Th17 cells, and complement-mediated phagocytosis (Kohanbash et al., 2017; Zhang et al., 2018A). A D-2-HG specific dehydrogenase also exists and can convert the D-2HG back to αKG while generating $FADH_2$. Mutations in D2HGDH also result in hydroxyglutaric acidurias, with encephalopathic phenotypes similar to those caused by L2HGDH mutations (Ye et al., 2018; Struys et al., 2005).

The accumulation of L-2-HG and D-2-HG has been shown to have relevance in metabolic reprogramming. These metabolites, particularly L-2-HG, inhibit αKG-dependent dioxygenases by competing with the α-KG-binding site, e.g., ten-eleven translocation 2 (TET2) and Jumonji-C (JmjC) histone demethylases (Ye et al., 2018). This drives epigenetic reprogramming as histone methylation regulates gene expression (**Figure 4.3**). We hypothesized that acidic conditions observed in the NDUFS4 KO, in parallel with reduced α-KGDH complex activity, would favor the increased production of L-2-HG. If L-2-HG is accumulated, it may further impact metabolic reprogramming in the NDUFS4 KO brain through altered histone methylation.

Since 2-HG exists as both L and D enantiomers, the derivatization of functional groups is usually employed to resolve these enantiomers by liquid chromatography-mass spectrometry (LC-MS) (Oldham and Loxcalzo 2016; Struys et al., 2004; Trefely et al., 2019). We employed chiral derivatization with diacetyl-

l-tartaric anhydride (DATAN) to accurately discriminate between the 2-HG enantiomers (Oldham et al., 2015). DATAN derivatization followed by liquid chromatography-mass spectrometry (LC-MS) reduces the time, cost, and racemization of analytes compared to gas chromatography-mass spectrometry protocols. This protocol uses lactate added to the low concentrations of the standards to facilitate their derivatization as it also contains a hydroxyl group (**Figure 4.4**). However, we reasoned that by substituting lactate with malate (whose hydroxyl group may also be derivatized by DATAN, **Figure 4.4C**), we might improve this method to allow the simultaneous detection of both 2-HG and lactate enantiomers. DATAN has been used previously to derivatize D- and L-lactate in separate analyses (Scheijen et al., 2012). Therefore, we report the successful adaptation of this method to simultaneously detect 2-HG levels in parallel with lactate quantification, providing a reliable estimation of lactic acidosis in select brain regions of the NDUFS4 KO.

4.2 Results

To determine if L-malate could be used to replace lactate as a carrier for the 2-HG standard derivatization, we derivatized standards of 2-HG and lactate and confirmed their resolution by LC-MS, the added malate was also detected based on its unique fragmentation pattern. Malate was only added to the standards to improve derivatization as the samples contained endogenous malate. Both enantiomers of 2HG, as well as L-lactate and L-malate, were monitored for all subsequent analyses with tissue samples. Representative extracted ion chromatograms from the derivatization of WT mouse serum (**Figure 4.5**) shows all

enantiomers were detected with separate retention times by LC. The unique masses of product ions derived from the fragmentation of these metabolites by mass spectrometry were used to confirm their identity by LC-MS. The derivatized L-malate was also detected (lower panel) (**Figure 4.5**). We did not detect D-lactate as serum D-lactate does not accumulate to appreciable amounts *in vivo* (Ewaschuk et al., 2005). Isotope dilution mass spectrometry was performed to determine the concentration of the metabolites of interest. All samples and standards were spiked with a fixed amount of isotopic D,L-2-HG and L-Lactate (See Methods). Peak area ratios were calculated for the known standards and used to calculate the absolute metabolite amounts.

P42 WT and NDUFS4 KO mouse OB and BS were analyzed following DATAN derivatization by LC-MS to determine 2-HG enantiomer and L-lactate levels. NDUFS4 KO mice had increased malate in the OB and BS compared to WT controls (**Figure 4.6**). This expected result supports our previous analysis of malate levels by GC-MS. In addition, L-lactate increased by 60% in the BS (8.09 nmol/mg in KO versus 4.96 nmol/mg in WT) and 40% in the OB (4.616 nmol/mg in KO versus 3.287 nmol/mg in WT) with knockout of NDUFS4 (**Figure 4.7**). Quantification of L-2-hydroxyglutarate in the olfactory bulb demonstrated no change, but a striking 26% decrease in brainstem L-2-HG was detected in NDUFS4 KO versus WT (**Figure 4.8**). In contrast, we measured a 57% decrease in olfactory bulb D-2-HG and no change in brainstem D-2-HG with knockout of NDUFS4, suggesting region-specific differences in metabolite dynamics (**Figure 4.9**).

We analyzed the levels of lactate and 2-hydroxyglutarate in P49 WT and NDUFS4 KO mouse serum to quantify systemic metabolite levels. While the level of L-lactate increased 40% as expected, the levels of L-2-HG were decreased 28% in NDUFS4 KO serum versus WT (**Figure 4.10A-B**). In addition, we quantified a remarkable 61% decrease in D-2-HG in NDUFS4 KO serum versus WT (**Figure 4.10C**). While the decrease in L-2-HG or D-2-HG was surprising in select brain regions, the serum measurements validate these findings and suggest that both enantiomers are selectively reduced in tissues of the NDUFS4 KO versus WT.

4.3 Discussion

We successfully adapted and improved an existing protocol to permit the simultaneous detection of lactate and 2-hydroxyglutarate enantiomers. We measured increased malate and an ~1.5-fold increase in lactate with knockout of NDUFS4, which confirmed the expected lactic acidosis throughout the body (Thompson Legault et al., 2015; Ferrari et al., 2017; Sharma et al., 2021). The confirmation of increased lactic acidosis in these regions affected by the pathology underscored the premise for the proposed L-2-HG measurement, as it was also expected to increase. Surprisingly, knockout of NDUFS4 did not alter basal levels of L-2-HG in the OB, where we had detected reduced activity of the α-ketoglutarate dehydrogenase complex (Piroli et al., 2021). In contrast to our original hypothesis, L-2-hydroxyglutarate decreased by 26% in the BS (**Figure 4.1, 4.8**). These data, while striking, also confirmed that L-2-HG does not appear to have a significant role in regulating histone demethylases (**Figure 4.3**). While we did not originally consider D-2-HG levels, this metabolite was also quantified in parallel with L-2-HG,

and we immediately noted that levels of D-2-HG were markedly reduced in the OB, with a 57% decrease with knockout of NDUFS4. In contrast to L-2-HG, D-2-HG levels were unchanged in the brainstem.

WT and NDUFS4 KO serum was used to quantify systemic metabolite levels. While we measured a 40% increase in L-lactate, the levels of L-2-HG were decreased by 28%, and the levels of D-2-HG were decreased by 61% in NDUFS4 KO serum versus WT (Figure 4.6A-C). Since serum findings were consistent for both enantiomers and were significantly reduced in the knockout versus wild-type, this suggests that this reduction may be a specific biomarker for this Complex I deficit.

As the metabolites were reduced rather than increased, this suggests that basal levels of these metabolites may be utilized. Our methods were limited in that we were not detecting the fate of αKG in these experiments. We expected acidosis to favor L-2-HG generation, and this may occur, but the subsequent L2HGDH mediated reduction to αKG may be favored to generate precious $FADH_2$, which can supply electrons to Complex II (Du et al., 2021; Leong et al., 2012; Quintana et al., 2010). $FADH_2$ offers the benefit of bypassing the NDUFS4 KO-induced Complex I bioenergetic deficit by funneling electrons to a functional complex that delivers them to ubiquinone for subsequent transit to Complex III (Du et al., 2021; **Figure 4.1**). 2-hydroxyglutarate, as a source of $FADH_2$ for Complex II, may in part explain why oxidative phosphorylation continues to be supported in NDUFS4 KO mice with the loss of Complex I (**Figure 2.10**).

It remains unclear why brain region-specific differences were observed in the reductions in these metabolites. However, it is interesting to speculate that variable expression of the associated dehydrogenases, L2HGDH and D2HGDH, is associated with the varied expression of 2-HG enantiomers. Alternatively, the differences in 2-HG levels may reflect region-specific metabolic dynamics with the 1.5-fold increase in L-lactate and ≥5-fold increase in L-2-HG in the WT and NDUFS4 KO brainstem compared to the olfactory bulb. The decrease in serum 2-HG levels with increased L-lactate suggests that 2-HG may be used systemically to maintain limited mitochondrial oxidative phosphorylation. Therefore, supplementation with the α-ketoglutarate ester DMKG may provide systemic benefits to NDUFS4 KO mice (Lee et al., 2019).

In summary, the robust reduction in 2-HG enantiomers in brain regions and serum of the NDUFS4 KO mouse suggest that these metabolites may have as yet unappreciated roles in supporting metabolism through alternative delivery of electrons derived from αKG oxidation. Further analyses of L2HGDH and D2HGDH enzyme activity coupled with the assessment of rates of production will be necessary to determine the synthesis and fate of these metabolites.

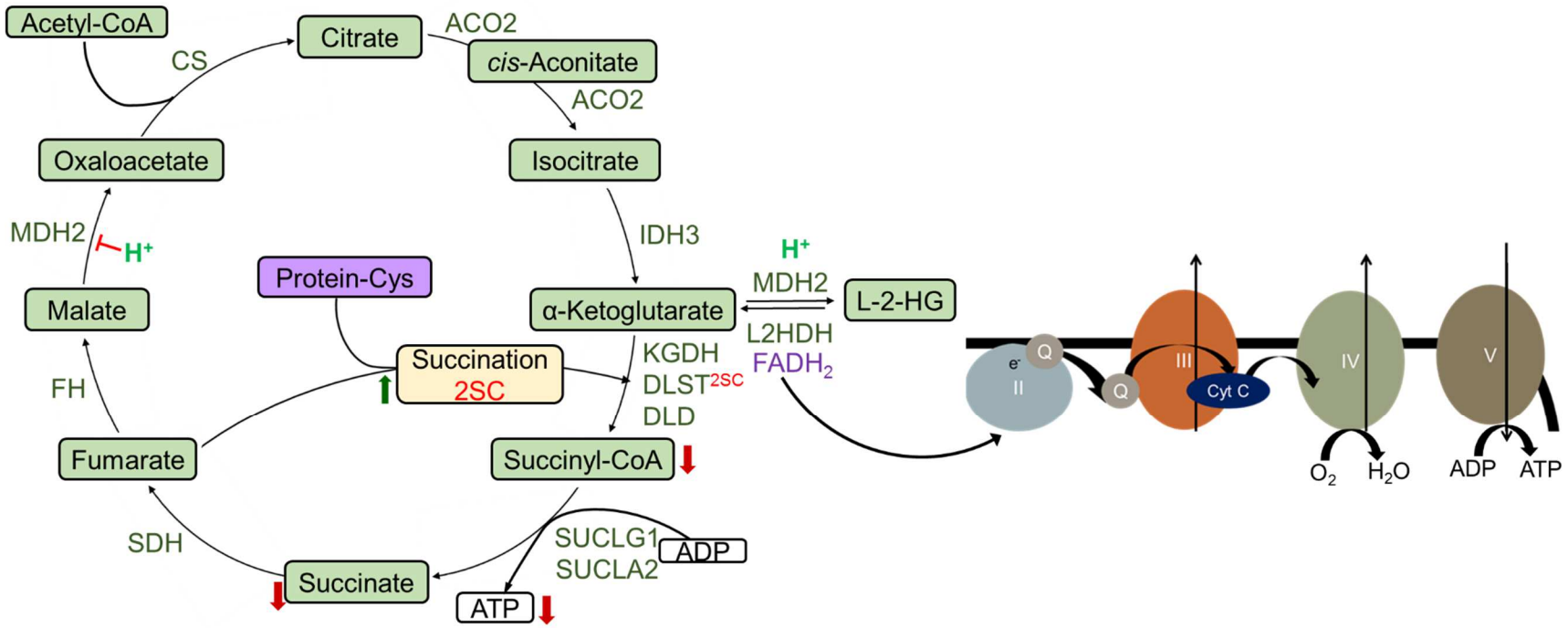

Figure 4.1 Production of L-2-Hydroxyglutarate in the NDUFS4 Knockout Mouse. Succination of DLST inhibits the α-ketoglutarate dehydrogenase complex, decreasing succinate, succinyl-CoA, and substrate-level phosphorylation with knockout of NDUFS4. However, α-ketoglutarate levels do not increase in the NDUFS4 KO OB. L-2-hydroxyglutarate is produced from α-ketoglutarate by malate dehydrogenase (MDH2) during lactic acidosis (H^+). L-2-hydroxyglutarate can be oxidized by an L-2-HG dehydrogenase to α-ketoglutarate while generating $FADH_2$. Complex II uses $FADH_2$ to produce ATP through oxidative phosphorylation, bypassing Ndufs4 KO-induced impairments to Complex I.

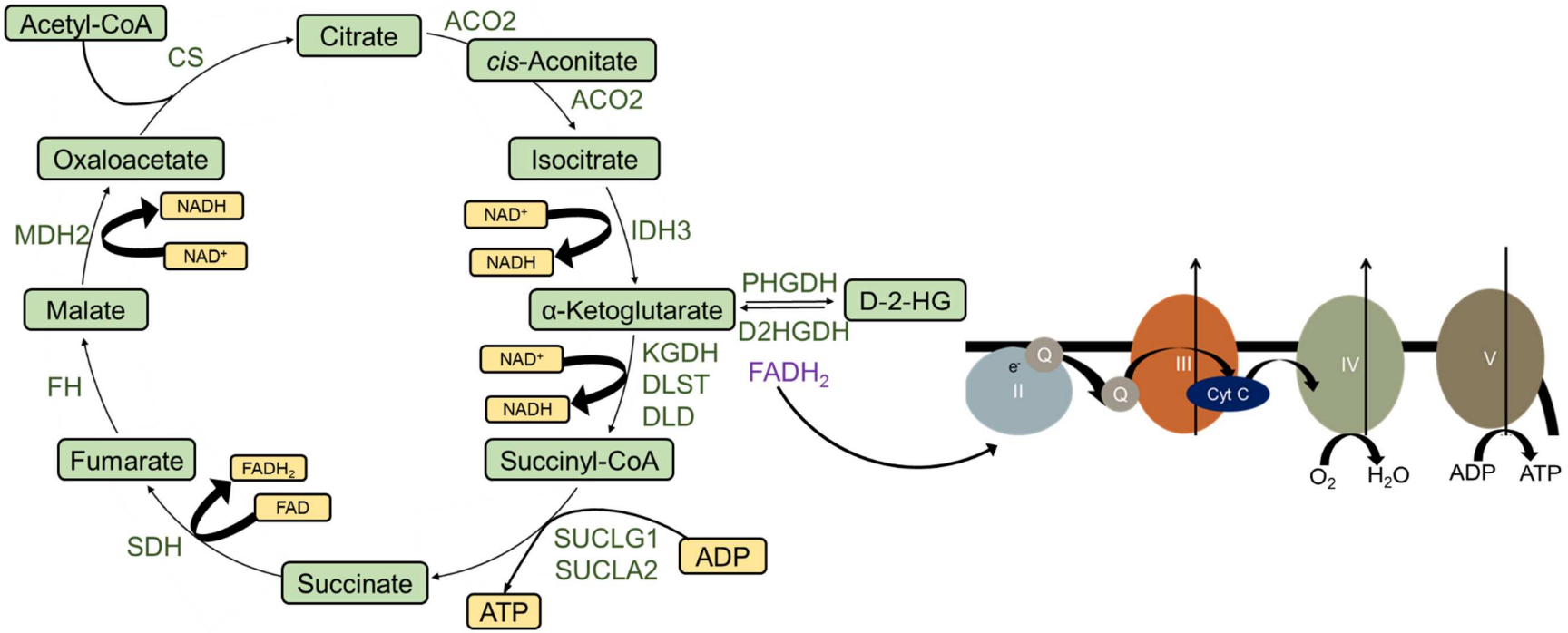

Figure 4.2 Production of D-2-Hydroxyglutarate from α-Ketoglutarate. D-2-hydroxyglutarate is produced from α-ketoglutarate by phosphoglycerate dehydrogenase (PHGDH). Accumulated D-2-hydroxyglutarate can be oxidized by D-2-HG dehydrogenase to α-ketoglutarate to generate $FADH_2$. Complex II uses $FADH_2$ to produce ATP through oxidative phosphorylation, bypassing Ndufs4 KO-induced impairments to Complex I.

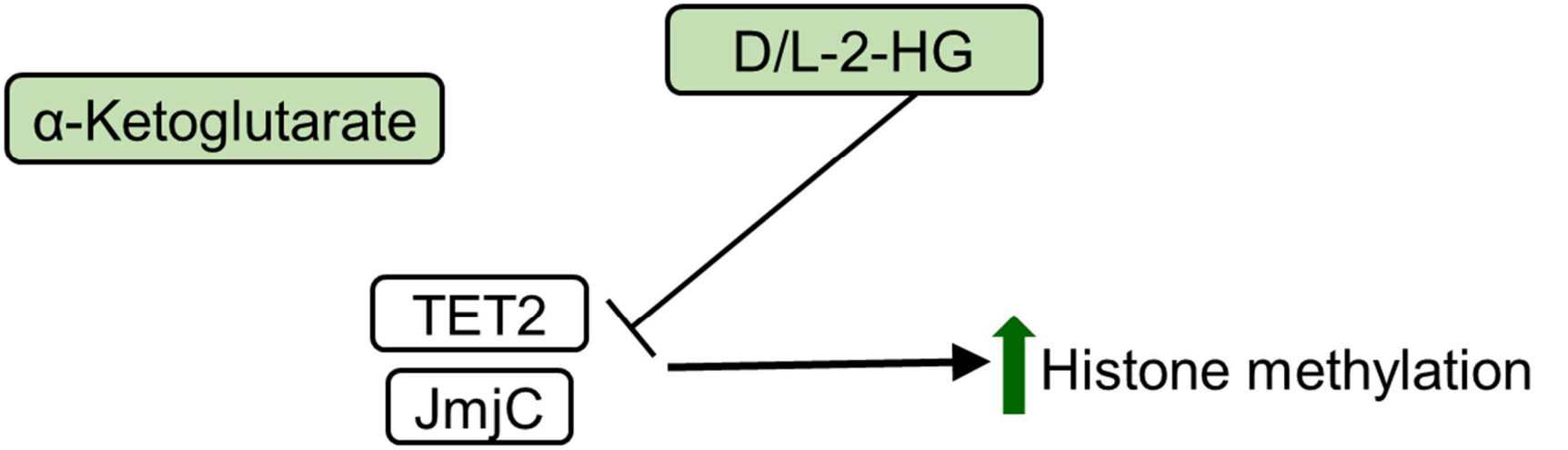

Figure 4.3 2-Hydroxyglutarate Can Impact Histone Methylation. Accumulated 2-hydroxyglutarate enantiomers act as a competitive inhibitor to α-ketoglutarate-dependent histone demethylases, including ten-eleven translocation 2 (TET2) and Jumonji-C (JmjC). This inhibition leads to increased histone methylation, potentially altering gene expression.

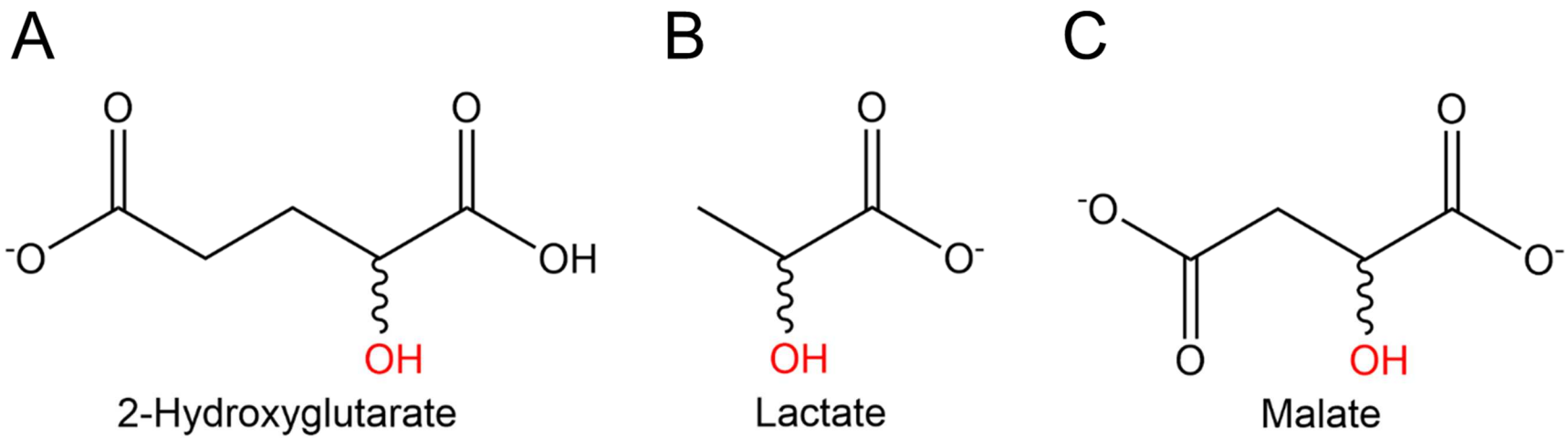

Figure 4.4 The Structure of 2-Hydroxyglutarate, Lactate, and Malate. The structure of 2-hydroxyglutarate (**A**), lactate (**B**), and malate (**C**), hydroxyl groups derivatized by DATAN are indicated in red.

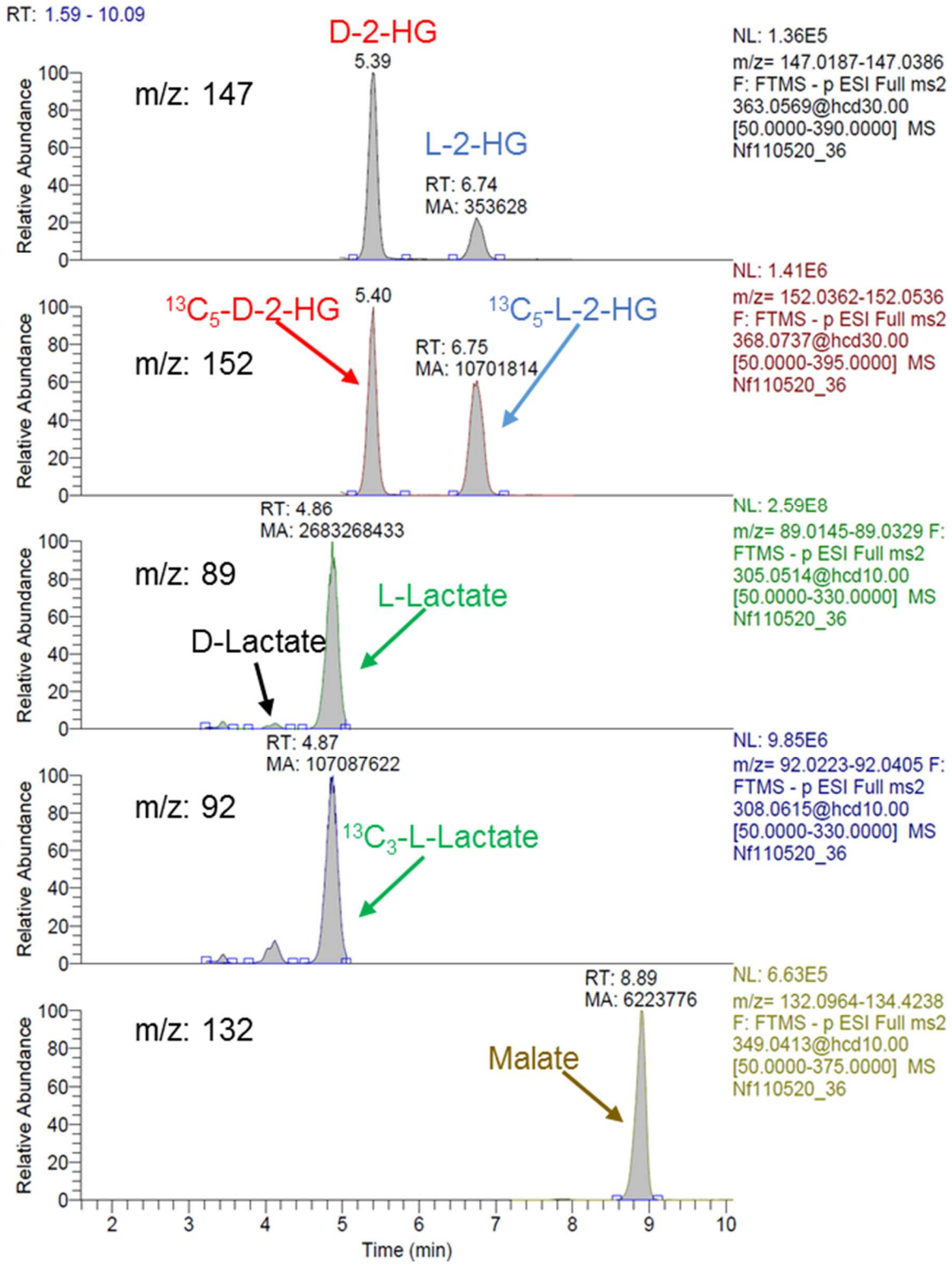

Figure 4.5 Extracted Ion Chromatograms for 2-HG Enantiomers, L-Lactate, and L- Malate. Metabolites were extracted from 50 µL WT serum in 80% methanol, dried, and derivatized for analysis by LC-MS for 2-HG and lactate enantiomers as described in Methods. The absorbance peaks were quantified for 2-HG, $^{13}C_5$-2-

HG internal standard, lactate, $^{13}C_3$-lactate internal standard, and malate. D-lactate was not detected in appreciable amounts in WT serum due to a low concentration *in vivo*. The product ion masses measured for each analyte are indicated (m/z values).

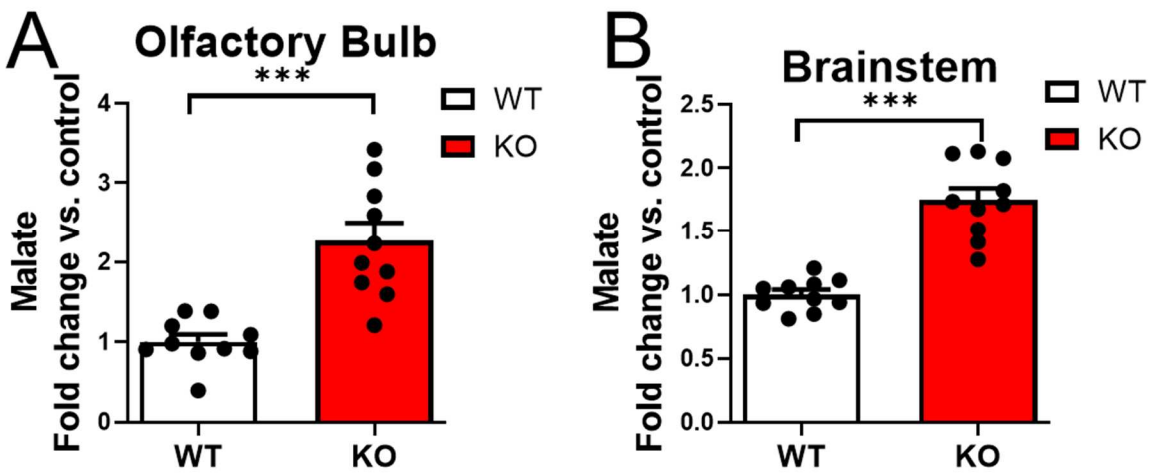

Figure 4.6 Malate Is Increased in NDUFS4 Knockout Mouse OB and BS. The metabolites of P53 WT and NDUFS4 KO mouse OB and BS tissues were extracted, derivatized, and analyzed by LC-MS to quantify metabolite enantiomers. **A-B**: The relative peak area ratio of malate was significantly increased in NDUFS4 KO mice in OB and BS tissues. Data are mean ± SE (***p < 0.001; unpaired t-test with Welch's correction) with n=10/group.

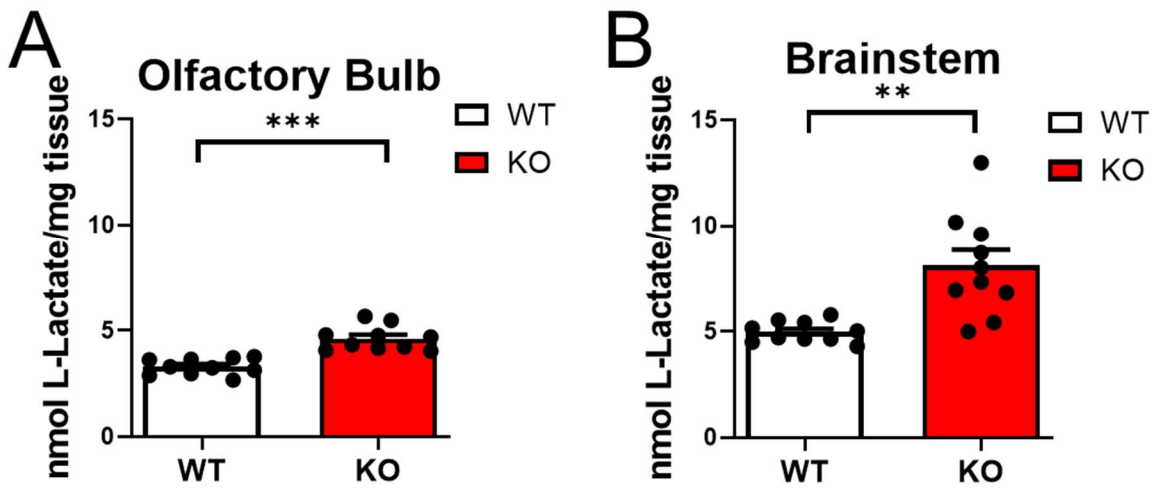

Figure 4.7 L-Lactate Is Increased in NDUFS4 Knockout Mouse OB and BS. The metabolites of P53 WT and NDUFS4 KO mouse OB and BS tissues were extracted, derivatized, and analyzed by LC-MS to quantify metabolite enantiomers. **A-B**: Knockout of NDUFS4 increased L-lactate 40% in OB (4.616 nmol/mg in KO versus 3.287 nmol/mg in WT) and 60% in the BS (8.09 nmol/mg in KO versus 4.96 nmol/mg in WT). Data are mean ± SE (**p < 0.01; ***p < 0.001; unpaired t-test with Welch's correction) with n=10/group.

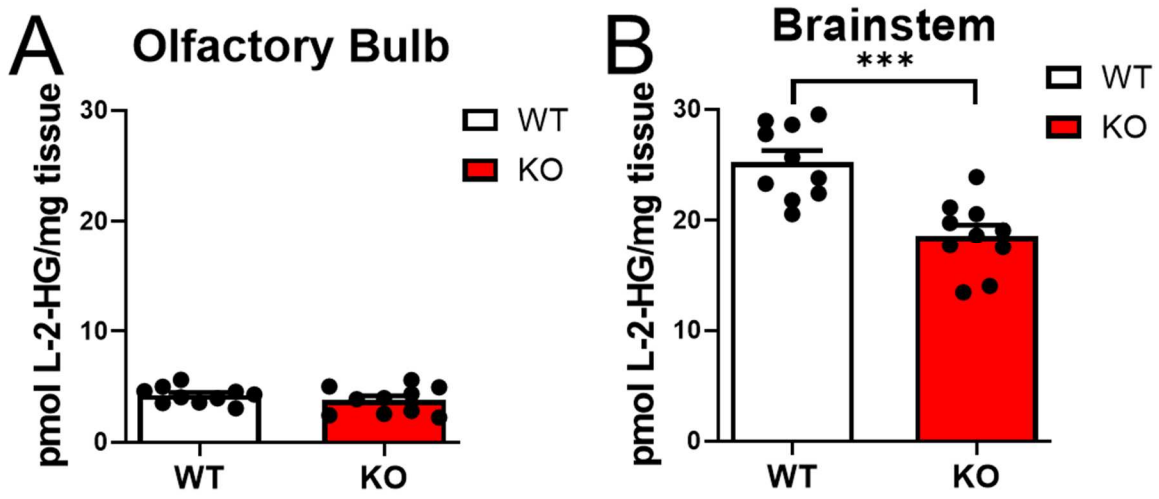

Figure 4.8 L-2-HG Is Decreased in NDUFS4 Knockout BS. P53 WT and NDUFS4 KO mouse OB and BS metabolites were extracted, derivatized, and analyzed by LC-MS to quantify metabolite enantiomers. **A-B**: While OB L-2-HG was unchanged with knockout of NDUFS4, NDUFS4 KO BS strikingly showed a 26% decrease in L-2-HG (18.566 pmol/mg in KO versus 25.245 pmol/mg in WT). Data are mean ± SE (***p < 0.001; unpaired t-test with Welch's correction) with n=10/group.

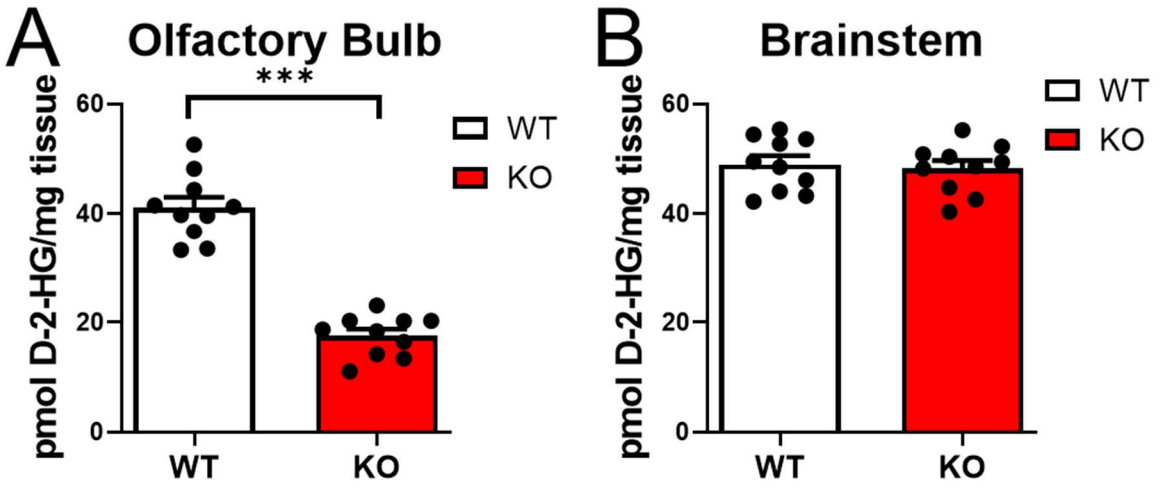

Figure 4.9 D-2-HG Is Decreased in NDUFS4 Knockout OB. P53 WT and NDUFS4 KO mouse OB and BS metabolites were extracted, derivatized, and analyzed by LC-MS to quantify metabolite enantiomers. **A-B**: NDUFS4 KO OB showed a 57% decrease in D-2-HG (17.607 pmol/mg in KO versus 41.053 pmol/mg in WT). However, brainstem levels of D-2-HG were unchanged with knockout of NDUFS4. Data are mean ± SE (***p < 0.001; unpaired t-test with Welch's correction) with n=10/group.

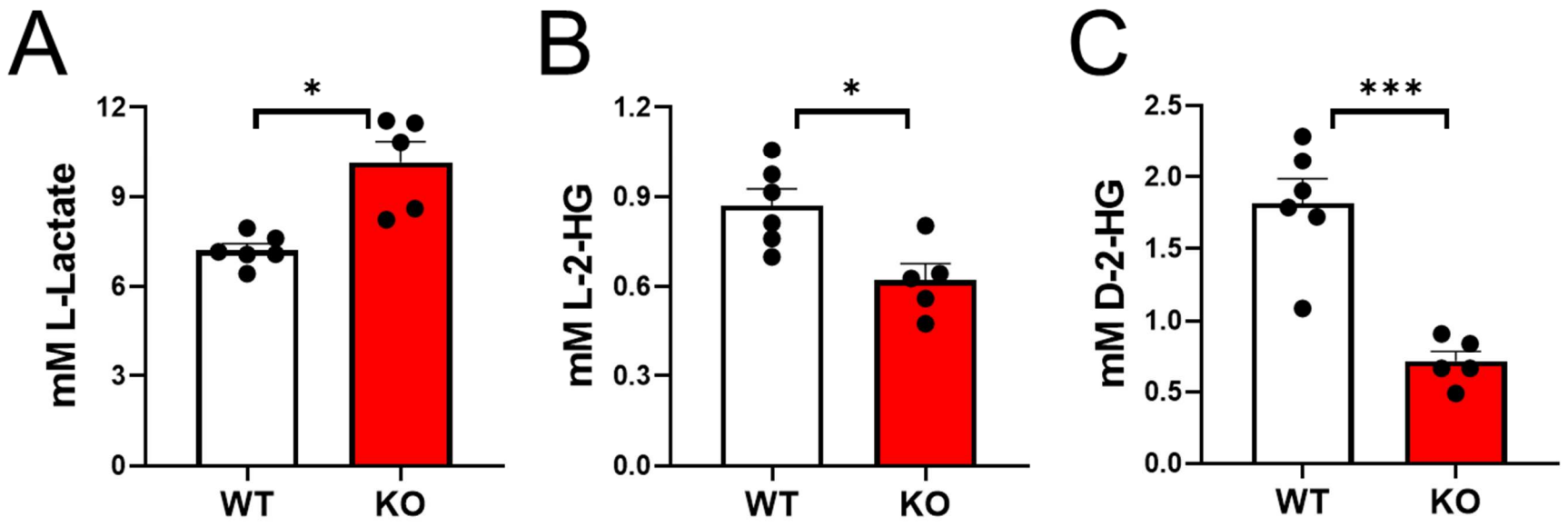

Figure 4.10 L-Lactate Is Increased and 2-HG Enantiomers Are Decreased in NDUFS4 Knockout Mouse Serum. The metabolites of 30 µL P49 WT and NDUFS4 KO mouse serum were extracted, derivatized, and analyzed by LC-MS to quantify metabolite enantiomers. **A-C**: Knockout of NDUFS4 increased L-Lactate by 40% and decreased L-2-HG by 28% and D-2-HG by 61% in the serum. Data are mean ± SE (*p < 0.05; ***p < 0.001; unpaired t-test with Welch's correction) with n=5-6/group.

CHAPTER 5

CONCLUSIONS

5.1 Overview

Our analysis of the inflammatory state of the NDUFS4 KO mouse confirmed that loss of NDUFS4 triggers the accumulation of microglia based on the expression of *Iba1*, *Trem2*, and *CD68* and increased IBA1 protein (**Figure 2.1, 2.2**). Previous reports have noted that the appearance of these microglia is activated and hypertrophic, versus quiescent ramified microglia found in these regions of the WT controls (Quintana et al., 2010). Despite the abundance of microglia, neither pro (*Il1b*, *Nlrp3*, Il6, *Tnfa*, *Il17*, *Irf3*, *Irf7*, *Il12*, *Arg1*) nor anti-inflammatory (*Hmox1*, *Irg1*, *Il10*) factors associated with select pathways were increased in the NDUFS4 KO olfactory bulb (**Figure 2.3, 2.4, 2.5, 2.6, 2.7**). In addition, NDUFS4 KO mouse olfactory bulbs do not accumulate the metabolites succinate or itaconate, whose increased abundance in parallel indicates a pro-inflammatory switch (**Figure 2.8**). This was surprising given the necrotizing lesion environment and sustained microgliosis in the NDUFS4 knockout OB, prompting further investigation of the impact of knockout of NDUFS4 on microglial and macrophage function.

Using a macrophage model of microglial metabolism, we discovered that knockout of NDUFS4 leads to an impaired glycolytic reserve, limited itaconate and succinate production, reduced expression and production of inflammatory factors, and decreased phagocytic activity (**Figure 2.10, 2.11, 2.12, 2.13, 2.14, 2.16**). The data suggests that the NDUFS4 KO microglia successfully migrate to the degenerating neurons and commit to phagocytosis but accumulate in these regions, sustaining the microgliosis. We speculate that these microglia may be 'exhausted' as they also lack NDUFS4 and may not be able to make sufficient ATP to support their metabolic needs, particularly the ATP-dependent lysosomal proton pump that is required for maximal cathepsin activity. While these cells are considered the 'neuroinflammatory' component of Leigh syndrome, it appears that they do not contribute to inflammatory cytokine production that further damages neurons. Rather, they are limited in their ability to respond to the neuronal death surrounding them.

To address the limited metabolism of the microglia, we sought to supplement the anti-inflammatory activity of itaconate using 4-octyl itaconate administration. We observed beneficial trends in gait, development of hindlimb curling, and body temperature, in addition to significantly slowing the NDUFS4 KO-induced decline in motor endurance in males (**Figure 3.5, 3.9**). Furthermore, increased PSD95, a neuronal synapse marker, was detected following 4OI treatment in the NDUFS4 KO cerebellum (**Figure 3.10**). While further study is needed to clarify the sex-specific effects of 4OI, these results indicate that early

treatment with exogenous itaconate may improve glial and neuronal function to better sustain healthy neurodevelopment.

A parallel study in our laboratory demonstrated inhibition of α-KGDH without accumulation of α-ketoglutarate in the NDUFS4 KO brain (Piroli et al., 2021). L-2-hydroxyglutarate is a metabolite enantiomer synthesized from α-ketoglutarate in acidic conditions, which is present in the NDUFS4 KO brain. While we detected increased L-lactate, as expected, L-2-hydroxyglutarate levels in addition to D-2-hydroxyglutarate levels were decreased in NDUFS4 KO mice (**Figure 4.7, 4.8, 4.9, 4.10**). These decreases highlight a potential metabolic target as 2-hydroxyglutarate can be used to replenish $FADH_2$ levels and sustain oxidative phosphorylation at Complex II, independent oxidative phosphorylation of the Complex I bioenergetic deficit.

5.2 Future Directions

The cytokine profiles analyzed offered a snapshot of the inflammatory network in NDUFS4 KO cells and tissues. However, to fully appreciate the specific nature of the microglia that are recruited to and retained in the lesions, we would perform single-cell transcriptomics. We appreciate that these cells may differ significantly from other microglia responding to pro-inflammatory stimuli, and determining the signature of these glia would further clarify if glial activation is secondary to, or driving, neuronal death. Further transcriptomic analyses of isolated NDUFS4 KO microglia in basal and LPS-stimulated conditions would

elucidate if they are capable of fully changing states in response to environmental cues.

We quantified impairments in phagocytic activity with knockout of NDUFS4, and an increase in lipid-rich microglia was observed in the NDUFS4 KO brain (Quintana et al., 2010). Therefore, investigation of NDUFS4 KO lysosomal function *in vitro* in basal and LPS-stimulated conditions using a pH-specific biosensor to quantify how knockout of NDUFS4 alters the function of the lysosomal vacuolar H^+ ATPase.

The anti-2SC antibody identified fumarate-modified and itaconate-modified proteins, which was unsurprising given the structural similarities between fumarate and itaconate-induced protein modifications. Therefore, it will be crucial to tailor LC-MS methods for the detection of free 2SC and 2,3 dicarboxypropylation. Given that the 2SC adduct is stable through 6 M hydrochloric acid hydrolysis at 100^{o}C, proper quantification of total protein levels of either fumarate or itaconate adducts could be measured post-hydrolysis (Nagai et al., 2007; Alderson et al., 2006). Well-characterized isotope standards will be required in line with our previous GC-MS methods for 2SC identification, considering that the mass adduct of fumarate is 116 compared to the 130 mass adduct of itaconate (Piroli et al., 2016). Therefore, we would use our antibody to detect proteins with a succinate moiety and follow this with mass spectrometry to quantify the specific adduct or identify the modified proteins in tissues and cells. These targets would provide a deeper understanding of how fumarate and itaconate-induced protein modifications alter the functional state in NDUFS4 KO mice.

As the mechanism behind the benefits of 4OI in NDUFS4 KO mice is unclear, an in-depth analysis of both the metabolome and transcriptome would broaden our understanding of the effects of 4OI. Therefore, we would treat WT and NDUFS4 KO mice with 4OI (100 mg/kg) IP injections once every 2 d for 14 d. Global proteomic and metabolomic analyses could be conducted on 4OI-treated WT and NDUFS4 KO mice in the OB and BS as the major sites of pathology. RNA-Seq analysis of these tissues would build on our qRT-PCR findings.

As Leigh syndrome patients are particularly vulnerable to infection and injury, supplementation with 4OI may enhance resistance to secondary infections. Therefore, we would assess the capacity of 4OI treatment to combat the LPS-stimulated pro-inflammatory responses *in vivo*. We would explore the benefits of pretreatment with 4OI in the initial response (2 h before 4 h 5 mg/kg LPS) and the peak of the LPS-stimulated inflammatory response (2 h before 18 h 5 mg/kg LPS). The inflammatory state of the serum and the olfactory bulb would be evaluated using standard ELISA kits for IL-1β and IL-10 for pro and anti-inflammatory cytokines.

The decrease in 2-hydroxyglutarate suggests that supplementation with α-ketoglutarate esters may provide therapeutic benefits. 2-hydroxyglutarate can be synthesized from α-ketoglutarate in the presence of lactic acidosis, and we predict that this would be rapidly utilized if 2-HG is providing electrons to Complex II via $FADH_2$ (Du et al., 2021). Administration of the α-ketoglutarate ester DMKG to WT and NDUFS4 KO mice would be performed prior to assessing motor behavior and measuring the effects on metabolite dynamics by LC-MS.

CHAPTER 6

MATERIALS AND METHODS

Materials. Unless otherwise noted, all chemicals were purchased from Sigma Aldrich (St. Louis, MO). Anti-2SC antibody was prepared by Eurogentec (Fremont, CA). Tween-20 and Criterion™ TGX™ Precast Gels were from Bio-Rad (Hercules, CA). Polyvinylidene fluoride (PVDF) was purchased from GE Healthcare (Fairfield, CT). L-glycine and sodium dodecyl sulfate (SDS) were purchased from Fisher Scientific (Waltham, MA).

Animals:

Animal care and use procedures were carried out by the guidelines of the National Institutes of Health Guide for the Care and Use of Laboratory Animals and approved by The University of South Carolina Animal Care and Use Committee. NDUFS4 KO heterozygous mice on a mixed 129/Sv:C57Bl/6 genetic background (Kruse et al., 2008: Quintana et al., 2010) were generously provided by Dr. Albert Quintana and Dr. Richard Palmiter (University of Washington, WA). The second exon of *Ndufs4* was excised from the germline using the *Mox2* promoter with Cre-Lox recombination to generate the systemic NDUFS4 KO mice. Vglut2 and Gad2 conditional NDUFS4 KO tissues were provided by Dr. Albert Quintana for use in the Frizzell laboratory. Breeding pairs were kept in the

University of South Carolina School of Medicine Department of Laboratory Animal Resources. Litters were ear punched to record offspring and weaned and genotyped at 21 d. Male and female mice were used to allow for sex-specific analyses where possible. Mice were sacrificed by isoflurane anesthesia and surgical decapitation. The olfactory bulb, brainstem, cerebellum, blood, and a lobe of the liver were removed, and the brainstem was bisected along the coronal axis for separate analyses. Tissues were incubated in RNAlater (Invitrogen AM7020) overnight for RNA analysis or snap-frozen in liquid nitrogen. Blood was collected and left to clot for 20 min at room temperature (RT) in 1.5 mL Eppendorf tubes. The tubes were centrifuged at 400 g and RT for 10 min. The serum supernatant was collected and snap-frozen in liquid nitrogen.

For the 16 d 4-octyl itaconate (4OI, ±50 mg/kg, HY-112675, MedChemExpress) treatment, P22 mice were habituated prior to baseline testing on the rotarod and an inclined balance beam prior to intraperitoneal injections in 40% β-cyclodextrin (MedChemExpress, HY-107201) (once every 3 d). Following this, the motor behaviors were again assessed at P40-41 prior to sacrifice and tissue collection. For the 14 d 4OI (100 mg/kg) treatment, P19 mice were habituated and given baseline testing in the rotarod and inclined balance beam behaviors before intraperitoneal injections in 40% β-cyclodextrin (every other day). Following this, the motor behaviors were again assessed at P35-36 prior to sacrifice and tissue collection (**Figure 3.2A-B**).

To test the benefits of 4OI treatment on survival, NDUFS4 KO mice were IP-injected at P27 with 100 mg/kg 4OI in 40% β-cyclodextrin once every 2 d for 45

d. Mice were weighed and scored on their development of NDUFS4 KO hindlimb curling from P27-71. The abdominal surface temperature was taken from P63-73, and gait was analyzed at P68. Mice were sacrificed at P74, and tissues were collected for analysis (**Figure 3.2C**). Further details are discussed below.

Rotarod:

Mice were habituated to the rotarod 3 d and the room for 1 h before testing. For testing, the rod was set to 4-40 rpm increase over 5 min. The weight, time till fall, and time spent spinning (where the mice hold the wheel as it spins instead of running) were recorded for 5 attempts with 30 min breaks in between. Time spent walking was calculated as time to fall – time spent spinning.

Inclined Balance Beam:

Mice were habituated to the inclined balance beam 3 d and the room for 1 h before testing. For testing, the mice were given 20 s in a black box with food and bedding at the end of the beam. Then, the mice were placed at the other end of a 1 m 4^{o} inclined beam with a 7 mm width. The weight, time to cross, and paw slips were recorded for 4 trials with 20 s inside the black box between trials. The best time of 3 trials was used for our analysis.

Surface Temperature:

Surface temperature readings were done similarly to Mei *et al.* though the abdominal region was ultimately used due to increased consistency (Mei et al., 2018). NDUFS4 KO mice were secured by scruffing. The abdominal temperature

was measured using a Braun No Touch 3-In-1 Digital Thermometer (Bruan, #BNT100US). Five temperature points were taken over a 15-second time frame, and the median temperature was recorded. Temperatures were recorded four times during the ages of P63-73.

Gait Analysis:

Gait analyses were conducted similarly to those described by Wertman *et al.* (Wertman et al., 2019). NDUFS4 KO mice were secured by scruffing, and their paws were painted distinct colors on the fore paws and hind paws of the mice with non-toxic, washable paint. Mice were placed in the gait chamber on one end of a 5.8 cm by 70.5 cm paper path opposite a covered portion and a food reward. The animal was allowed to freely walk down the chamber and were removed if they refused to walk or if they halted walking during the trial. Only mice who walked a minimum of half the length were used for data analysis. Right overlap was defined as the gait distance between the fore and hind paw prints on the right side of the mouse and was measured to determine the imbalance of the mouse.

Curling Assessment:

NDUFS4 KO mice were picked up by the tail for a maximum of 10 s. The presence of NDUFS4 KO-induced curling behaviors was measured, including trunk curling into a ball-shape or hind limb clasping.

Cell Culture:

Highly Aggressive Proliferating Immortalized (HAPI) cell culture: HAPI cells are a rat microglial cell line (Millipore, SCC103), were cultured in DMEM + 5% FBS + 1% Penicillin/Streptomycin. At ~80% confluence, cells were pretreated with ±62.5 μM 4-octyl itaconate and stimulated with ±100 ng - 5 μg/mL lipopolysaccharide (LPS, Invitrogen, 00-4976-03) for 18-24 h before the cells were collected for metabolite, protein, or RNA analysis. The cells were treated with a minimum of 100 ng/mL LPS as this dose is sufficient to stimulate a pro-inflammatory response in macrophages (Mills et al., 2018; Liao et al., 2019; Swain et al., 2020). Untreated cell lysates were incubated with ±10 mM itaconate after protein collection.

Peritoneal macrophage Isolation: P42 mice were injected with 1 mL 3% thioglycolate per 10 g of body weight into the peritoneal cavity 3 d before being sacrificed for the isolation of peritoneal macrophages. The cell suspension was centrifuged at 400 g for 10 min at 4 °C, and the supernatant was discarded. The pellet was resuspended in DMEM + 10% FBS + 1% Penicillin/Streptomycin and counted using a hemocytometer. Cells were cultured in DMEM + 10% FBS + 1% Penicillin/Streptomycin and treated with ±100 ng - 5 μg/mL lipopolysaccharide for 18-24 h before metabolite or protein collection.

Primary microglial Isolation: Microglia were isolated from P42 mice using the adult brain dissociation kit (Miltenyi Biotec, 130-107-677). Brainstem, olfactory bulb, and the remaining brain tissues were surgically isolated into ice-cold DPBS. The tissues were centrifuged for 10 min at 4 °C and 300 g before the supernatant was discarded. The tissues were incubated in 1 mL Enzyme mix 1 and 2 at 37 °C

for ~25 min. During incubation, tissues were dissociated using fire-polished glass pipettes. The cell suspension was strained through a 70-µm cell strainer and washed with 5 mL DPBS + 0.5% BSA. The suspension was centrifuged for 10 min at room temperature (RT) and 300 g before the supernatant was discarded. The suspension was incubated in 2 mL ice-cold Debris buffer and overlaid gently with 2 mL ice-cold DPBS. The tubes were centrifuged for 10 min at 4 °C and 3000 g before the top 2 phases were discarded. The suspension was washed with 8 mL ice-cold DPBS and centrifuged for 10 min at 4 °C and 3000 g before the supernatant was discarded. 0.5 mL of RBC removal solution was added. The suspension was incubated at 4 °C for 10 min. 5 mL DPBS + 2 mM EDTA or 0.5% BSA was added. The dissociated suspension was centrifuged for 10 min at 4 °C and 300 g before the supernatant was discarded.

CD11+ microglia were isolated using the EasySep™ mouse CD11b positive selection kit II (Stemcell, 18970A). The dissociated cell suspension was incubated in 50 µL/mL selection cocktail for 5 min at RT. 80 µL/mL RapidSpheres™ were added, and the suspension was incubated at RT for 5 min. The suspension volume was increased to 2.5 mL with PBS + 2 mM ethylenediaminetetraacetic acid (EDTA). The LS column (Miltenyi Biotec, 130-042-401) was placed in the MidiMACS separation magnet (Miltenyi Biotec, 130-042-302) and rinsed with 2 mL PBS + 2 mM EDTA. The cell suspension was pipetted into the magnetized column. The magnetized column was washed 2X with 2 mL PBS + 2 mM EDTA. The flow-through was collected and centrifuged for 5 min at 4 °C and 1400 g before the supernatant was discarded. The CD11- cell pellet was saved for protein collection.

The column was removed from the separation magnet and rinsed with 2 mL PBS + 2 mM EDTA using the associated plunger to isolate the CD11+ cell suspension. The CD11+ cell suspension was centrifuged for 5 min at 4 °C and 1400 g before the supernatant was discarded. The CD11+ cell pellet was saved for protein collection.

In addition, enriched microglia were isolated using a Percoll gradient. The dissociated cell suspension was centrifuged for 10 min at 4 °C and 250 g. The supernatant was discarded. The cell pellet was resuspended in 4 mL HBSS with 37% Percoll and transferred to a 15 mL conical tube. 4 mL HBSS with 70% Percoll was gently underlaid on the bottom, and 4 mL HBSS with 30% Percoll was gently added at the top. 2 mL HBSS was gently added at the top, and the tubes were centrifuged for 40 min at RT and 300 g with no brake. The microglial interphase between the 70% and 37% Percoll layers was isolated. 6 mL HBSS was added to the enriched interphase. The interphase was centrifuged for 7 min at 4 °C and 500 g. The supernatant was discarded. The pellet was washed briefly through centrifugation 3X in 500 µL HBSS at 800 g and 4 °C. Enriched cells were resuspended in DMEM + 10% FBS+ 1% Penicillin/Streptomycin, counted through a hemocytometer, and plated. Cells were cultured for 14 d before treatment with ±100 ng - 5 µg/mL lipopolysaccharide for 24 h and protein collection.

Polyacrylamide Gel Electrophoresis and Immunoblotting:

For protein collection, cell culture plates were washed 3X with DPBS. Cells and tissues were harvested in radioimmunoprecipitation assay (RIPA+) lysis buffer

(50 mM Tris-HCl + 150 mM NaCl + 1 mM ethylenediaminetetraacetic acid + 0.1% Triton X-100 + 0.1% SDS + 0.5% sodium deoxycholate, pH 7.4), with the addition of 2 mM diethylenetriaminepentaacetic acid and a protease inhibitor mixture (P8340, Sigma/Aldrich). Homogenization was performed by pulse sonication at 2 watts using a Model 100 sonic dismembrator (Fisher Scientific, Fair Lawn, NJ) for 5-30 s before quantification by the Lowry assay.

For sodium dodecyl sulfate-polyacrylamide gel electrophoresis (SDS-PAGE), 15-40 µg of cell or tissue lysate were incubated with 4X Laemmli loading buffer in 95 °C for 15 min. The lysates were centrifuged briefly and loaded on 12% gels. The gels were run at 100 V for ~55 min in running buffer (25 mM Tris + 200 mM Glycine + 0.1% SDS) and washed in transfer buffer (25 mM Tris + 200 mM Glycine + 0.07% Tween-20) for 15 min at RT. The protein was transferred to a PVDF membrane under 250 mA for 100 min at 4 °C in transfer buffer. Equal protein loading was verified via Ponceau Red staining for 1 min at RT. Membranes were washed 3X for 5 min at RT in wash buffer (pH 7.4, 20 mM Tris + 20% Methanol) and blocked in 5% milk for 1 h at RT or overnight at 4 °C. Membranes were incubated in primary and secondary antibodies for 1 h at RT or overnight at 4 °C in 2% milk with 3 5 min washes in wash buffer after each antibody. Membranes were probed with 1:1000 anti-Iba1 antibody (Invitrogen, PA5-21274) and 1:8000 goat anti-rabbit horseradish peroxidase-labeled secondary antibody (Cell Signaling, 7074S); 1:6000 Frizzell laboratory anti-2SC/succinate moieties antibody and 1:4000 anti-rabbit antibody; 1:2000 Discovery anti-2SC/succinate moieties antibody (Discovery Antibodies, crb2005017d) and 1:5000 anti-rabbit antibody;

1:2000 anti-heme oxygenase-1 antibody (Enzo Life Sciences, ADI-SPA-896-F) and 1:8000 anti-rabbit antibody; 1:6000 anti-IL-1β antibody (Cell Signaling, D3H1Z) and 1:12000 anti-rabbit antibody; 1:8000 anti-β3-tubulin antibody (Cell Signaling, D65A4) and 1:16000 anti-rabbit antibody; 1:15000 anti-PSD95 antibody (Biorad, VMA00479) and 1:30,000 mouse anti-goat horseradish peroxidase-labeled secondary antibody (Santa Cruz, sc-2354); or 1:8000 anti-actin antibody (Santa Cruz, sc-1616) and 1:16,000 anti-mouse antibody The membranes were imaged on photographic film after 5 min at RT in enhanced chemiluminescent (ECL) solution (Thermo Scientific, 80196). Membranes were stripped in preheated stripping buffer (pH 6.8, 62.5 mM Tris + 2% SDS + 0.7% β-mercaptoethanol) at 65 °C for 5-20 min. Stripped membranes were washed 3X for 5 min in wash buffer before blocking in milk for future immunodetection. Membranes were normalized through incubation in Coomassie staining for 5 min at RT, washed 2X for 1 h in 7% acetic acid + 10% methanol, and dried at RT. Image J software (NIH) was used to quantify band intensity through densitometry.

RNA Isolation:

RNA was isolated per the manufactures instructions using the RNeasy+ Mini Kit (Qiagen). Briefly, ~20 µg of brain tissue or ~2.5 x 10^6 cells were homogenized and added to the spin column. Suspensions were washed, and RNA was eluted in 30 µL RNase-free H_2O. RNA density (µg/mL) and purity were determined via Nanodrop.

Quantitative Real-Time PCR (qRT-PCR):

The RNA was normalized according to total RNA yield quantified using a Biophotometer plus (Eppendorf). 0.2 mL polymerase chain reaction (PCR) tubes were filled with 1 µg of RNA + 4 µL 5X qScript cDNA SuperMix (Quantabio 95048) + RNase-free H_2O to 20 µL. The tubes were treated for 5 min at 25 °C, 30 min at 42 °C, and 5 min at 85 °C in a Mastercycler (Eppendorf) to form the cDNA. Real-time PCR was performed using an iCycler IQ (BioRad) with 10 µL PerfeCTa SYBR Green FastMix (Quantabio, 95072) + 4 µL cDNA + 1 µL 50 µM forward and reverse primer stock and filled to 20 µL with RNase free H_2O in a 96 well PCR plate (**Table M.1**). Plates were covered with clear adhesive film and run through 1 cycle of 3 min at 95 °C and 40 cycles of 15 s at 95 °C and 1 min at 60 °C. The $2^{-\Delta\Delta Ct}$ values used the levels of *Rbs18* or *Iba1* mRNA to normalize the results where indicated. Results were plotted in fold change to WT control. Primers are listed in Table 1.

Cellular Metabolism Analysis:

XF24 seahorse plates (Agilent, 100777-004) were plated with peritoneal macrophages (30,000 cells/well except for the background wells) to conduct real-time analyses of oxidative phosphorylation and glycolysis. After growing overnight in DMEM + 10% FBS + 1% Penicillin/Streptomycin at 5% CO_2 and 37 °C in a cell incubator, the cells were exposed to $\pm$100 ng/mL LPS for 1 h. For oxidative phosphorylation and glycolysis stress tests, plates were washed with XFAB pH 7.4 or XF base medium pH 7.4, respectively. The cells were cultured without CO_2 for 1 h in XFAB + 25 mM Glucose + 10 mM Pyruvate pH 7.4 or XF Base Medium pH 7.4 respectively and loaded into the Agilent XF24 Extracellular Flux Analyzer. 3 cycles of 3 min mix, 2 min wait, and 3 min measure were conducted. For oxidative

phosphorylation, the OCR was monitored under basal conditions and in response to oligomycin (10 μM), FCCP (2 μM), and rotenone/antimycin (30 μM and 40 μM respectively). Basal respiration (the baseline group average - the post-rotenone/antimycin injection group average) and ATP production (the baseline group average - the post-oligomycin injection group average) were calculated. For glycolysis, the ECAR was monitored in macrophages under basal conditions and in response to glucose (10 mM), oligomycin (1 μM), and 2-deoxyglucose (50 mM). Glycolysis (the post-glucose injection group average - the post-2-deoxyglucose injection group average) and glycolytic reserve (the post-oligomycin injection group average - the post-glucose injection group average) were calculated. Plates were washed 3X with PBS, and cells were fragmented in 50 uL 100 mM NaOH. All data obtained were normalized to total protein content with a Lowry assay.

Phagocytic Activity Analysis:

WT and NDUFS4 KO macrophages were plated on 22 mm by 22 mm glass coverslips and cultured in DMEM + 10% FBS+ 1% Penicillin/Streptomycin. Cells were stimulated for 18 h with ±100 ng/mL LPS and 3 h with 1:500 1 μm mean particle size fluorescently labeled latex beads (Sigma Aldrich, L4655). Slides were washed 3X in PBS and fixed at 37 °C in 4% paraformaldehyde for 20 min. The fixed slips were washed 3X in PBS for 5 min at RT. The cells were permeabilized with 0.25% Triton in PBS for 15 min at RT on a shaker and rinsed in PBS. The coverslips were incubated in 5 μg/mL DAPI stain for 5 min at RT. The coverslips were rinsed in PBS and mounted on glass slides with Prolong Diamond Antifade Mountant (LifeTechnologies, P36965). The interface was sealed with nail polish,

and the slides were dried overnight in the dark at RT. The dried slides were stored at 4 °C without light until imaging. Slides were imaged with Neurolucida software, and fluorescence was quantified using ImageJ.

Metabolite Analysis:

The snap-frozen tissues were dissociated on ice through pre-cooled glass-Teflon homogenizers in 600 µL 2:1 chloroform: methanol and transferred to 1.5 mL Eppendorf tubes. The tubes were briefly pulse-sonicated. Cells were lysed in 200 µL methanol and collected using a rubber policeman into 1.5 mL Eppendorf tubes. 400 µL chloroform was added. Both cell and tissue tubes were given 200 µL LC-MS grade H_2O and the respective internal standards, including a succinate $^{13}C_4$ internal standard (CLM-1571, Cambridge Isotope Laboratories); or a lactate $^{13}C_3$ internal standard (CLM 1579, Cambridge Isotope Laboratories); and a fumarate $^{13}C_4$ internal standard (CLM-1529, Cambridge Isotope Laboratories). Tubes were centrifuged at 3220 g and 4 °C for 20 min. The upper metabolite layer was transferred to a new 1.5 mL Eppendorf tube and dried by centrifugal evaporation. The chloroform layer was discarded. The protein was dried and resuspended in RIPA+ buffer for protein quantification by the Lowry assay. The standards were prepared in 80% methanol with their respective internal standards and a 100 µM malate carrier and dried by centrifugal evaporation.

The quantification of TCA cycle intermediates was performed by GC-MS at the David H. Murdock Research Institute (DHMRI, Kannapolis, NC) for OB tissues and HAPI cells. Analysis of polar TCA metabolites from macrophages was

performed by LC-MS at the University of South Carolina Mass Spectrometry Center. Both methods are described below.

The quantification of lactate and 2-hydroxyglutarate enantiomers for WT and NDUFS4 KO OB and serum was performed by LC-MS at the University of South Carolina Mass Spectrometry Center after metabolite extraction and derivatization. 80% final methanol + 50 µM final lactate $^{13}C_3$ internal standard (CLM 1579, Cambridge Isotope laboratories) + 5 µM final 2-hydroxyglutarate $^{13}C_5$ internal standard (CLM-10351, Cambridge Isotope laboratories) were added to 30-50 µL serum in 1.5 mL Eppendorf tubes. Serum tubes were centrifuged at 3220 g and 4 °C for 20 min. The upper metabolite layer was transferred to a new 1.5 mL Eppendorf tube. The protein pellet was dried for future analyses. Olfactory bulb metabolites were extracted in 2:1 chloroform: methanol with 50 µM final lactate $^{13}C_3$ internal standard + 5 µM final 2-hydroxyglutarate $^{13}C_5$ internal standard into 1.5 mL Eppendorf tubes. Lactate and 2-hydroxyglutarate standard curves were prepared in parallel with their respective internal standards and 100 µM malate carrier. The metabolites and standards were dried by centrifugal evaporation and derivatized with 50 µL 50 mg/mL DATAN in 4:1 acetonitrile: acetic acid at 70^{o}C for 2 h in a water bath incubator. Tubes were cooled to RT and centrifuged briefly before 50 µL 4:1 acetonitrile: acetic acid was added to dilute for LC-MS analysis by the University of South Carolina Mass Spectrometry Center.

Before the derivatization of OB tissues and HAPI cells for GC-MS, the extracts were resuspended in ethyl acetate, transferred to GC-MS vials, and dried with N_2. The extracts were derivatized with 200 µL methylamine (20 mg/mL in

pyridine) at 30 °C for 90 min, followed by drying under N_2. This was followed by the addition of 120 µL N-methyl-N-(trimethylsilyl) trifluoroacetamide (MSTFA) with 1% trimethylchlorosilane (TMCS); the mixture was incubated at 70 °C for 60 min. The derivatized product was stored in a -20 °C freezer for one hour before GC/MS analysis. An Agilent 7890A GC system, coupled to an Agilent 5975C electron ionization (EI) mass selective detector (MSD), was used to analyze the TMS-derivatized products. Select ion monitoring (SIM) was performed, and the peak areas obtained were normalized to the internal standards. Absolute quantification for all metabolites was performed based on standard curves obtained from the normalized reference standards using Xcalibur (Thermo Scientific), and the final metabolite concentrations were normalized to tissue weights, serum volume, or total protein content.

For LC-MS, samples were vortexed and transferred to LC vials for analysis. LC separation was performed on a Thermo Vanquish Flex liquid chromatograph using a PEEK coated SeQuant ZIC HILIC column (Merck Millipore). The column was 2.1 mm x 150 mm with 3.5 µm particles and was preceded by an equivalent 20 mm long guard column. 1 µl of the sample was separated by isocratic elution with 15% mobile phase A (10% 200 mM formic acid:90% LC-MS grade water) and 85% mobile phase B (10% 200 mM formic acid:90% acetonitrile) at a total flow rate of 200 µl/min. The formic acid was titrated to pH 3.25 with ammonium hydroxide. Negative ion electrospray mass spectra were acquired on a Thermo Q-Exactive HF-X quadrupole-Orbitrap in MS/MS mode with the Orbitrap resolution set at 7,500. Precursor ions (305 or 308 Da) were isolated by the quadrupoles and

fragmented in the HCD cell at 10 eV. The product ions were mass analyzed in the Orbitrap. XCalibur 4.3 software was used to construct chromatograms of the transitions 305>89 (lactate) and 308>92 (L-lactate-$^{13}C_3$). The transitions 363>147 and 368>152 were monitored for unlabeled 2-hydroxyglutarate and $^{13}C_5$ 2-hydroxyglutarate, and the transition 349>132 was used for L-malate. The areas of the lactate and 2-hydroxyglutarate peaks were normalized to the areas of their ^{13}C internal standard and tissue weight.

Data Analysis:

The number of biological replicates used varies across experiments and is indicated in the legends after the Grubbs' test was used to identify statistical outliers. Cell culture experiments used a minimum of 3 (range 3-8) biological replicates per group and animal experiments used an average of 6 (range 3-10) biological replicates per group depending on if there were sufficient numbers for sex-specific analyses. Data are summarized as mean $\pm$ standard error and analyzed and graphed using Prism 9 (Graphpad Software, San Diego, California). Welch's t-test compared data between two groups, the repeated measures ANOVA compared data across timepoints, and the two-way ANOVA with Tukey's multiple comparisons test compared data between more than two groups. In all analyses, $p < 0.05$ was considered statistically significant.

Primer	Forward	Reverse
Arg1	ACC TGG CCT TTG TTG ATG TCC CTA	AGA GAT GCT TCC AAC TGC CAG ACT
Cathepsin B	GTG GAG GTG TCT GCT GAA G	GGG AGG GAT GGT GTA TGG TAA
Cathepsin D	AGG ACA CTG TAT CGG TTC CAT	TGT TCA GGT AGA AGG AGA AGA TGT T
CD68	ACT TCG GGC CAT GTT TCT CT	GCT GGT AGG TTG ATT GTC GT
Hmox1	GAG CAG AAC CAG CCT GAA CT	CTC GGC TTG GAT GTG TAC CT
Iba1	GGA TTT GCA GGG AGG AAA A	TGG GAT CAT CGA GGA ATT G
Il10	AGG CGC TGT CAT CGA TTT	CAC CTT GGT CTT GGA GCT TAT
Il12	CGA AAC CTG CTG AAG ACC AC	AGC TCC CTC TTG TTG TGG AA
Il17	CCT TCA CTT TCA GGG TCG AG	CAG TTT GGG ACC CCT TTA CA
Il1b	CCT GCA GCT GGA GAG TGT GGA T	TGT GCT CTG CTT GTG AGG TGC T
Il6	AGA CAA AGC CAG AGT CCT TCA G	TGC CGA GTA GAT CTC AAA GTG A
Irf3	GGA AAT ATC TGA GCC CCA CT	CAG CTC TGG ACC TGT CTT GT
Irf7	GAA GAC CCT GAT CCT GGT GA	CCA GGT CCA TGA GGA AGT GT
Irg1	TAT GCC AAC TAC TCC CCC GA	CGG GAA GCT CTT AAA GGC CA
Nlrp3	TGC TCT TCA CTG CTA TCA AGC CCT	ACA AGC CTT TGC TCC AGA CCC TAT
Rbs18	GGA TGT GAA GGA TGG GAA GT	CCC TCT ATG GGC TCG AAT TT
Tnfa	GCC TCT TCT CAT TCC TGC TT	TGG GAA CTT CTC ATC CCT TTG
Trem2	CTG GAA CCG TCA CCA TCA CTC	CGA AAC TCG ATG ACT CCT CGG

Table 6.1: Primer list for real-time PCR.

REFERENCES

Adam, J., Yang, M., Soga, T., & Pollard, P.J. (2014). Rare insights into cancer biology. *Oncogene*, 33(20), 2547-56. doi: 10.1038/onc.2013.222.

Adjobo-Hermans, M.J.W., de Haas, R., Willems, P.H.G.M., Wojtala, A., van Emst-de Vries, S.E., Wagenaars, J.A., van den Brand, M., Rodenburg, R.J., Smeitink, J.A.M., Nijtmans, L.G., Sazanov, L.A., Wieckowski, M.R., & Koopman, W.J.H. (2020). NDUFS4 deletion triggers loss of NDUFA12 in Ndufs4−/− mice and Leigh syndrome patients: A stabilizing role for NDUFAF2. *BBA Bioenergetics*, 1861(8), 148213

Alderson, N.L., Wang, Y., Blatnik, M., Frizzell, N., Walla, M.D., Lyons, T.J., Alt, N., Carson, J.A., Nagai, R., Thorpe, S.R., & Baynes, J.W. (2006). S-(2-Succinyl)cysteine: a novel chemical modification of tissue proteins by a Krebs cycle intermediate. *Arch Biochem Biophys*, 450, 1-8

Amici, S.A., Dong, J., & Geurau-de-Arellano, M. (2017). Molecular Mechanisms Modulating the Phenotype of Macrophages and Microglia. *Front. Immunol*, 10. https://doi.org/10.3389/fimmu.2017.01520

Angelaki, D. E., & Cullen, K. E. (2008). Vestibular system: the many facets of a multimodal sense. *Annu Rev Neurosci*, 31, 125-50. doi: 10.1146/annurev.neuro.31.060407.125555.

Äyräväinen, A., Pasanen, A., Ahvenainen, T., Heikkinen, T., Pakarinen, P., Härkki, P., & Vahteristo, P. (2020). Systematic molecular and clinical analysis of

uterine leiomyomas from fertile-aged women undergoing myomectomy. *Hum Reprod*, 35(10), 2237-2244. doi: 10.1093/humrep/deaa187.

Bajwa, E., Pointer, C.B., & Klegeris, A. (2019). The Role of Mitochondrial Damage-Associated Molecular Patterns in Chronic Neuroinflammation. *Mediators of Inflammation*, 4050796. https://doi.org/10.1155/2019/4050796

Bak, D.W., Bechtel, T.J., Falco, J.A., & Weerapana, E. (2019). Cysteine reactivity across the subcellular universe. *Current Opinion in Chemical Biology,* 48, 96–105. https://doi.org/10.1016/j.cbpa.2018.11.002

Bakare, A.B., Lesnefsky, E.J., & Iyer, S. (2021). Leigh Syndrome: A Tale of Two Genomes. *Frontiers in Physiology*, 12, 693734. https://doi.org/10.3389/fphys.2021.693734

Bambouskova, M., Gorvel, L., Lampropoulou, V., Sergushichev, A., Loginicheva, E., Johnson. K., Korenfeld, D., Mathyer, M.E., Kim, H., Huang, L.H., Duncan, D., Bregman, H., Keskin, A., Santeford, A., Apte, R.S., Sehgal, R., Johnson, B., Amarasinghe, G.K., Soares, M.P., Satoh, T., Akira, S., Hai, T., Strong, C.G., Auclair, K., Roddy, T.P., Biller, S.A., Jovanovic, M., Klechevsky, E., Stewart, K.M., Randolph, G.J., & Artyomov, M.N. (2018). Electrophilic properties of itaconate and derivatives regulate the IκBζ–ATF3 inflammatory axis. *Nature*, 556(7702), 501-504

Becker-Kettern, J., Paczia, N., Conrotte, J.F., Kay, D.P., Guignard, C., Jung, P.P., & Linster, C.L. (2016). Saccharomyces cerevisiae Forms D-2-Hydroxyglutarate and Couples Its Degradation to D-Lactate Formation via

a Cytosolic Transhydrogenase. *The Journal of Biological Chemistry*, 291(12), 6036–6058. https://doi.org/10.1074/jbc.M115.704494

Bhatia, K. D., Krishnan, P., Kortman, H., Klostranec, J., & Krings, T. (2020). Acute Cortical Lesions in MELAS Syndrome: Anatomic Distribution, Symmetry, and Evolution. *AJNR Am J Neuroradiol*, 41(1), 167-173. doi: 10.3174/ajnr.A6325.

Bilbo, S. D., Block, C. L., Bolton, J. L., Hanamsagar, R., & Tran, P. K. (2018). Beyond infection - Maternal immune activation by environmental factors, microglial development, and relevance for autism spectrum disorders. *Experimental Neurology*, 299(Pt A), 241–251. https://doi.org/10.1016/j.expneurol.2017.07.002

Bizzoco, E., Faussone-Pellegrini, M. S., & Vannucchi, M. G. (2007). Activated microglia cells express argininosuccinate synthetase and argininosuccinate lyase in the rat brain after transient ischemia. *Exp Neurol,* 208(1), 100-9. doi: 10.1016/j.expneurol.2007.07.018.

Blatnik, M., Frizzell, N., Thorpe, S.R., & Baynes, J. W. (2008A). Inactivation of glyceraldehyde-3-phosphate dehydrogenase by fumarate in diabetes: formation of S-(2-succinyl)cysteine, a novel chemical modification of protein and possible biomarker of mitochondrial stress. *Diabetes*, 57(1), 41–49. https://doi.org/10.2337/db07-0838

Blatnik, M., Thorpe, S.R., & Baynes, J. W. (2008B). Succination of proteins by fumarate: mechanism of inactivation of glyceraldehyde-3-phosphate

dehydrogenase in diabetes. *Annals of the New York Academy of Sciences*, 1126, 272–275. https://doi.org/10.1196/annals.1433.047

Blewett, M. M., Xie, J., Zaro, B. W., Backus, K. M., Altman, A., Teijaro, J. R., & Cravatt, B. F. (2016). Chemical proteomic map of dimethyl fumarate-sensitive cysteines in primary human T cells. *Science Signaling,* 9:rs10. doi:10.1126/scisignal.aaf7694

Bolea, I., Gella, A., Sanz, E., Prada-Dacasa, P., Menardy, F., Bard, A.M., Machuca-Márquez, P., Eraso-Pichot, A., Mòdol-Caballero, G., Navarro, X., Kalume, F., & Quintana, A. (2019). Defined neuronal populations drive fatal phenotype in a mouse model of Leigh syndrome. *eLife*, 8, e47163. https://doi.org/10.7554/eLife.47163

Bongaerts, G., Tolboom, J., Naber, T., Bakkeren, J., Severijnen, R., & Willems, H. (1995). D-lactic acidemia and aciduria in pediatric and adult patients with short bowel syndrome. *Clin Chem,* 41, 107-110

Bunse, L., Pusch, S., Bunse, T., Sahm, F., Sanghvi, K., Friedrich, M., Alansary, D., Sonner, J. K., Green, E., Deumelandt, K., Kilian, M., Neftel, C., Uhlig, S., Kessler, T., von Landenberg, A., Berghoff, A. S., Marsh, K., Steadman, M., Zhu, D., Nicolay, B., Wiestler, B., Breckwoldt, M. O., Al-Ali, R., Karcher-Bausch, S., Bozza, M., Oezen, I., Kramer, M., Meyer, J., Habel, A., Eisel, J., Poschet, G., Weller, M., Preusser, M., Nadji-Ohl, M., Thon, N., Burger, M.C., Harter, P.N., Ratliff, M., Harbottle, R., Benner, A., Schrimpf, D., Okun, J., Herold-Mende, C., Turcan, S., Kaulfuss, S., Hess-Stumpp, H., Bieback, K., Cahill, D. P., Plate, K. H., Hänggi, D., Dorsch, M., Suvà, M. L., Niemeyer,

B. A., von Deimling, A., Wick, W., & Platten, M. (2018). Suppression of antitumor T cell immunity by the oncometabolite (R)-2-hydroxyglutarate. *Nat Med*, 24(8), 1192-1203. doi: 10.1038/s41591-018-0095-6.

Burgener, A. V., Bantug, G. R., Meyer, B. J., Higgins, R., Ghosh, A., Bignucolo, O., Ma, E. H., Loeliger, J., Unterstab, G., Geigges, M., Steiner, R., Enamorado, M., Ivanek, R., Hunziker, D., Schmidt, A., Müller-Durovic, B., Grählert, J., Epple, R., Dimeloe, S., Lötscher, J., Sauder, U., Ebnöther, M., Burger, B., Heijnen, I., Martínez-Cano, S., Cantoni, N., Brücker, R., Kahlert, C. R., Sancho, D., Jones, R. G., Navarini, A., Recher, M., & Hess, C. (2019). SDHA gain-of-function engages inflammatory mitochondrial retrograde signaling via KEAP1-Nrf2. *Nat Immunol,* 20(10), 1311-1321. doi: 10.1038/s41590-019-0482-2.

Calvaruso, M. A., Willems, P., van den Brand, M., Valsecchi, F., Kruse, S., Palmiter, R., Smeitink, J., & Nijtmans, L. (2012). Mitochondrial complex III stabilizes complex I in the absence of NDUFS4 to provide partial activity, *Human Molecular Genetics*, 21(1), 115–120

Casey, R. T., McLean, M. A., Challis, B. G., McVeigh, T. P., Warren, A. Y., Mendil, L., Houghton, R., De Sanctis, S., Kosmoliaptsis, V., Sandford, R. N., Gallagher, F. A., & Maher, E. R. (2020). Fumarate Metabolic Signature for the Detection of Reed Syndrome in Humans. *Clin Cancer Res*, 226(2), 391-396. doi: 10.1158/1078-0432.CCR-19-1729.

Cavanagh, J. B. & Harding, B. N. (1994). Pathogenic factors underlying the lesions in Leigh's disease. Tissue responses to cellular energy deprivation and their clinico-pathological consequences. *Brain*, 117, 1357 – 76

Cheepsunthorn, P., Radov, L., Menzies, S., Reid, J., & Connor, J.R. (2001). Characterization of a novel brain-derived microglial cell line isolated from neonatal rat brain. *Glia*, 35(1), 53-62. doi: 10.1002/glia.1070.

Chen, L., Cui, Y., Jiang, D., Ma, C. T., Tse, H.F., Hwu, W. L., & Lian, Q. (2017). Management of Leigh syndrome: Current status and new insights. *Clinical Genetics*, 93(6)

Chinnery, P. F., Johnson, M. A., Wardell, T. M., Singh-Kler, R., Hayes, C., Brown, D. T., Taylor, R. W., Bindoff, L. A., Turnbull, D. M. (2000). The epidemiology of pathogenic mitochondrial DNA mutations. *Ann Neurol*, 48(2), 188-93

Chouchani, E. T., Pell, V. R., Gaude, E., Aksentijević, D., Sundier, S. Y., Robb, E. L., Logan, A., Nadtochiy, S. M., Ord, E., Smith, A. C., Eyassu, F., Shirley, R., Hu, C. H., Dare, A. J., James, A. M., Rogatti, S., Hartley, R. C., Eaton, S., Costa, A., Brookes, P. S., … & Murphy, M.P. (2014). Ischaemic accumulation of succinate controls reperfusion injury through mitochondrial ROS. *Nature*, 515(7527), 431–435. https://doi.org/10.1038/nature13909

Christen, M., Janzen, N., Fraser, A., Sewell, A.C., Jagannathan, V., Guevar, J., Leeb, T., & Sanchez-Masian, D. (2021). L2HGDH Missense Variant in a Cat with L-2-Hydroxyglutaric Aciduria. *Genes*, 12(5), 682. https://doi.org/10.3390/genes12050682

Coley, A.A. & Gao, W.J. (2018). PSD95: A synaptic protein implicated in schizophrenia or autism? *Prog Neuropsychopharmacol Biol Psychiatry*, 82, 187-194. doi:10.1016/j.pnpbp.2017.11.016

Cordes, T., Lucas, A., Divakaruni, A.S., Murphy, A.N., Cabrales, P., & Metallo, C. M. (2020). Itaconate modulates tricarboxylic acid and redox metabolism to mitigate reperfusion injury. *Molecular Metabolism*, 32, 122–135. https://doi.org/10.1016/j.molmet.2019.11.019

Cordes, T., Wallace, M., Michelucci, A., Divakaruni, A. S., Sapcariu, S. C., Sousa, C., Koseki, H., Cabrales, P., Murphy, A. N., Hiller, K., & Metallo, C. M. (2016). Immunoresponsive Gene 1 and Itaconate Inhibit Succinate Dehydrogenase to Modulate Intracellular Succinate Levels. *The Journal of Biological Chemistry*, 291(27), 14274–14284. https://doi.org/10.1074/jbc.M115.685792

Dang, L., White, D. W., Gross, S., Bennett, B. D., Bittinger, M. A., Driggers, E. M., Fantin, V. R., Jang, H. G., Jin, S., Keenan, M. C., Marks, K. M., Prins, R. M., Ward, P. S., Yen, K. E., Liau, L. M., Rabinowitz, J. D., Cantley, L. C., Thompson, C. B., Vander Heiden, M. G., & Su, S. M. (2009). Cancer-associated IDH1 mutations produce 2-hydroxyglutarate. *Nature*, 462(7274), 739–744. https://doi.org/10.1038/nature08617

Daniels, B. P., Kofman, S. B., Smith, J. R., Norris, G. T., Snyder, A. G., Kolb, J. P., Gao, X., Locasale, J. W., Martinez, J., Gale, M., Jr, Loo, Y. M., & Oberst, A. (2019). The Nucleotide Sensor ZBP1 and Kinase RIPK3 Induce the Enzyme

IRG1 to Promote an Antiviral Metabolic State in Neurons. *Immunity*, 50(1), 64–76.e4. https://doi.org/10.1016/j.immuni.2018.11.017

Davies, L. C., Rice, C. M., Palmieri, E. M., Taylor, P. R., Kuhns, D. B., & McVicar, D. W. (2017). Peritoneal tissue-resident macrophages are metabolically poised to engage microbes using tissue-niche fuels. *Nature Communications*, 8(1), 2074. https://doi.org/10.1038/s41467-017-02092-0

de Haas, R., Russel, F. G., & Smeitink, J. A. (2016). Gait analysis in a mouse model resembling Leigh disease. *Behavioural Brain Research,* 296, 191-198

Delonlay, P., Rötig, A., & Sarnat, H. B. (2013). Respiratory chain deficiencies. *Handb Clin Neurol*, 113, 1651-66. doi: 10.1016/B978-0-444-59565-2.00033-2.

Dobolyi, A., Bago, A., Palkovits, M., Nemeria, N. S., Jordan, F., Doczi, J., Ambrus, A., Adam-Vizi, V., & Chinopoulos, C. (2020). Exclusive neuronal detection of KGDHC-specific subunits in the adult human brain cortex despite pancellular protein lysine succinylation. *Brain Structure & Function*, 225(2), 639–667. https://doi.org/10.1007/s00429-020-02026-5

Du, S., Wang, Y., Alatrash, N., Weatherly, C. A., Roy, D., MacDonnell, F.M., & Armstrong, D.W. (2019). Altered profiles and metabolism of l-and d-amino acids in cultured human breast cancer cells vs. non-tumorigenic human breast epithelial cells. *J. Pharm. Biomed. Anal*, 164, 421– 429. DOI: 10.1016/j.jpba.2018.10.047

Du, X. & Hu, H. (2021). The Roles of 2-Hydroxyglutarate. *Frontiers in Cell and Developmental Biology,* 9, 651317. https://doi.org/10.3389/fcell.2021.651317

El Kasmi, K. C. & Stenmark, K. R. (2015). Contribution of metabolic reprogramming to macrophage plasticity and function. *Seminars in Immunology*, 27(4), 267–275. https://doi.org/10.1016/j.smim.2015.09.001

El-Hattab, A. W., Adesina, A. M., Jones, J., & Scaglia, F. (2015). MELAS syndrome: Clinical manifestations, pathogenesis, and treatment options. *Molecular Genetics and Metabolism*, 116(1-2), 4-12. doi:10.1016/j.ymgme.2015.06.004.

Ernster, L. & Forsmark-Andree, P. (1993). Ubiquinol: an endogenous antioxidant in aerobic organisms. *Clin Investig*,;71(8 Suppl), S60–S65.

Ewaschuk, J. B., Naylor, J. M., & Zello, G. A. (2005). D-Lactate in Human and Ruminant Metabolism. *The Journal of Nutrition,* 135(7), 1619–1625. https://doi.org/10.1093/jn/135.7.1619

Facci, M. R., Auray, G., Meurens, F., Buchanan, R., van Kessel, J., & Gerdts, V. (2011). Stability of expression of reference genes in porcine peripheral blood mononuclear and dendritic cells. *Vet Immunol Immunopathol*, 141(1-2), 11-5. doi: 10.1016/j.vetimm.2011.01.005.

Fall, F., Lamy, E., Brollo, M., Naline, E., Lenuzza, N., Thévenot, E., Devillier, P., & Grassin-Delyle, S. (2020). Metabolic reprograming of LPS-stimulated human lung macrophages involves tryptophan metabolism and the

aspartate-arginosuccinate shunt. *PloS one*, 15(4), e0230813. https://doi.org/10.1371/journal.pone.0230813

Fan, H., Tang, H. B., Chen, Z., Wang, H.Q., Zhang, L., Jiang, Y., Li, T., Yang, C.F., Wang, X. Y., Li, X., Wu, S. X., & Zhang, G.L. (2020). Inhibiting HMGB1-RAGE axis prevents pro-inflammatory macrophages/microglia polarization and affords neuroprotection after spinal cord injury. *Journal of Neuroinflammation*, 17(1), 295. https://doi.org/10.1186/s12974-020-01973-4

Fan, J., Teng, X., Liu, L., Mattaini, K. R., Looper, R. E., Vander Heiden, M. G., & Rabinowitz, J. D. (2015). Human phosphoglycerate dehydrogenase produces the oncometabolite D-2-hydroxyglutarate. *ACS Chemical Biology*, 10(2), 510–516. https://doi.org/10.1021/cb500683c

Felici, R., Cavone, L., Lapucci, A., Guasti, D., Bani, D., & Chiarugi, A. (2014). PARP inhibition delays progression of mitochondrial encephalopathy in mice. *Neurotherapeutics: the Journal of the American Society for Experimental NeuroTherapeutics,* 11(3), 651–664. https://doi.org/10.1007/s13311-014-0285-y

Ferrari, M., Jain, I. H., Goldberger, O., Rezoagli, E., Thoonen, R., Cheng, K. H., Sosnovik, D. E., Scherrer-Crosbie, M., Mootha, V. K., & Zapol, W. M. (2017). Hypoxia treatment reverses neurodegenerative disease in a mouse model of Leigh syndrome. *PNAS,* 114(21), E4241–E4250

Finsterer, J. (2008). Leigh and Leigh-Like Syndrome in Children and Adults. *Pediatric Neurology*, 39(4), 223-235

Frizzell, N., Rajesh, M., Jepson, M. J., Nagai, R., Carson, J. A., Thorpe, S. R., & Baynes, J. W. (2009). Succination of thiol groups in adipose tissue proteins in diabetes: succination inhibits polymerization and secretion of adiponectin. *J. Biol. Chem*, 284(38), 25772–25781. https://doi.org/10.1074/jbc.M109.019257

Frizzell, N., Thomas, S.A., Carson, J.A., & Baynes, J.W. (2012). Mitochondrial stress causes increased succination of proteins in adipocytes in response to glucotoxicity. *Biochem.J*, 445, 247–254

Garcia-Cazorla, A., Quadros, E. V., Nascimento, A., Garcia-Silva, M. T., Briones, P., Montoya, J., Ormazábal, A., Artuch, R., Sequeira, J. M., Blau, N., Arenas, J., Pineda, M., & Ramaekers, V. T. (2008). Mitochondrial diseases associated with cerebral folate deficiency. *Neurology,* 70(16), 1360-1362

Gerards, M., Van Den Bosch, B. J. C., Danhauser K, et al. (2011). Riboflavin-responsive oxidative phosphorylation complex I deficiency caused by defective ACAD9: new function for an old gene. *Brain*, 134(1), 210-219. doi:10.1093/brain/awq273.

Gold, R., Giovannoni, G., Phillips, J. T., Fox, R. J., Zhang, A., Meltzer, L., & Kurukulasuriya, N. C. (2015). Efficacy and safety of delayed-release dimethyl fumarate in patients newly diagnosed with relapsing-remitting multiple sclerosis (RRMS). *Multiple Sclerosis*, 21(1), 57–66. doi:10.1177/1352458514537013

Goto, Y.-I., Nonaka, I., & Horai, S. (1990). A mutation in the tRNALeu(UUR) gene associated with the MELAS subgroup of mitochondrial

encephalomyopathies. *Nature*, 348(6302), 651-653. doi:10.1038/348651a0.

Guadagno, J., Xu, X., Karajgikar, M., Brown, A., & Cregan, S. P. (2013). Microglia-derived TNFα induces apoptosis in neural precursor cells via transcriptional activation of the Bcl-2 family member Puma. *Cell Death Dis*, 4, e538 https://doi.org/10.1038/cddis.2013.59

Guo, X., Zhu, Z., Zhang, W., Meng, X., Zhu, Y., Han, P., Zhou, X., Hu, Y., & Wang, R. (2017). Nuclear translocation of HIF-1α induced by influenza A (H1N1) infection is critical to the production of proinflammatory cytokines. *Emerg Microbes Infect*, 6(5), e39. doi: 10.1038/emi.2017.21.

Gupta, S., Vanderbilt, C. M., Leibovich, B. C., Herrera-Hernandez, L., Raghunathan, A., Sukov, W. R., Voss, J. S., Barr Fritcher, E. G., Reed, K. A., Lohse, C. M., Reuter, V. E., Jimenez, R. E., Thompson, R. H., & Cheville, J. C. (2020). Secondary renal neoplasia following chemotherapy or radiation in pediatric patients. *Hum Pathol*, 1-13. doi: 10.1016/j.humpath.2020.07.014.

Hargreaves, I. P. (2014). Coenzyme Q10 as a therapy for mitochondrial disease. *The International Journal of Biochemistry and Cell Biology*, 49, 105-111. doi:10.1016/j.biocel.2014.01.020.

Hegde, V. R., Vogel, R., & Feany, M. B. (2014). Glia are critical for the neuropathology of complex I deficiency in Drosophila. *Human Molecular Genetics*, 23(17), 4686–4692. https://doi.org/10.1093/hmg/ddu188

Henry, J. L., Coggin, D. L., & King, C.R. (1993). High-level expression of the ribosomal protein L19 in human breast tumors that overexpress erbB-2. *Cancer Res*, 53(6), 1403-8.

Hirschey, M. D. & Zhao, Y. (2015). Metabolic Regulation by Lysine Malonylation, Succinylation, and Glutarylation. *Molecular & Cellular Proteomics: MCP*, 14(9), 2308–2315. https://doi.org/10.1074/mcp.R114.046664

Hooftman, A., Angiari, S., Hester, S., … , Irvine, A. D., Fischer, R., & O'Niell, L. A. J. (2020). The Immunomodulatory Metabolite Itaconate Modifies NLRP3 and Inhibits Inflammasome Activation. *Cell Metabolism*, 32(3), 468-478.E7

Iannetti, E. F., Smeitink, J. A. M., Willems, P. H. G. M., Beyrath, J., & Koopman, W. J. H. (2018). Rescue from galactose-induced death of Leigh Syndrome patient cells by pyruvate and NAD+. *Cell Death Dis*, 9, 1135. https://doi.org/10.1038/s41419-018-1179-4

Iizuka, T. & Sakai, F. (2005). Pathogenesis of stroke-like episodes in MELAS: analysis of neurovascular cellular mechanisms. *Curr Neurovasc Res*, 2(1), 29-45. doi: 10.2174/1567202052773544.

Intlekofer, A. M., Dematteo, R. G., Venneti, S., Finley, L. W., Lu, C., Judkins, A. R., Rustenburg, A. S., Grinaway, P. B., Chodera, J. D., Cross, J. R., & Thompson, C. B. (2015). Hypoxia Induces Production of L-2-Hydroxyglutarate. *Cell Metabolism*, 22(2), 304–311. https://doi.org/10.1016/j.cmet.2015.06.023

Intlekofer, A. M., Wang, B., Liu, H., Shah, H., Carmona-Fontaine, C., Rustenburg, A. S., Salah, S., Gunner, M. R., Chodera, J. D., Cross, J. R., and Thompson,

C. B. (2017). L-2-Hydroxyglutarate production arises from noncanonical enzyme function at acidic pH. *Nat Chem Biol*, 13(5), 494-500. doi: 10.1038/nchembio.2307.

Iyer, S., Bergquist, K., Young, K., Gnaiger, E., Rao, R. R., & Bennett, J. P. (2012). Mitochondrial gene therapy improves respiration, biogenesis, and transcription in G11778A Leber's hereditary optic neuropathy and T8993G Leigh's syndrome cells. *Human Gene Therapy*, 23(6), 647–657. https://doi.org/10.1089/hum.2011.177

Jain, I. H., Zazzeron, L., Goldberger, O., Marutani, E., Wojtkiewicz, G. R., Ast, T., Wang, H., Schleifer, G., Stepanova, A., Brepoels, K., Schoonjans, L., Carmeliet, P., Galkin, A., Ichinose, F., Zapol, W. M., & Mootha, V. K. (2019). Leigh Syndrome Mouse Model Can Be Rescued by Interventions that Normalize Brain Hyperoxia, but Not HIF Activation. *Cell Metabolism*, 30(4), 824–832.e3. https://doi.org/10.1016/j.cmet.2019.07.006

Jha, A. K., Huang, S. C., Sergushichev, A., Lampropoulou, V., Ivanova, Y., Loginicheva, E., Chmielewski, K., Stewart, K.M., Ashall, J., Everts, B., Pearce, E .J., Driggers, E. M., Artyomov, M. N. (2015). Network integration of parallel metabolic and transcriptional data reveals metabolic modules that regulate macrophage polarization. *Immunity*, 42(3), 419-30. doi: 10.1016/j.immuni.2015.02.005. PMID: 25786174.

Jiao, H., Jiang, D., Hu, X., Du, W., Ji, L., Yang, Y., Li, X., Sho, T., Wang, X., Li, Y., Wu, Y. T., Wei, Y. H., Hu, X., & Yu, L. (2021). Mitocytosis, a migrasome-

mediated mitochondrial quality-control process. *Cell,* 184(11), 2896-2910.e13. doi: 10.1016/j.cell.2021.04.027. PMID: 34048705.

Jin, Z., Wei, W., Yang, M., Du, Y., & Wan, Y. (2014). Mitochondrial Complex I Activity Suppresses Inflammation and Enhances Bone Resorption by Tipping the Balance of Macrophage-Osteoclast Polarization. *Cell Metab*, 20(3), 483-498

Johnson, S. C., Yanos, M. E., Bitto, A., Castanza, A., Gagnidze, A., Gonzalez, B., Gupta, K., Hui J., Jarvie, C., Johnson, B. M., Letexier, N., McCanta, L., Sangesland, M., Tamis, O., Uhde, L., Ende, A. V. D., Rabinovitch, P. S., Suh, Y., & Kaeberlein, M. (2015). Dose-dependent effects of mTOR inhibition on weight and mitochondrial disease in mice. *Font. Genet,* 6, 247

Johnson, S. C., Yanos, M. E., Kayser, E. B., Quintana, A., Sangesland, M., Castanza, A., Uhde, L., Hui J., Wall, V. Z., Gagnidze, A., Oh, K., Wasko, B. M., Ramos, F. J., Palmiter, R. D., Rabinovitch, P. S., Morgan, P. G., Sedensky, M. M., & Kaeberlein, M. (2013). mTOR Inhibition Alleviates Mitochondrial Disease in a Mouse Model of Leigh Syndrome. *Science*, 342(6165), 1524-1528

Jurkiewicz E, Chełstowska S, Pakuła-Kościesza I, Malczyk K, Nowak K, Bekiesińska-Figatowska M, Sykut-Cegielska J, Piekutowska-Abramczuk D, & Pronicka E. (2011). Proton MR Spectroscopy in Patients with Leigh Syndrome. *Neuroradiol J*, 24(3), 424-8. doi: 10.1177/197140091102400312.

Kayser, E. B., Sedensky, M. M., & Morgan, P. G. (2016). Region-Specific Defects of Respiratory Capacities in the Ndufs4(KO) Mouse Brain. *PloS one*, 11(1), e0148219. https://doi.org/10.1371/journal.pone.0148219

Kelly, B., & O'Neill, L.A. (2015). Metabolic reprogramming in macrophages and dendritic cells in innate immunity. *Cell Research*, 25(7), 771–784. https://doi.org/10.1038/cr.2015.68

Kim, J., Ahn, M., Choi, Y., & Shin, T. (2020). Upregulation of Cathepsins in Olfactory Bulbs Is Associated with Transient Olfactory Dysfunction in Mice with Experimental Autoimmune Encephalomyelitis. *Mol Neurobiol*, 57, 3412–3423. https://doi.org/10.1007/s12035-020-01952-z

Kimura, T., Hamase, K., Miyoshi, Y. et al. (2016). Chiral amino acid metabolomics for novel biomarker screening in the prognosis of chronic kidney disease. *Sci Rep,* 6, 26137. https://doi.org/10.1038/srep26137

Koga, Y., Povalko, N., Inoue, E., Nakamura, H., Ishii, A., Suzuki, Y., Yoneda, M., Kanda, F., Kubota, M., Okada, H., & Fujii, K. (2018). Therapeutic regimen of L-arginine for MELAS: 9-year, prospective, multicenter, clinical research. *Journal of Neurology*, *265*(12), 2861–2874. https://doi.org/10.1007/s00415-018-9057-7

Kohanbash, G., Carrera, D. A., Shrivastav, S., Ahn, B. J., Jahan, N., Mazor, T., et al. (2017). Isocitrate dehydrogenase mutations suppress STAT1 and CD8(+) T cell accumulation in gliomase. *J. Clin. Investig,* 127, 1425–1437. doi: 10.1172/JCI90644

Kranendijk, M., Struys, E. A., van Schaftingen, E., Gibson, K .M., Kanhai, W. A., van der Knaap, M. S., et al. (2010). IDH2 mutations in patients with D-2-hydroxyglutaric aciduria. *Science,* 330, 336. doi: 10.1126/science.1192632

Kruse, S. E., Watt, W. C., Marcinek, D. J., Kapur, R. P., Schenkman, K. A., & Palmiter, R. D. (2008). Mice with mitochondrial complex I deficiency develop a fatal encephalomyopathy. *Cell Metabolism*, 7(4), 312–320. https://doi.org/10.1016/j.cmet.2008.02.004

Krycer, J. R., Elkington, S. D., Diaz-Vegas, A., Cooke, K. C., Burchfield, J. G., Fisher-Wellman, K. H., Cooney, G. J., Fazakerley, D. J., & James, D. E. (2020). Mitochondrial oxidants, but not respiration, are sensitive to glucose in adipocytes. *The Journal of Biological Chemistry*, 295(1), 99–110. https://doi.org/10.1074/jbc.RA119.011695

Krycer, J. R., Yugi, K., Hirayama, A., Fazakerley, D. J., Quek, L. E., Scalzo, R., Ohno, S., Hodson, M. P., Ikeda, S., Shoji, F., Suzuki, K., Domanova, W., Parker, B. L., Nelson, M. E., Humphrey, S. J., Turner, N., Hoehn, K. L., Cooney, G. J., Soga, T., Kuroda, S., & James, D. E. (2017). Dynamic Metabolomics Reveals that Insulin Primes the Adipocyte for Glucose Metabolism. *Cell Rep*, 21(12), 3536-3547. doi: 10.1016/j.celrep.2017.11.085.

Kulkarni, R. A., Bak, D. W., Wei, D., Bergholtz, S. E., Briney, C. A., Shrimp, J. H., Alpsoy, A., Thorpe, A. L., Bavari, Arissa E., Crooks, D. R., Levy, M., Florens, L., Washburn, M. P., Frizzell, N., Dykhuizen, E. C., Weerapana, E., Linehan,

W. M., & Meier, J. L. (2019). A chemoproteomic portrait of the oncometabolite fumarate. *Nature Chemical Biology*, 15, 391–400

Kunze, R., Urrutia, A., Hoffmann, A., Liu, H., Helluy, X., Pham, M., Reischl, S., Korff, T., & Marti, H. H. (2015). Dimethyl fumarate attenuates cerebral edema formation by protecting the blood-brain barrier integrity. *Exp Neurol*, 266, 99-111. doi: 10.1016/j.expneurol.2015.02.022.

Kuo, P. C., Weng, W. T., Scofield, B. A., Furnas, D., Paraiso, H. C., Yu, I. C., & Yen, J. H. (2021). Immunoresponsive gene 1 modulates the severity of brain injury in cerebral ischaemia. *Brain Commun*, 3(3), fcab187. doi: 10.1093/braincomms/fcab187.

Kuo, P. C., Weng, W. T., Scofield, B. A., Paraiso, H. C., Brown, D. A., Wang, P. Y., Yu, I. C., & Yen, J. H. (2020). Dimethyl itaconate, an itaconate derivative, exhibits immunomodulatory effects on neuroinflammation in experimental autoimmune encephalomyelitis. *Journal of Neuroinflammation,* 17(1), 138. https://doi.org/10.1186/s12974-020-01768-7

Lai, R. K. & Goldman, P. (1992). Organic acid profiling in adipocyte differentiation of 3T3-F442A cells: increased production of Krebs cycle acid metabolites. *Metabolism*, 41(5), 545-7. doi: 10.1016/0026-0495(92)90216-w.

Lake, N. J., Compton, A. G., Rahman, S. & Thorburn, D. R. (2016). Leigh syndrome: One disorder, more than 75 monogenic causes. *Ann Neurol*, 79, 190-203. https://doi.org/10.1002/ana.24551

Lampropoulou, V., Sergushichev, A., Bambouskova, M., Nair, S., Vincent, E. E., Loginicheva, E., Cervantes-Barragan, L., Ma, X., Huang, S. C., Griss, T.,

Weinheimer, C. J., Khader, S., Randolph, G. J., Pearce, E. J., Jones, R. G., Diwan, A., Diamond, M. S., & Artyomov, M. N. (2016). Itaconate Links Inhibition of Succinate Dehydrogenase with Macrophage Metabolic Remodeling and Regulation of Inflammation. *Cell Metabo*, 24(1), 158-66 10.1016/j.cmet.2016.06.004

Laugel, V., This-Bernd, V., Cormier-Daire, V., Speeg-Schatz, C., de Saint-Martin, A., & Fischbach, M. (2007). Early-onset ophthalmoplegia in Leigh-like syndrome due to NDUFV1 mutations. *Pediatr Neurol*, 36(1), 54–57.

Lauro, C., & Limatola, C. (2020). Metabolic Reprograming of Microglia in the Regulation of the Innate Inflammatory Response. *Frontiers in Immunology*, 11(493). https://doi.org/10.3389/fimmu.2020.00493

Lee, C. F., Caudal, A., Abell, L., Gowda, G. A. N., & Tian, R. (2019). Targeting NAD+ Metabolism as Interventions for Mitochondrial Disease. *Scientific Reports*, 9, 3073

Lei, Y., Guerra Martinez, C., Torres-Odio, S., Bell, S. L., Birdwell, C.E., Bryant, J. D., Tong, C. W., Watson, R. O., West, L. C., & West, A. P. (2021). Elevated type I interferon responses potentiate metabolic dysfunction, inflammation, and accelerated aging in mtDNA mutator mice. *Science Advances*, 7(22), eabe7548. https://doi.org/10.1126/sciadv.abe7548

Leigh, D. (1951). Subacute necrotizing encephalomyelopathy in an infant. *Journal of Neurology, Neurosurgery, and Psychiatry*, 14(3), 216–221. https://doi.org/10.1136/jnnp.14.3.216

Leong, D. W., Komen, J. C., Hewitt, C. A., Arnaud, E., McKenzie, M., Phipson, B., Bahlo, M., Laskowski, A., Kinkel, S. A., Davey, G. M., Heath, W. R., Voss, A. K., Zahedi, R. P., Pitt, J. J., Chrast, R., Sickmann, A., Ryan, M. T., Smyth, G. K., Thorburn, D. R., & Scott, H. S. (2012). Proteomic and metabolomic analyses of mitochondrial complex I-deficient mouse model generated by spontaneous B2 short interspersed nuclear element (SINE) insertion into NADH dehydrogenase (ubiquinone) Fe-S protein 4 (Ndufs4) gene. *The Journal of Biological Chemistry*, 287(24), 20652–20663. https://doi.org/10.1074/jbc.M111.327601

Leshinsky-Silver, E., Lebre, A. S., Minai, L., Saada, A., Steffann, J., Cohen, S., Rötig, A., Munnich, A., Lev, D., & Lerman-Sagie, T. (2009). NDUFS4 mutations cause Leigh syndrome with predominant brainstem involvement. *Mol Genet Metab*. 97(3), 185-9. doi: 10.1016/j.ymgme.2009.03.002.

Li, Y., Chen, X., Zhang, H., Xiao, J., Yang, C., Chen, W., Wei, Z., Chen, X., & Liu, J. (2020). 4-Octyl Itaconate Alleviates Lipopolysaccharide-Induced Acute Lung Injury in Mice by Inhibiting Oxidative Stress and Inflammation. *Drug Design, Development and Therapy*, 14, 5547–5558. https://doi.org/10.2147/DDDT.S280922

Liao, S. T., Han, C., Xu, D. Q. Fu, X. W., Wang, J. S., & Ling-Yi Kong, L. Y. (2019). 4-Octyl itaconate inhibits aerobic glycolysis by targeting GAPDH to exert anti-inflammatory effects. *Nat Commun*, 10, 5091. https://doi.org/10.1038/s41467-019-13078-5

Linker, R. A., Lee, D. H., Ryan, S., van Dam, A. M., Conrad, R., Bista, P., Zeng, W., Hronowsky, X., Buko, A., Chollate, S., Ellrichmann, G., Brück, W., Dawson, K., Goelz, S., Wiese, S., Scannevin, R. H., Lukashev, M., & Gold, R. (2011). Fumaric acid esters exert neuroprotective effects in neuroinflammation via activation of the Nrf2 antioxidant pathway. *Brain*, 134(Pt 3), 678-92. doi: 10.1093/brain/awq386.

Liu, L., Shah, S., Fan, J., Park, J. O., Wellen, K. E., & Rabinowitz, J. D. (2016). Malic enzyme tracers reveal hypoxia-induced switch in adipocyte NADPH pathway usage. *Nature Chemical Biology*, 12(5), 345–352. https://doi.org/10.1038/nchembio.2047

Liu, L., Zhang, K., Sandoval, H., Yamamoto, S., Jaiswal, M., Sanz, E., Li, Z., Hui, J., Graham, B. H., Quintana, A., & Bellen, H. J. (2015). Glial lipid droplets and ROS induced by mitochondrial defects promote neurodegeneration. *Cell*, 160(1-2), 177–190. https://doi.org/10.1016/j.cell.2014.12.019

Lorenzo, M. P., Dudzik, D., Varas, E., Gibellini, M., Skotnicki, M., Zorawski, M., Zarzycki, W., Pellati, F. & García, A. (2015). Optimization and validation of a chiral GC–MS method for the determination of free d-amino acids ratio in human urine: application to a gestational diabetes mellitus study. *J. Pharm. Biomed. Anal,* 107, 480–487. DOI: 10.1016/j.jpba.2015.01.015

Lynch, M. A. (2020). Can the emerging field of immunometabolism provide insights into neuroinflammation? *Prog Neurobiol*, 184, 101719. doi: 10.1016/j.pneurobio.2019.101719. Epub 2019 Nov 6. PMID: 31704314.

Majamaa, K., Moilanen, J. S., Uimonen, S., Remes, A. M., Salmela, P. I., Kärppä, M., Majamaa-Voltti, K. A., Rusanen, H., Sorri, M., Peuhkurinen, K. J., & Hassinen, I. E. (1998). Epidemiology of A3243G, the mutation for mitochondrial encephalomyopathy, lactic acidosis, and strokelike episodes: prevalence of the mutation in an adult population. *American Journal of Human Genetics*, 63(2), 447–454. https://doi.org/10.1086/301959

Man, P. Y., Turnbull, D. M., Chinnery, P. F. (2002). Leber hereditary optic neuropathy. *J Med Genet*, 39, 162–69

Manuel, A. M., Walla, M. D., Dorn, M. T., Tanis, R. M., Piroli, G. G., & Frizzell, N. (2020). Fumarate and oxidative stress synergize to promote stability of C/EBP homologous protein in the adipocyte. *Free Radical Biology & Medicine*, 148, 70–82. https://doi.org/10.1016/j.freeradbiomed.2019.12.037

Manuel, A. M., Walla, M. D., Faccenda, A., Martin, S. L., Tanis, R. M., Piroli, G. G., Adam, J., Kantor, B., Mutus, B., Townsend, D. M., & Frizzell, N. (2017). Succination of Protein Disulfide Isomerase Links Mitochondrial Stress and Endoplasmic Reticulum Stress in the Adipocyte During Diabetes. *Antioxid Redox Signal*, 27(16), 1281-1296

Manwaring, N., Jones, M. M., Wang, J. J., Rochtchina, E., Howard, C., Mitchell, P., & Sue, C. M. (2007). Population prevalence of the MELAS A3243G mutation. *Mitochondrion*.,7(3), 230-3. doi: 10.1016/j.mito.2006.12.004

Marschallinger, J., Iram, T., Zardeneta, M., Lee, S. E., Lehallier, B., Haney, M. S., Pluvinage, J. V., Mathur, V., Hahn, O., Morgens, D. W., Kim, J., Tevini, J., Felder, T. K., Wolinski, H., Bertozzi, C. R., Bassik, M. C., Aigner, L., & Wyss-

Coray, T. (2020). Lipid-droplet-accumulating microglia represent a dysfunctional and proinflammatory state in the aging brain. *Nat Neurosci*, 23(2), 194-208. doi: 10.1038/s41593-019-0566-1

Martín, M. A., Blázquez, A., Gutierrez-Solana, L. G., Fernández-Moreira, D., Briones, P., Andreu, A. L., Garesse, R., Campos, Y., & Arenas, J. (2005). Leigh syndrome associated with mitochondrial complex I deficiency due to a novel mutation in the NDUFS1 gene. *Arch Neurol*, 62(4), 659-61. doi: 10.1001/archneur.62.4.659

Mascialino, B., Leinonen, M., & Meier, T. (2012). Meta-analysis of the prevalence of Leber hereditary optic neuropathy mtDNA mutations in Europe. *Eur J Ophthalmol*, 22(3), 461-5. doi: 10.5301/ejo.5000055

Mazzei, R., Ungaro, C., Garreffa, G., Conforti, F .L., Mollo, A., Sprovieri, T., Servillo, P., Blasi, V., Gallo, O., Cerasa, A., Lanza, P. L., & Quattrone, A. (2011). Clinical, genetic and magnetic resonance findings in an Italian patient affected by L-2-hydroxyglutaric aciduria. *Neurol Sci*, 32(1), 95-9.

McDowell, R. E., Aulak, K. S., Almoushref, A., Melillo, C. A., Brauer, B. E., Newman, J. E., Tonelli, A. R., & Dweik, R. A. (2020). Platelet glycolytic metabolism correlates with hemodynamic severity in pulmonary arterial hypertension. American journal of physiology. *Lung Cellular and Molecular Physiology*, 318(3), L562–L569. https://doi.org/10.1152/ajplung.00389.2019

McElroy, G. S., Reczek, C. R., Reyfman, P. A., Mithal, D. S., Horbinski, C. M., & Chandel, N. S. (2020). NAD+ Regeneration Rescues Lifespan, but Not

Ataxia, in a Mouse Model of Brain Mitochondrial Complex I Dysfunction. *Cell Metab*, 32(2), 301-308.e6. doi: 10.1016/j.cmet.2020.06.003

McGettrick, A. F. & O'Neill, L. A. (2020). The Role of HIF in Immunity and Inflammation. *Cell Metabolism*, 32(4), 524-536

McLellan, A. C., Plillips, S. A., & Thornalley, P. J. (1992). Fluorimetric assay of d-lactate. *Anal Biochem*, 206, 12–16

Mei, J., Riedel, N., Grittner, U. et al. (2018). Body temperature measurement in mice during acute illness: implantable temperature transponder versus surface infrared thermometry. *Sci Rep*, 8, 3526. https://doi.org/10.1038/s41598-018-22020-6

Merkley, E. D., Metz, T. O., Smith, R. D., Baynes, J. W., & Frizzell, N. (2016). The succinated proteome. *Mass Spectrom Rev*, 33, 98–109

Miller, H. C., Louw, R., Mereis, M., Venter, G., Boshoff, J. D., Mienie, L., van Reenen, M., Venter, M., Lindeque, J. Z., Domínguez-Martínez, A., Quintana, A., & van der Westhuizen, F. H. (2021). Metallothionein 1 Overexpression Does Not Protect Against Mitochondrial Disease Pathology in Ndufs4 Knockout Mice. *Mol Neurobiol*, 58(1),243-262. doi: 10.1007/s12035-020-02121-y.

Mills, E. & O'Niell, L. A. J. (2014). Succinate: a metabolic signal in inflammation. *Trends in Cell Biology*, 24(5), 313-320.

Mills, E. L., Kelly, B., Logan, A., Costa, A. S. H., Varma, M., Bryant, C. E., Tourlomousis, P., Däbritz, J. H. M., Gottlieb, E., Latorre, I., Corr, S. C., McManus, G., Ryan, D., Jacobs, H. T., Szibor, M., Xavier, R. J., Braun, T.,

Frezza, C., Murphy, M. P., & O'Neill, L. A. (2016). Succinate Dehydrogenase Supports Metabolic Repurposing of Mitochondria to Drive Inflammatory Macrophages. *Cell*, 167(2), 457-470.e13. doi: 10.1016/j.cell.2016.08.064.

Mills, E. L., Ryan, D. G., Prag, H. A., Dikovskaya, D., Menon, D., Zaslona, Z., Jedrychowski, M. P., Costa, A. S. H., Higgins, M., Hams, E., Szpyt, J., Runtsch, M. C., King, M. S., McGouran, J. F., Fischer, R., Kessler, B. M., McGettrick, A. F., Hughes, M. M., Carroll, R. G., Booty, L. M., Knatko, E. V., Meakin, P. J., Ashford, M. L. J., Modis, L. K., Brunori, G., Sévin, D. C., Fallon, P. G., Caldwell, S .T., Kunji, E. R. S., Chouchani, E. T., Frezza, C., Dinkova-Kostova, A. T., Hartley, R. C., Murphy, M. P., & O'Neill, L. A.. (2018). Itaconate is an anti-Inflammatory metabolite that activates Nrf2 via alkylation of KEAP1. *Nature,* 556, 113–117. 10.1038/nature25986

Mimaki, M., Wang, X., McKenzie, M., Thorburn, D. R., & Ryan, M. T. (2012). Understanding mitochondrial complex I assembly in health and disease. *BBA Bioenergetics,* 1817(6), 851-862

Mindell, J. A. (2012). Lysosomal acidification mechanisms. *Annu Rev Physiol*, 74, 69-86. doi: 10.1146/annurev-physiol-012110-142317

Modrzejewska, M., Gawronski, M., & Gackowski, D. (2011). Normalization of metabolic data to total thymine content and its application to determination of 2-hydroxyglutarate. *Analytical Biochemistry*, 618(114129). https://doi.org/10.1016/j.ab.2021.114129

Mohana Devi, S., Abishek Kumar, B., Mahalaxmi, I., & Balachandar, V. (2021). Leber's hereditary optic neuropathy: Current approaches and future perspectives on Mesenchymal stem cell-mediated rescue. *Mitochondrion,* 60, 201-218. doi: 10.1016/j.mito.2021.08.013. Epub ahead of print.

Muri, J., Wolleb, H., Broz, P., Carriera, E. M., & Kopf, M. (2020). Electrophilic Nrf2 activators and itaconate inhibit inflammation at low dose and promote IL-1β production and inflammatory apoptosis at high dose. *Redox Biology*, 36(101647), 1-15

Nadtochiy, S. M., Schafer, X., Fu, D., Nehrke, K., Munger, J., & Brookes, P. S. (2016). Acidic pH Is a Metabolic Switch for 2-Hydroxyglutarate Generation and Signaling. *The Journal of Biological Chemistry*, 291(38), 20188–20197. https://doi.org/10.1074/jbc.M116.738799

Nagai, R., Brock, J. W., Blatnik, M., Baatz, J. E., Bethard, J., Walla, M. D., Thorpe, S. R., Baynes, J. W., & Frizzell, N. (2007). Succination of protein thiols during adipocyte maturation: a biomarker of mitochondrial stress. *J. Biol. Chem*, 282, 34219-34228

Nair, S., Huynh, J. P., Lampropoulou, V., Loginicheva, E., Esaulova, E., Gounder, A. P., Boon, A., Schwarzkopf, E. A., Bradstreet, T. R., Edelson, B. T., Artyomov, M. N., Stallings, C. L., & Diamond, M. S. (2018). Irg1 expression in myeloid cells prevents immunopathology during M. tuberculosis infection. *The Journal of Experimental Medicine*, 215(4), 1035–1045. https://doi.org/10.1084/jem.20180118

Nakanishi, H. (2020). Cathepsin regulation on microglial function. *BBA-Proteins and Proteomics*, 1868(9), 140465

Nelson, L. H., Warden, S., & Lenz, K. M. (2017). Sex differences in microglial phagocytosis in the neonatal hippocampus. *Brain, Behavior, and Immunity,* 64, 11–22. https://doi.org/10.1016/j.bbi.2017.03.010

Ng, Y. S., Bindoff, L. A., Gorman, G. S., Klopstock, T., Kornblum, C., Mancuso, M., McFarland, R., Sue, C. M., Suomalainen, A., Taylor, R. W., Thorburn, D. R., & Turnbull, D. M. (2021). Mitochondrial disease in adults: recent advances and future promise. *Lancet Neurol*, 20(7), 573-584. doi: 10.1016/S1474-4422(21)00098-3

O'Callaghan, A. A., Dempsey, E., Iyer, N., Stiegeler, S., Mercurio, K., & Corr, S. C. (2021). Intestinal Metabolites Influence Macrophage Phagocytosis and Clearance of Bacterial Infection. *Frontiers in Cellular and Infection microbiology*, 11, 622491. https://doi.org/10.3389/fcimb.2021.622491

Olagnier, D., Brandtoft, A. M., Gunderstofte, C., Villadsen, N. L., Krapp, C., Thielke, A. L., Laustsen, A., Peri, S., Hansen, A. L., Bonefeld, L., Thyrsted, J., Bruun, V., Iversen, M. B., Lin, L., Artegoitia, V. M., Su, C., Yang, L., Lin, R., Balachandran, S., Luo, Y., … & Holm, C. K. (2018). Nrf2 negatively regulates STING indicating a link between antiviral sensing and metabolic reprogramming. *Nature Communications*, 9(1), 3506. https://doi.org/10.1038/s41467-018-05861-7

Oldham, W. M. & Loscalzo, J. (2016). Quantification of 2-Hydroxyglutarate Enantiomers by Liquid Chromatography-mass Spectrometry. *Bio Protoc,* 6(16). doi:10.21769/BioProtoc.1908

Oldham, W. M., Clish, C. B., Yang, Y., & Loscalzo, J. (2015). Hypoxia-Mediated Increases in L-2-hydroxyglutarate Coordinate the Metabolic Response to Reductive Stress. *Cell Metabolism,* 22(2), 291–303. https://doi.org/10.1016/j.cmet.2015.06.021

Parikh, S., Goldstein, A., Koenig, M.K., et al. (2015). Diagnosis and management of mitochondrial disease: a consensus statement from the Mitochondrial Medicine Society. *Genetics in Medicine*, 17(9), 689-701. doi:10.1038/gim.2014.177

Parodi, B., Rossi, S., Morando, S., Cordano, C., Bragoni, A., Motta, C., Usai, C., Wipke, B. T., Scannevin, R. H., Mancardi, G. L., Centonze, D., Kerlero de Rosbo, N., & Uccelli, A. (2015). Fumarates modulate microglia activation through a novel HCAR2 signaling pathway and rescue synaptic dysregulation in inflamed CNS. *Acta Neuropathologica*, 130(2), 279–295. https://doi.org/10.1007/s00401-015-1422-3

Patel, K. P., O'Brien, T. W., Subramony, S. H., Shuster, J., & Stacpoole, P. W. (2012). The spectrum of pyruvate dehydrogenase complex deficiency: clinical, biochemical and genetic features in 371 patients. *Molecular Genetics and Metabolism,* 105(1), 34–43. https://doi.org/10.1016/j.ymgme.2011.09.032

Patgiri, A., Skinner, O. S., Miyazaki, Y. et al. (2020). An engineered enzyme that targets circulating lactate to alleviate intracellular NADH:NAD+ imbalance. *Nat Biotechnol*, 38, 309–313. https://doi.org/10.1038/s41587-019-0377-7

Peragallo, J.H. & Newman, N.J. (2015). Is there treatment for Leber hereditary optic neuropathy?, *Current Opinion in Ophthalmology*, 26(6), 450-457 doi: 10.1097/ICU.0000000000000212

Petruzzella, V. & Papa, S. (2002). Mutations in human nuclear genes encoding for subunits of mitochondrial respiratory complex I: the NDUFS4 gene. *Gene,* 286, 149–154

Piroli, G. G., Manuel, A. M. Clapper, A. C., Walla, M. D., Baatz, J. E., Palmiter, R. D., Quintana, A., & Frizzell, N. (2016). Succination is Increased on Select Proteins in the Brainstem of the NADH dehydrogenase (ubiquinone) Fe-S protein 4 (Ndufs4) Knockout Mouse, a Model of Leigh Syndrome. *Mol Cell Proteomics,* 12(2), 445-461

Piroli, G. G., Manuel, A. M., Patel, T., Walla, M. D., Shi, L., Lanci, S. A., Wang, J., Galloway, A., Ortinski, P.I., Smith, D. S., & Frizzell, N. (2019). Identification of Novel Protein Targets of Dimethyl Fumarate Modification in Neurons and Astrocytes Reveals Actions Independent of Nrf2 Stabilization. *Molecular & Cellular Proteomics: MCP*, 18(3), 504–519. https://doi.org/10.1074/mcp.RA118.000922

Piroli, G. G., Manuel, A. M., Walla, M. D., Jepson, M. J., Brock, J. W., Rajesh, M. P., Tanis, R. M., Cotham, W. E., & Frizzell, N. (2014). Identification of

protein succination as a novel modification of tubulin. *The Biochemical Journal*, 462(2), 231–245. https://doi.org/10.1042/BJ20131581

Piroli, G. G., McCain, R. S., Manuel, A. M., Smith, H. H., Cotham, W. E., Walla, M. D., & Frizzell, N. Succination of Dihydrolipoyllysine Succinyltransferase by Fumarate Exacerbates Defective Mitochondrial ATP Production during Complex I Deficiency. [preprint]. 2021 September. Available from: https://www.biorxiv.org/content/10.1101/2020.01.09.900514v2. doi: https://doi.org/10.1101/2020.01.09.900514.

Poole L. B. (2015). The basics of thiols and cysteines in redox biology and chemistry. *Free Radical Biology & Medicine*, 80, 148–157. https://doi.org/10.1016/j.freeradbiomed.2014.11.013

Qualls, J. E., Subramanian, C., Rafi, W., Smith, A. M., Balouzian, L., DeFreitas, A. A., Shirey, K. A., Reutterer, B., Kernbauer, E., Stockinger, S., Decker, T., Miyairi, I., Vogel, S. N., Salgame, P., Rock, C. O., & Murray, P. J. (2012). Sustained generation of nitric oxide and control of mycobacterial infection requires argininosuccinate synthase 1. *Cell Host & Microbe,* 12(3), 313–323. https://doi.org/10.1016/j.chom.2012.07.012

Quintana, A., Kruse, S. E., Kapur, R. P., Sanz, E., & Palmiter, R. D. (2010). Complex I deficiency due to loss of Ndufs4 in the brain results in progressive encephalopathy resembling Leigh syndrome. *Proc Natl Acad Sci USA*, 107, 10996-1001.

Rahman, S., Brown, R. M., Chong, W. K., Wilson, C. J., & Brown, G. K. (2001). A SURF1 gene mutation presenting as isolated leukodystrophy. *Ann Neurol*, 49(6), 797-800. doi: 10.1002/ana.1060

Raimondi, V., Ciccarese, F., & Ciminale, V. (2020). Oncogenic pathways and the electron transport chain: a dangeROS liaison. *British Journal of Cancer,* 122(2), 168–181. https://doi.org/10.1038/s41416-019-0651-y

Rattigan, K. M., Pountain, A. W., Regnault, C., Achcar, F., Vincent, I. M., Goodyear, C. S., & Barrett, M. P. (2018). Metabolomic profiling of macrophages determines the discrete metabolomic signature and metabolomic interactome triggered by polarising immune stimuli. *PloS one,* 13(3), e0194126. https://doi.org/10.1371/journal.pone.0194126

Reiter-Brennan, C., Semmler, L., & Klein, A. (2018). The effects of 2-hydroxyglutarate on the tumorigenesis of gliomas. *Contemporary oncology (Poznan, Poland),* 22(4), 215–222. https://doi.org/10.5114/wo.2018.82642

Ryan, D. G., Murphy, M. P., Frezza, C., Prag, H. A., Chouchani, E. T., O'Neill, L. A., & Mills, E. L. (2019). Coupling Krebs cycle metabolites to signalling in immunity and cancer. *Nature Metabolism*, 1, 16–33. https://doi.org/10.1038/s42255-018-0014-7

Ryan, D. G. & O'Neill, L. A. (2020). Krebs Cycle Reborn in Macrophage Immunometabolism. *Annual Review of Immunology*, 38, 289-313

Scacco, S., Petruzella, V., Budde, S., Vergari, R., Tamborra, R., Panelli, D., van den Heuvel, L. P., Smeitink, J. A., & Papa, S. (2003). Pathological Mutations of the Human NDUFS4 Gene of the 18-kDa (AQDQ) Subunit of Complex I

Affect the Expression of the Protein and the Assembly and Function of the Complex. *JBC,* 44161-44167.

Scheijen, J. L., Hanssen, N. M., van de Waarenburg, M. P., Jonkers, D. M., Stehouwer, C. D., & Schalkwijk, C. G. (2012). L(+) and D(-) lactate are increased in plasma and urine samples of type 2 diabetes as measured by a simultaneous quantification of L(+) and D(-) lactate by reversed-phase liquid chromatography tandem mass spectrometry. *Experimental Diabetes Research*, 234812. https://doi.org/10.1155/2012/234812

Scholte, H. R., Busch, H. F. M., Bakker, H. D., Bogaard, J. M., Luyt-Houwen, I. E. M., & Kuyt, L. P. (1995). Riboflavin-responsive complex I deficiency. *BBA – Molecular Basis of Disease,* 1271(1), 75-83. doi:10.1016/0925-4439(95)00013-T

Scialò, F., Fernández-Ayala, D. J., & Sanz, A. (2017). Role of Mitochondrial Reverse Electron Transport in ROS Signaling: Potential Roles in Health and Disease. *Frontiers in Physiology*, 8, 428. https://doi.org/10.3389/fphys.2017.00428

Seim, G. L., Britt, E. C., John, S. V., Yeo, F. J., Johnson, A. R., Eisenstein, R. S., Pagliarini, D. J., & Fan, J. (2019). Two-stage metabolic remodelling in macrophages in response to lipopolysaccharide and interferon-γ stimulation. *Nature Metabolism* 1(7), 731–742. https://doi.org/10.1038/s42255-019-0083-2

Sharma, R., Reinstadler, B., Engelstad, K., Skinner, O. S., Stackowitz, E., Haller, R. G., Clish, C. B., Pierce, K., Walker, M. A., Fryer, R., Oglesbee, D., Mao,

X., Shungu, D. C., Khatri, A., Hirano, M., De Vivo, D. C., & Mootha, V. K. (2021). Circulating markers of NADH-reductive stress correlate with mitochondrial disease severity. *The Journal of Clinical Investigation*, 131(2), e136055. https://doi.org/10.1172/JCI136055

Sheu, K. F. R. & Blass, J. P. (1999). The α-ketoglutarate dehydrogenase complex. Ann. *N Y Acad. Sci*, 893, 61-78.

Shtilbans, A., Shanske, S., Goodman, S., Sue, C. M., Bruno, C., Johnson, T. L., Lava, N. S., Waheed, N., & DiMauro, S. (2000). G8363A mutation in the mitochondrial DNA transfer ribonucleic acidLys gene: another cause of Leigh syndrome. *J Child Neurol*, 15(11), 759-61. doi: 10.1177/088307380001501109

Singh, S., Singh, P. K., Jha, A., Naik, P., Joseph, J., Giri, S., & Kumar, A. (2021). Integrative metabolomics and transcriptomics identifies itaconate as an adjunct therapy to treat ocular bacterial infection. *Cell Reports. Medicine*, 2(5), 100277. https://doi.org/10.1016/j.xcrm.2021.100277

Sofou, K., De Coo, I. F., Isohanni, P., Ostergaard, E., Naess, K., De Meirleir, L., Tzoulis, C., Uusimaa, J., De Angst, I. B., Lönnqvist, T., Pihko, H., Mankinen, K., Bindoff, L. A., Tulinius, M., & Darin, N. (2014). A multicenter study on Leigh syndrome: disease course and predictors of survival. *Orphanet Journal of Rare Diseases*, 9, 52. https://doi.org/10.1186/1750-1172-9-52

Struys, E. A., Salomons, G. S., Achouri, Y., Van Schaftingen, E., Grosso, S., Craigen, W. J., Verhoeven, N. M., & Jakobs, C. (2005). Mutations in the D-2-hydroxyglutarate dehydrogenase gene cause D-2-hydroxyglutaric

aciduria. *American Journal of Human Genetics*, 76(2), 358–360. https://doi.org/10.1086/427890

Struys, E., Jansen, E. E. W., Verhoeven, N. M., & Jakobs, C. (2004). Measurement of urinary D- and L-2-hydroxyglutarate enantiomers by stable-isotope-dilution liquid chromatography-tandem mass spectrometry after derivatization with diacetyl-L-tartaric anhydride. *Clin Chem*, 50(8), 1391-5

Sugden, M. C. & Holness, M. J. (2011). The pyruvate carboxylase-pyruvate dehydrogenase axis in islet pyruvate metabolism: Going round in circles?. *Islets*, 3(6), 302–319. https://doi.org/10.4161/isl.3.6.17806

Sun, K. A., Li, Y., Meliton, A. Y., Woods, P. S., Kimmig, L. M., Cetin-Atalay, R., Hamanaka, R. B., & Mutlu, G. M. (2020). Endogenous itaconate is not required for particulate matter-induced NRF2 expression or inflammatory response. *ELife*, 9, e54877. https://doi.org/10.7554/eLife.54877

Swain, A., Bambouskova, M., Kim, H., Andhey, P. S., Duncan, D., Auclair, K., Chubukov, V., Simons, D. M., Roddy, T. P., Stewart, K. M., & Artyomov, M. N. (2020). Comparative evaluation of itaconate and its derivatives reveals divergent inflammasome and type I interferon regulation in macrophages. *Nature Metabolism*, 2, 594-602

Takeda, H., Yamaguchi, T., Yano, H., & Tanaka, J. (2021). Microglial metabolic disturbances and neuroinflammation in cerebral infarction. *J. of Pharmacological Sciences,* 145(1), 130-139

Tanis, R. M., Piroli, G. G., Day, S. D., & Frizzell, N. (2015). The effect of glucose concentration and sodium phenylbutyrate treatment on mitochondrial

bioenergetics and ER stress in 3T3-L1 adipocytes. *Biochimica et Biophysica Acta*, 1853(1), 213–221. https://doi.org/10.1016/j.bbamcr.2014.10.012

Tannahill, G. M., Curtis, A. M., Adamik, J., Palsson-McDermott, E. M., McGettrick, A. F., Goel, G., Frezza, C., Bernard, N. J., Kelly, B., Foley, N. H., Zheng, L., Gardet, A., Tong, Z., Jany, S. S., Corr, S. C., Haneklaus, M., Caffrey, B. E., Pierce, K., Walmsley, S., Beasley, F. C., … O'Neill, L.A. (2013). Succinate is an inflammatory signal that induces IL-1β through HIF-1α. *Nature*, 496(7444), 238–242. https://doi.org/10.1038/nature11986

Tannahill, G. M., Iraci, N., Gaude, E., Frezza, C., & Pluchino, S. (2015). Metabolic reprograming of mononuclear phagocytes in progressive multiple sclerosis. *Frontiers in Immunology,* 6, 106. https://doi.org/10.3389/fimmu.2015.00106

Taylor, R., Jobling, M., Turnbull, D., & Chinnery, P. (2003). Frequency of rare mitochondrial DNA mutations in patients with suspected Leber's hereditary optic neuropathy. *Journal of Medical Genetics*, 40(7), e85. doi:10.1136/jmg.40.7.e85.

Taylor, R. W. & Turnbull, D. M. (2005). Mitochondrial DNA Mutations In Human Disease. *Nat Rev Genet,* 6(5), 389-402

Thompson Legault, J., Strittmatter, L., Tardif, J., Sharma, R., Tremblay-Vaillancourt, V., Aubut, C., Boucher, G., Clish, C. B., Cyr, D., Daneault, C., Waters, P. J., LSFC Consortium, Vachon, L., Morin, C., Laprise, C., Rioux, J. D., Mootha, V. K., & Des Rosiers, C. (2015). A Metabolic Signature of Mitochondrial Dysfunction Revealed through a Monogenic Form of Leigh

Syndrome. *Cell Reports*, 13(5), 981–989. https://doi.org/10.1016/j.celrep.2015.09.054

Trefely, S., Liu, J., Huber, K., Doan, M.T., Jiang, H., Singh, J., von Krusenstiern, E., Bostwick, A., Xu, P., Bogner-Strauss, J. G., Wellen, K. E., & Snyder, N. W. (2019). Subcellular metabolic pathway kinetics are revealed by correcting for artifactual post harvest metabolism. *Molecular Metabolism,* 30, 61-71

Turunen, M., Olsson, J., & Dallner, G. (2004). Metabolism and function of coenzyme Q. *BBA-Biomembranes,* 1660(1-2), 171-199

Tyrakis, P. A., Palazon, A., Macias, D., Lee, K. L., Phan, A. T., Veliça, P., You, J., Chia, G. S., Sim, J., Doedens, A., Abelanet, A., Evans, C. E., Griffiths, J. R., Poellinger, L., Goldrath, A. W., & Johnson, R. S. (2016). S-2-hydroxyglutarate regulates CD8+ T-lymphocyte fate. *Nature*, 540(7632), 236–241. https://doi.org/10.1038/nature20165

Ullah, M. I., Nasir, A., Ahmad, A., Harlalka, G. V., Ahmad, W., Hassan, M. J., Baple, E. L., Crosby, A. H., & Chioza, B. A. (2018). Identification of novel L2HGDH mutation in a large consanguineous Pakistani family- a case report. *BMC Med Genet*, 19(1), 25.

Uusimaa, J., Moilanen, J. S., Vainionpää, L., Tapanainen, P., Lindholm, P., Nuutinen, M., Löppönen, T., Mäki-Torkko, E., Rantala, H., & Majamaa, K. (2007). Prevalence, segregation, and phenotype of the mitochondrial DNA 3243A>G mutation in children. *Ann Neurol*< 62(3), 278-87. doi: 10.1002/ana.21196

Van Coster, R., Lombres, A., De Vivo, D. C., Chi, T. L., Dodson, W. E., Rothman, S., Orrechio, E. J., Grover, W., Berry, G. T., Schwartz, J. F., Habib, A., & DiMauro, S. (1991). Cytochrome c oxidase-associated Leigh syndrome: phenotypic features and pathogenetic speculations. *J Neurol Sci*, 104(1),97-111. doi: 10.1016/0022-510x(91)90222-s

Van den Bossche, J., O'Neill, L. A., & Menon, D. (2017). Macrophage Immunometabolism: Where Are We (Going)? *Trends Immunol*, 38(6), 395-406. doi: 10.1016/j.it.2017.03.001

Van Erven, P. M., Cillessen, J. P., Eekhoff, E. M., Gabreëls, F. J., Doesburg, W. H., Lemmens, W. A., Slooff, J. L., Renier, W. O., & Ruitenbeek, W. (1987). Leigh syndrome, a mitochondrial encephalo(myo)pathy. A review of the literature. *Clin Neurol Neurosurg*, 89(4), 217-30. doi: 10.1016/s0303-8467(87)80020-3

Villa, A., Gelosa, P., Castiglioni, L., Cimino, M., Rizzi, N., Pepe, G., Lolli, F., Marcello, E., Sironi, L., Vegeto, E., & Maggi, A. (2018). Sex-Specific Features of Microglia from Adult Mice. *Cell Reports*, 23(12), 3501–3511. https://doi.org/10.1016/j.celrep.2018.05.048

Vreeburg, R. A., Bastiaan-Net, S., & Mes, J. J. (2011). Normalization genes for quantitative RT-PCR in differentiated Caco-2 cells used for food exposure studies. *Food Funct,* 2(2), 124-9. doi: 10.1039/c0fo00068j

Wagner, G. R., Bhatt, D. P., O'Connell, T. M., Thompson, J. W., Dubois, L. G., Backos, D. S., Yang, H., Mitchell, G. A., Ilkayeva, O. R., Stevens, R. D., Grimsrud, P. A., & Hirschey, M. D. (2017). A Class of Reactive Acyl-CoA

Species Reveals the Non-enzymatic Origins of Protein Acylation. *Cell Metabolism*, 25(4), 823-837.e8,

Walker, D.G. & Lue, L.F. (2015). Immune phenotypes of microglia in human neurodegenerative disease: challenges to detecting microglial polarization in human brains. *Alzheimer's Research & Therapy*, 7(1), 56. https://doi.org/10.1186/s13195-015-0139-9

Watanabe, T., Nobusawa, S., Kleihues, P., & Ohgaki, H. (2009). IDH1 mutations are early events in the development of astrocytomas and oligodendrogliomas. *Am. J. Pathol*, 174, 1149–1153. doi: 10.2353/ajpath.2009.080958

Wedatilake, Y., Brown, R. M., McFarland, R., Yaplito-Lee, J., Morris, A. A., Champion, M., Jardine, P. E., Clarke, A., Thorburn, D. R., Taylor, R. W., Land, J. M., Forrest, K., Dobbie, A., Simmons, L., Aasheim, E. T., Ketteridge, D., Hanrahan, D., Chakrapani, A., Brown, G. K., & Rahman, S. (2013). SURF1 deficiency: a multi-centre natural history study. *Orphanet Journal of Rare Diseases,* 8, 96. https://doi.org/10.1186/1750-1172-8-96

Weerapana, E., Wang, C., Simon, G. M., Richter, F., Khare, S., Dillon, M. B., Bachovchin, D. A., Mowen, K., Baker, D., & Cravatt, B. F. (2010). Quantitative reactivity profiling predicts functional cysteines in proteomes. *Nature*, 468(7325), 790-5. doi: 10.1038/nature09472.

Wertman, V., Gromova, A., La Spada, A. R., & Cortes, C. J. (2019). Low-Cost Gait Analysis for Behavioral Phenotyping of Mouse Models of Neuromuscular

Disease. J*ournal of Visualized Experiments: JoVE*, (149), 10.3791/59878. https://doi.org/10.3791/59878

White, S. L., Collins, V. R., Wolfe, R., Cleary, M. A., Shanske, S., DiMauro, S., Dahl, H. H., & Thorburn, D. R. (1999). Genetic counseling and prenatal diagnosis for the mitochondrial DNA mutations at nucleotide 8993. *American Journal of Human Genetics*, 65(2), 474–482. https://doi.org/10.1086/302488

Wu, Q., Wang, Q., Mao, G., Dowling, C. A., Lundy, S. K., & Mao-Draayer, Y. (2017). Dimethyl Fumarate Selectively Reduces Memory T Cells and Shifts the Balance between Th1/Th17 and Th2 in Multiple Sclerosis Patients. *Journal of Immunology*, 198(8), 3069–3080. https://doi.org/10.4049/jimmunol.1601532

Yang, Y. & Gibson, G.E. (2019). Succinylation Links Metabolism to Protein Functions. *Neurochem Res*, 44(10), 2346-2359. doi: 10.1007/s11064-019-02780-x

Yates, B. J., Billig, I., Cotter, L. A., Mori, R. L., & Card, J. P. (2002). Role of the vestibular system in regulating respiratory muscle activity during movement. *Clin. Exp. Pharmacol. Physiol*, 29, 112–117

Ye, D., Guan, K. L., & Xiong, Y. (2018). Metabolism, Activity, and Targeting of D- and L-2-Hydroxyglutarates. *Trends in Cancer*, 4(2), 151–165. https://doi.org/10.1016/j.trecan.2017.12.005

Yun, J. H., Lee, D. H., Jeong, H. S., Kim, H. S., Ye, S. K., & Cho, C. H. (2021). STAT3 activation in microglia exacerbates for hippocampal neuronal

apoptosis in diabetic brains. *Journal of Cellular Physiology,* 1–13. https://doi.org/10.1002/jcp.30373

Zajd, C. M., Ziemba, A. M., Miralles, G. M., Nguyen, T., Feustel, P. J., Dunn, S. M., Gilbert, R. J., & Lennartz, M. R. (2020). Bone Marrow-Derived and Elicited Peritoneal Macrophages Are Not Created Equal: The Questions Asked Dictate the Cell Type Used. *Frontiers in immunology*, 11, 269. https://doi.org/10.3389/fimmu.2020.00269

Zhang, L., Sorensen, M. D., Kristensen, B. W., Reifenberger, G., McIntyre, T. M., & Lin, F. (2018A). D-2-hydroxyglutarate is an intercellular mediator in IDH-mutant gliomas inhibiting complement and T cells. *Clin. Cancer Res*, 24, 5381–5391. doi: 10.1158/1078-0432.CCR-17-3855

Zhang, Y., Wang, C., Yang, K., Wang, S., Tian, G., & Chen, Y. (2018B). A novel compound heterozygous mutation of the L2HGDH gene in a Chinese boy with L-2-hydroxyglutaric aciduria: case report and literature review. *Neurol Sci*, 39(10), 1697-1703.

Zhao, G. & Winkler, M. E. (1996). A novel alpha-ketoglutarate reductase activity of the serA-encoded 3-phosphoglycerate dehydrogenase of Escherichia coli K-12 and its possible implications for human 2-hydroxyglutaric aciduria. *Journal of Bacteriology*, 178(1), 232–239. https://doi.org/10.1128/jb.178.1.232-239.1996

Zheng, L., Cardaci, S., Jerby, L., MacKenzie, E. D., Sciacovelli, M., Johnson, T. I., Gaude, E., King, A., Leach, J. D., Edrada-Ebel, R., Hedley, A., Morrice, N. A., Kalna, G., Blyth, K., Ruppin, E., Frezza, C., & Gottlieb, E. (2015).

Fumarate induces redox-dependent senescence by modifying glutathione metabolism. *Nature Communications*, 6, 6001. https://doi.org/10.1038/ncomms7001

Zheng, X., Boyer, L., Jin, M., Kim, Y., Fan, W., Bardy, C., Berggren, T., Evans, R. M., Gage, F. H., & Hunter, T. (2016). Alleviation of neuronal energy deficiency by mTOR inhibition as a treatment for mitochondria-related neurodegeneration. *eLife*, 5, e13378. https://doi.org/10.7554/eLife.13378